AEDC-TR-71-90

cy 2

RADIATIVE HEAT TRANSFER OF COATINGS ON A CRYOGENIC SURFACE

Jeffrey A. Roux
University of Tennessee Space Institute

April 1971

Approved for public release; distribution unlimited.

VON KÁRMÁN GAS DYNAMICS FACILITY
ARNOLD ENGINEERING DEVELOPMENT CENTER
AIR FORCE SYSTEMS COMMAND
ARNOLD AIR FORCE STATION, TENNESSEE

NOTICES

AEDC-TR-71-90

RADIATIVE HEAT TRANSFER OF COATINGS ON A CRYOGENIC SURFACE

Jeffrey A. Roux
University of Tennessee Space Institute

FOREWORD

The research presented in this report was sponsored by the Arnold Engineering Development Center (AEDC), Air Force Systems Command (AFSC), Arnold Air Force Station, Tennessee, under Program Element 64719F.

The results of the research were obtained by ARO, Inc. (a subsidiary of Sverdrup & Parcel and Associates, Inc.), contract operator of AEDC, AFSC, under Contract F40600-71-C-0002. At the time this work was done, the author was a research assistant provided under ARO Subcontract 70-11-TS/OMD with the University of Tennessee Space Institute. The work was performed under ARO Project Nos. SW5906, SW5007, and VW5122 during the period from October 1968 to September 1970. The manuscript was submitted for publication on March 31, 1971.

The work described herein was used in partial fulfillment of Ph. D. dissertation requirements for the University of Tennessee Space Institute. The author would like to acknowledge many helpful suggestions, ideas, and comments, which contributed significantly to the progress of this work, from his colleagues. The assistance provided by Dr. A. M. Smith, Mr. B. E. Wood, and Mr. B. A. Seiber of ARO, Inc., deserves particular mention.

This technical report has been reviewed and is approved.

Michael G. Buja
First Lieutenant, USAF
Research and Development
Division
Directorate of Technology

Harry L. Maynard
Colonel, USAF
Director of Technology

ABSTRACT

An analytical model for the radiative characteristics of coatings formed on a cryogenic surface is presented. In creating a realistic mathematical model, six different sets of boundary conditions are employed in order to determine which most closely approximates the actual experimental results. The medium is considered to be absorbing and scattering; due to the cryogenic temperatures involved, emission is justifiably neglected. The scattering is considered as isotropic. To determine the best analytical model, the theoretical results are compared to experimental data in order to provide a test of the validity of the radiative transfer theory upon which the analytical predictions are based. Then using a combination of experimental results and the chosen analytical model, the monochromatic absorption and scattering coefficients for H_2O and CO_2 cryodeposits are simultaneously determined in the visible wavelength region. The results are demonstrated in the form of hemispherical-directional reflectance and intensity profiles within the medium. Also bidirectional reflectance distributions are presented and compared with experimental data.

TABLE OF CONTENTS

LIST OF FIGURES

FIGURE PAGE

FIGURE PAGE

FIGURE | PAGE

NOMENCLATURE

dA_i	Illuminated area
dA_j	Detector area
a_j	Weighing factor for Gaussian quadrature in Equation 23
C_k	Integration constants in Equation 92 to be determined through boundary conditions
E	Error term
e_b	Black body emission power
F_o	Incident normal colluminated flux
F_r	Reflected flux
h	Numerical integration step size
I	Intensity of radiation
I_o	Intensity of incident radiation
I_r	Intensity of reflected radiation
L	Physical thickness
n	Refractive index of a dielectric
$\bar{n}$	Complex refractive index
P_D	Detector power output
$p(\mu,\mu')$	Scattering function
p	Order of Gaussian quadrature
r	Distance between detector area and irradiated area
T	Temperature
v	Components of eigenvector in Equations 60 and 61
W	Albedo parameter, $\sigma/(\sigma + k)$

X	Eigenvector, Equation 92
x_j	Ordinate for Gaussian quadrature in Equation 23
y	Position coordinate

Greek Symbols

β	Radiation extinction coefficient, $\sigma + k$
γ	Eigenvalue
δ	Dirac delta function
δ_{ij}	Kronecker delta function
θ_1	Angle between outward normal and incident direction of pencil of radiation
θ	Angle between normal direction and direction of pencil of radiation (measured inside the deposit); θ is related to θ_1 by Snell's law Equation 35
θ_1^*	Angle of incidence of collimated radiation
i	Dimensionless intensity defined by Equations 6d and 127
k	Absorption coefficient
λ	Wavelength
μ	Cos θ
μ_1^*	Cos θ_1
$\rho_{ha}(\mu_1)$	Hemispherical-angular reflectance
$\rho_{ah}(\mu_1)$	Angular-hemispherical reflectance
$\rho_{ba}(\mu_1)$	Biangular reflectance
$\rho_{ba}^d(\mu_1)$	Diffuse component of biangular reflectance
σ	Scattering coefficient
τ	Optical depth defined by Equation 6b

τ_o	Optical thickness defined by Equation 6b where $y = L$
ω	Solid angle

Subscripts

1	Refers to vacuum
2	Refers to deposit
3	Refers to substrate

Superscripts

+	Refers to "forward" direction
-	Refers to "backward" direction

CHAPTER I

INTRODUCTION

With the dawning of the space-age many areas of science have been required to expand in breadth and depth. The demand for a high degree of sophistication in the field of radiation heat transfer has come about since radiation is the primary, if not the only, mode of heat transport in outer space. Also due to the high cost per pound of payload, small safety factors are required which in turn necessitate a high degree of accuracy in all fields of science.

The recent area of interest with respect to radiant exchange has been in the region of participating media, i.e. media which absorb, emit, and scatter radiant energy. The range of analysis has been from high temperature gas flows to low temperature cryodeposits.

Early interest in radiative transfer was directed toward high temperature applications where the absolute value of the temperature and hence emission were very important. More current areas of interest include thermal control of space vehicles and long-time storage of cryogenic fluids.

Problems associated with the presence of condensed gases on low temperature surfaces have recently begun to receive attention. The effect of cryogenic condensates (cryodeposits) on the operation of space simulation chambers has been of interest for some time. Since present-day space simulation chambers employ cryogenic pumping, the test vehicle is surrounded by LN_2(77 °K) cooled panels. In order to simulate the black sky of outer space and to "minimize" the reflection of radiation from the panels to the test model, the panels are painted black. During the period of testing, however, cryodeposits form on the cold panels. These deposits change the reflectance of the shroud, thus altering the thermal environment of the test model. In order to be able to correct the resulting thermal balance test data, it is necessary to have the capability of predicting the influence of film deposits on the reflection of radiation from the cold panels.

Figure 1, taken from Reference [1],[1] illustrates the change in steady-state temperature associated with the increased heat load due to the formation of cryodeposits on the floor and walls of a solar simulator.

Just as the formation of condensates in a simulation chamber may cause the almost zero wall reflectance to increase to significantly high values, film deposits may cause the reflectance of highly reflecting surfaces to decrease. Cryodeposits may form on the walls of cryogenic storage tanks designed for the long-time storage of cryogenic fluids in space. Therefore, the absorptance of radiation by the

---

[1]Numbers in brackets refer to similarly numbered references in the bibliography.

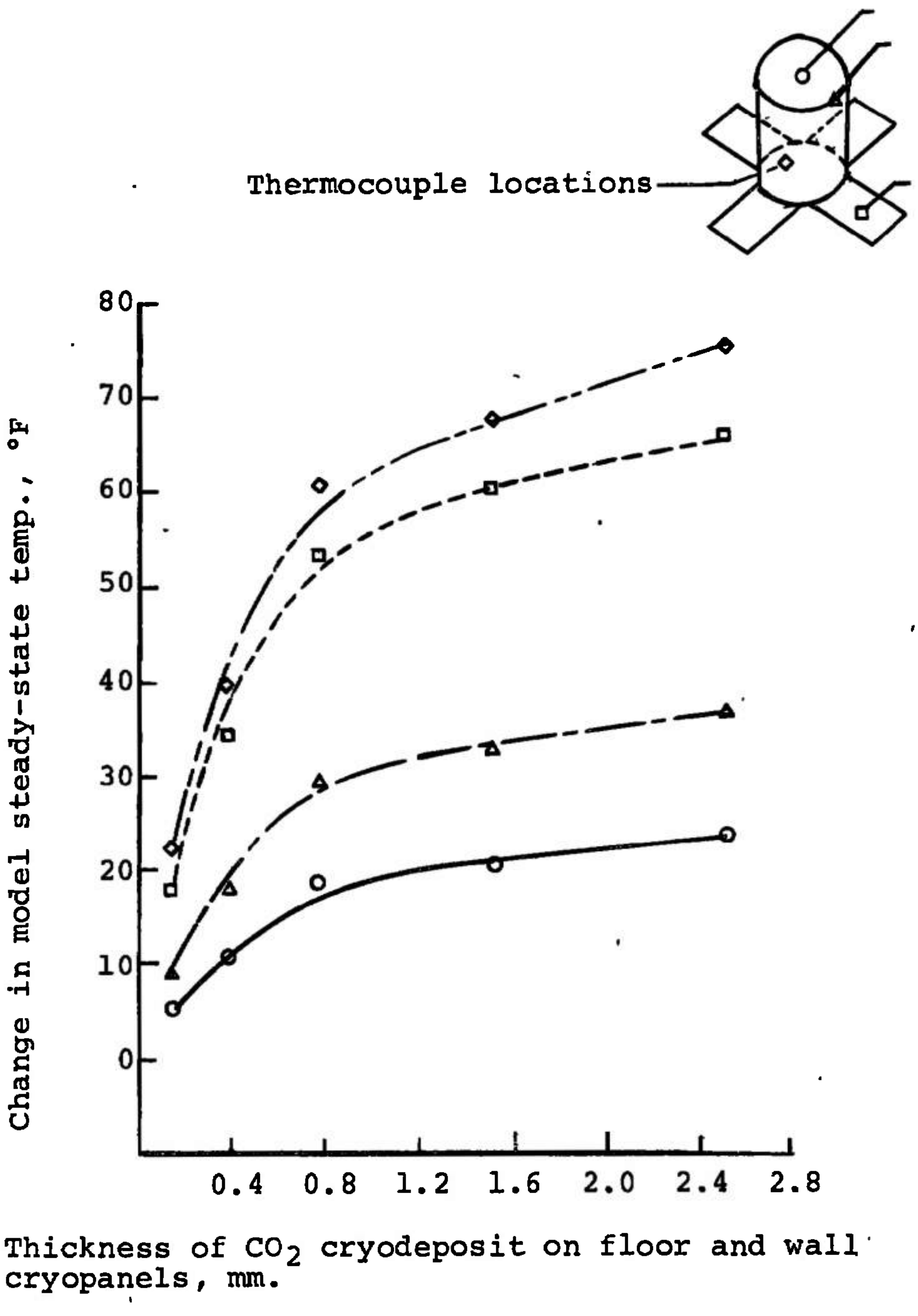

Figure 1. Changes in steady-state temperature of test model due to reflection of solar simulator flux from CO_2 cryodeposits.

Source: Mills, D. W., and A. M. Smith. "Effect of Reflections from CO_2 Cryopanel Deposits on the Thermal Balance of a Test Model in a Space Simulation Chamber," Journal of Spacecraft and Rockets, 7:374-376, March, 1970.

tank, and thus the boil-off rate of the cryogen, will depend on the radiative properties of the deposit. If the tank is shielded from various sources of radiation by shadow shields, the efficiency of shielding will depend on whether cryo-deposits are present and the nature of their radiative properties. Film deposits can also effect the thermal control of space vehicles or even increase the refrigeration load on a low temperature device.

An analysis will be presented for the radiative characteristics of solid films on various substrates and for various boundary conditions. A comparison will be made between the analytical model and current experimental data available from a wealth of publications in the recent literature.

In view of the vast progress that has been made in the field of radiant transport there is still a crucial need for radiant properties such as absorption and scattering coefficients. Most analyses are performed on a non-dimensional basis; this yields results which give important information with respect to general trends but does not reveal much information for numerical design values.

In this investigation an attempt will be made to obtain monochromatic absorption and scattering coefficients based on a combination of experimental data and analytical results.

A review of the pertinent experimental and analytical literature is given in Chapter II. In Chapter III the physical and geometrical problem is defined, and in Chapter IV the numerical solution to the transport equation is described. The theoretical results of various analytical models are presented in Chapter V from which the one conforming most to the data is selected in Chapter VI. In Chapter VII an initial guess criteria is presented for the numerical solution. A discussion of the numerical error is given in Chapter VIII, and the analysis for determination of property coefficients is presented in Chapter IX. Finally, in Chapter X biangular results are shown.

CHAPTER II

SURVEY OF LITERATURE

Most of the reflectance characteristics of cryodeposits have been primarily of an experimental nature such as in References [2], [3], [4], and [5]. These experimental results are important because any analytical model should be validated at least through quantitative agreement with the experimental data.

Several analytical investigations have been conducted concerning the radiant heat transfer in an absorbing, emitting, and scattering medium, but most of the results were for high temperature applications and for low values of the albedo parameter, W.

The definitions of hemispherical-angular reflectance, angular-hemispherical reflectance, and biangular reflectance are of fundamental importance for thorough understanding of the material presented hereafter.

The hemispherical-angular reflectance, ρ_{ha} is defined as the ratio of the intensity reflected from an infinitesimal area dA, collected in a specific angular direction to the incident intensity which is hemispherically distributed.

The angular-hemispherical reflectance, ρ_{ah}, is defined as the ratio of the flux reflected from an infinitesimal element of area dA, collected over the entire hemispherical space to the flux reflected from a white perfectly diffuse-reflecting surface which is a beam orientated at a specific angle relative to the surface normal.

The biangular reflectance, ρ_{ha}, is defined as the ratio of the intensity reflected from an infinitesimal area dA, collected in a specific angular direction to the intensity reflected from a white perfectly diffuse-reflecting surface. The incident radiation is a beam orientated at a specific angle relative to the surface normal. The angular-hemispherical reflectance can be obtained by integration of the biangular reflectance. For a rough or smooth surface it can be shown that the angular-hemispherical and hemispherical-angular reflectances are equal. One of the purposes of this research will be to determine whether or not it is reasonable that the angular-hemispherical and hemispherical-angular reflectances are equal for a cryodeposit and substrate complex.

I. ANALYTICAL STUDIES

Several authors have found solutions to the radiative transport equation for various limiting cases and for various values of the governing dimensionless parameters. Francis and Love [6] considered isothermal dielectrics on a conductor substrate; dielectrics have only a real refractive index, whereas conductors have a complex refractive index. The dielectric coating was assumed to be a homogeneous, absorbing and emitting medium, but scattering was neglected. The geometry was regarded to be infinite in extent but with finite thickness. The dielectric-air and dielectric-conductor interfaces were taken parallel and were assumed to be perfectly smooth with specular reflectances given by Fresnel's law.

When scattering is neglected closed form analytical solutions are often possible as in [6] and Love [7]. Pepper [8] has also performed a non-scattering analysis for ice cryodeposits. The correspondence between experimental and analytical results was reasonable, but this was only because scattering is not prominent for H_2O deposits in the infrared region which was considered.

Analyses which have accounted for scattering have been primarily of a high temperature nature. Hsia and Love [9] published a computational method for monochromatic heat transfer in the plane, one-dimensional case of a medium with a given temperature profile, and anisotropically scattering particles suspended. They approximated the equation of transfer by a system of ordinary differential equations, applying the classical method of discrete coordinates. This technique is a cornerstone because it permits the application of quadrature approximations to the integral term in the radiative transport equation--an integrodifferential equation describing the radiation intensity field--and so to reduce the transport equation to a system of simultaneous ordinary linear differential equations. The system of differential equations was solved by finding the eigenvalues and eigenvectors through the method of idempotents. However, as indicated by Love convergence of the resulting computer program could not be obtained for values of the albedo parameter, W, greater than 0.7. It should be noted that the double Gaussian quadrature was used in [9].

Hottel et al. [10] employed the method of discrete coordinates to calculate the biangular reflectance from an absorbing, emitting, and anisotropically scattering medium with allowance of Fresnel reflection at the boundaries. Hottel also solved the system of simultaneous differential equations by calculating the eigenvalues and eigenvectors. But as indicated by Love, Hottel encountered difficulties in obtaining convergence of his eigenvalue program for values of the albedo parameter greater than 0.9.

The most pertinent research recently published with regard to cryodeposits was done by Merriam [11]. Merriam [11] analytically and experimentally investigated the radiative characteristics of condensed gas deposits on cold surfaces. Absorbing, emitting, and scattering media bounded by diffuse and specular surfaces were considered. The substrate, however, was taken as a constant reflecting surface regardless of whether or not a deposit was present. This assumption neglects the reflectance change that results due to the relative refractive index change occurring after the deposit forms on the initially bare substrate. Both gray and non-gray models were treated, and the effects of different scattering functions were discussed. Results were presented for the reflectance and absorptance of deposits with diffuse or collimated incident radiation. Good agreement was shown between the data and theory for a deposit which was essentially non-scattering. However, a comparison of theory and experimental data was not shown for a highly scattering deposit.

Merriam [11] employed two different methods of solution. First the integro-differential transport equation was integrated to yield an integral equation. The integral equation was solved by successive approximations. However, the successive-approximations solution of the integral equation would only converge for very low values of the albedo parameter; for albedo values at which convergence was attained, the convergence was extremely slow (10 to 100 times slower than the method of discrete coordinates [11]).

The second approach of Merriam [11] was to use the method of discrete coordinates (24 point single Gaussian quadrature). The eigenvalues and eigenvectors were computed by a numerical procedure based on the "method of Danilevsky" discussed by Faddeeva [12]. Solutions to the system of differential equations were obtained for W = 1.0, but not all of the eigenvalues were real for the albedo value of unity. All but two of the roots were real and distinct. Hsia stated that based on his experience all the eigenvalues were real and the roots appeared in positive and negative pairs.

It appears that for various values of W and for different orders of quadrature many problems may be encountered, such as when the eigenvalues are complex or when the eigenvalues are of multiplicity greater than one. Additional problems are created in finding the eigenvectors which correspond to these eigenvalues, and difficulties occur in determining the integration constants through the boundary conditions.

Since the coefficient matrix in general is rather arbitrary there appears to be many problems associated in calculating the eigenvalues and eigenvectors (especially for W near unity). Thus, it seems wise to try a different approach, such as a numerical solution to the system of differential equations.

Wolf [13] considered radiation heat transfer in absorbing, emitting, and scattering media with arbitrary temperature profiles in plane, spherical, and cylindrical geometries; the bounding surfaces were taken to be diffuse. After reducing the transport equation to a system of ordinary differential equations, Wolf [13] solved the system of equations numerically. The two methods used were the modified Euler method and Simpson's rule. As was done by Hottel [10] and Merriam [11], Wolf [13] also used the single Gaussian quadrature for the method of discrete coordinates.

Wolf [13] first analytically solved the system for $W = 0.0$ and then used this solution as an initial guess for the solution at $W = 0.1$. This procedure was continued until $W \simeq 0.6$. Convergence was not obtained for higher values of the albedo parameter according to Wolf. Unfortunately, in the visible wavelength region, H_2O and CO_2 cryodeposits are very highly scattering which corresponds to a near unity value for W.

Thus, it appears that a major disadvantage of using the numerical approach would be that convergence is either very slow or that it is difficult to make a wise initial guess for high W values. It is desirable to have a numerical solution in order to avoid the complications of the eigen-value computation. But it is also desirable to have a numerical solution for W = 1.0, which can converge in a reasonable amount of time by building up the solution from W = 0.0 and making successive initial guesses as done by Wolf [13].

Hopefully, one could make an intelligent enough initial guess for W = 1.0 so that convergence is obtainable without having to waste time solving the case of W = 0.0, W = 0.1, and so forth, in order to build up a solution. It is a purpose of this work to develop a means of making an initial guess at the solution for W = 1.0 directly such that convergence is possible and rapid.

II. EXPERIMENTAL RESULTS

Experimental results are very important since they are the physical basis for confirming or disqualifying any attempt at an analytical model. From observation of experi-mental data one can use the available mathematical tools and laws of physics to try to formulate a realistic model of the observed phenomena.

It was not the purpose of this investigation to concentrate on experimental technique but rather to use the supply of published results as a guide in establishing a realistic theoretical model.

Many of the results are given in the forms of hemispherical-angular reflectance, ρ_{ha}, angular-hemispherical reflectance, ρ_{ah}, and biangular reflectance, ρ_{ha}. Wood et al. [3] measured the angular-hemispherical reflectance of CO_2 cryodeposits on 77 °K black and stainless steel substrates. It was found that in all the measurements on cryodeposits, the reflectance decreased as the wavelength increased. The measurements taken in [3] were in the 0.37 to 0.81 micron range. Also the spectral reflectance data of CO_2 cryodeposits show the same general trends as the total reflectance data. The reflectance increases with an increase in the viewing angle of the irradiated surface and an increase in cryodeposit thickness. Neglecting the effects of the above parameters on the reflectance would introduce serious errors in the heat balance calculations. Why does the reflectance decrease as wavelength increases? Is it because the scattering coefficient decreases, or because the absorption coefficient increases, or a combination of both?

McCullough et al. [2] measured the hemispherical-angular and biangular reflectances of CO_2 cryodeposits in the 0.01 to 1.1 micron range. The surfaces investigated were polished copper and rough copper, black paint, and a front surface aluminized mirror, all maintained at 77 °K. The total reflectance measurements have indicated the following conclusions:

1. The reflectance of the substrate has a strong influence on the total reflectance of a surface for thin layers of CO_2 cryodeposits.
2. A reflectance plateau will occur for thick deposits which is essentially independent of the substrate.
3. The reflectance of a surface is a strong function of the viewing angle of the light reflected. The larger viewing angles (from the normal) yield higher total reflectances.

Figure 2 illustrates the trend of the angular dependence for a black substrate.

In [4] the hemispherical-angular reflectance was measured in the 0.5 to 10 micron wavelength range. Reflectance data for CO_2 cryodeposits on stainless steel and black paint substrates were presented as a function of wavelength and cryodeposit thickness. In Figure 3 the reflectances of CO_2-black paint, and CO_2-stainless steel complexes are shown as a function of thickness at 0.75 micron wavelength. There is a sharp reduction (almost in the form of a discontinuity) in reflectance for a near zero thickness of CO_2 cryodeposits. As the thickness is increased further, the reflectance attains a minimum and then increases slowly. McCullough <u>et al</u>. [4] attributes this to scattering and absorption

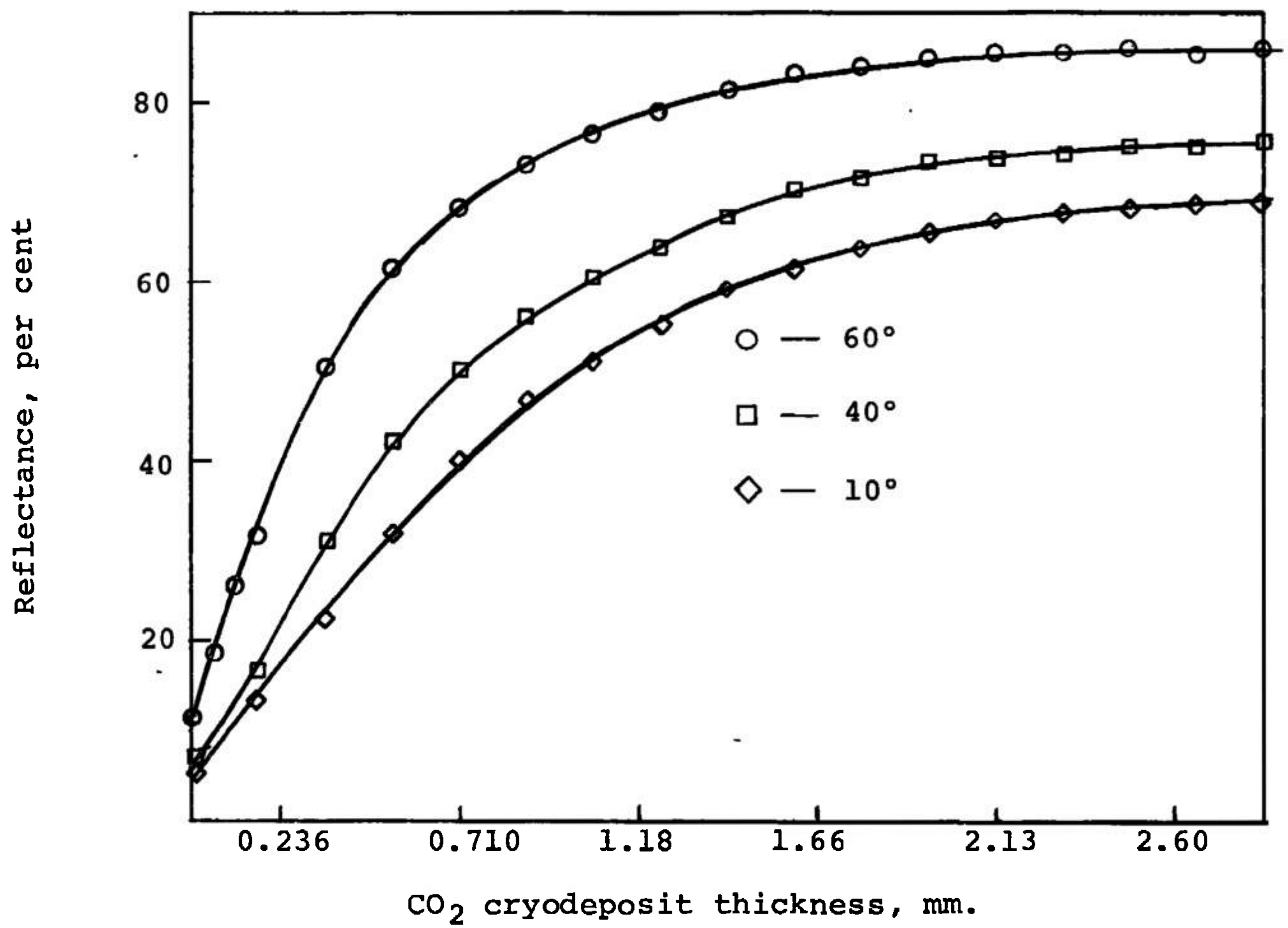

Figure 2. Total angular-hemispherical reflectance of CO_2 cryodeposit on a black paint substrate.

Source: McCullough, B. A., B. E. Wood, and J. P. Dawson. "Thermal Radiative Properties of Carbon Dioxide Cryodeposits from 0.5 to 1.1 Microns," Arnold Engineering Development Center TR-65-94, Arnold Air Force Station, Tennessee, August, 1965.

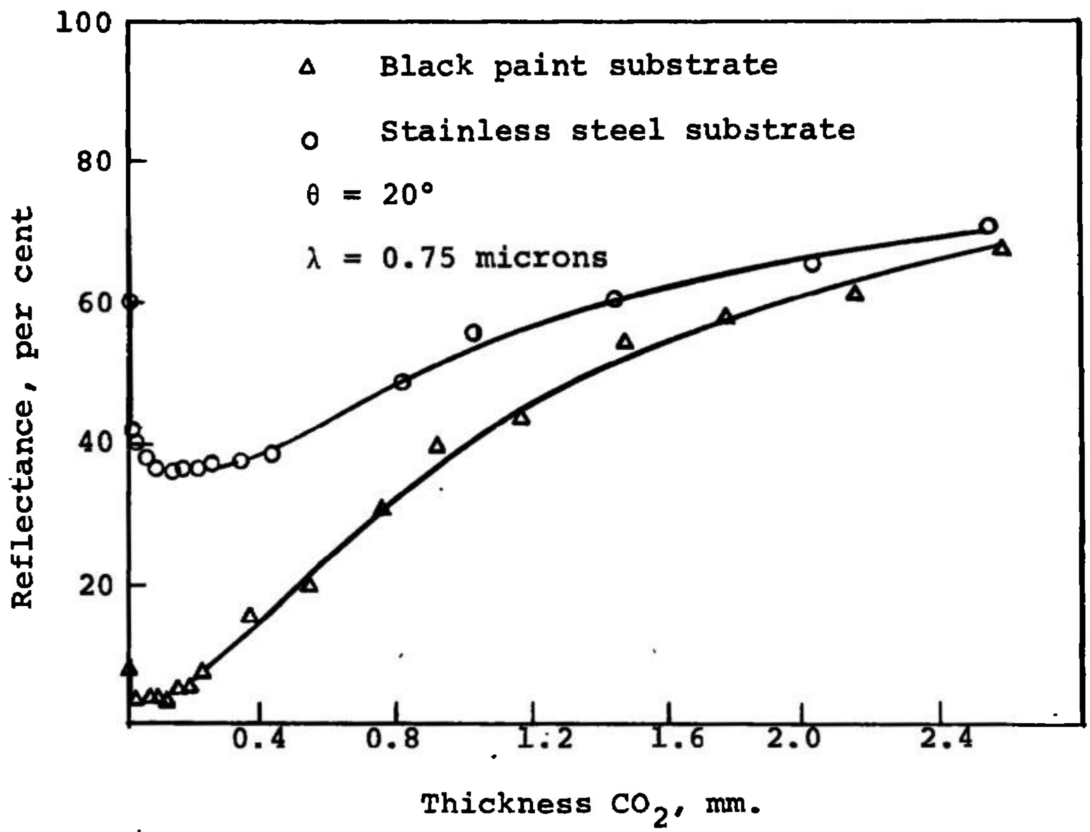

Figure 3. Effect of CO_2 cryodeposit thickness on the cryodeposit-substrate (hemispherical-angular) reflectance.

Source: McCullough, B. A., B. E. Wood, and A. M. Smith. "A Vacuum Integrating Sphere for In Situ Reflectance Measurements at 77 °K from 0.5 to 10 Microns," Arnold Engineering Development Center TR-67-10, Arnold Air Force Station, Tennessee, April, 1967.

phenomena which occur within the cryodeposit. This decrease and subsequent increase are of current interest since it shows that depending on the cryodeposit thickness, the cryodeposit-substrate complex may possibly either increase or decrease the reflectance relative to the bare substrate. One purpose of this analytical investigation is to present a sound physical explanation for this phenomena. McCullough et al. [4] also concluded that the hemispherical-angular reflectance of CO_2 frost is essentially independent of the substrate material in the visible wavelength range for large deposit thicknesses.

Wood et al. [14] investigated the variation of H_2O and CO_2 reflectances with angle of viewing and deposit thickness on a black paint substrate. It was concluded that H_2O and CO_2 cryodeposit reflectances are strongly dependent on thickness up to approximately 1 mm. A further increase in thickness resulted in a relatively small reflectance change. Also thin film interference effects were observed for thin films of both H_2O and CO_2 formed on polished copper and black paint surfaces. In general the presence of the thin film caused a decrease in the reflectance. This decrease corresponds to the sharp initial drop in Figure 3.

Müller [5] measured biangular reflectances of CO_2 and H_2O cryodeposits on copper and black paint substrates. In general, it was found that as the deposit thickness increased, the reflectance in the specular direction decreased and that the reflectance in the non-specular directions increased.

Based on the light distributions for roughened glass surfaces from [5], it was concluded that an approximate mathematical model for a rough surface would be to assume the rough interface to transmit radiation specularly, yet reflect radiation diffusely. One of the analytical vacuum-interface models for the cryodeposit is due to the experimental results of [5].

In performing any engineering calculations certain physical properties are needed. For the determination of the monochromatic absorption and scattering coefficients, it is necessary to have the refractive index as a function of wavelength. Figures 4 and 5 show the refractive index of H_2O and CO_2 cryodeposits in the visible region. Müller also measured the refractive index of the black paint which was used in his work; its value was given as 1.48 ± 0.03.

Brown [15] experimentally measured cryopumping speed, thickness, density, optical, and thermal radiation properties of physically absorbed gaseous cryodeposits. One of his results was that the extinction coefficient for H_2O cryodeposits of thicknesses greater than 4.0×10^{-4} cm was approximately 1.55×10^{3} cm^{-1} at 0.6328 microns.

A realistic theoretical model should show at least some of the same general trends as the experimental data shown and discussed in this section.

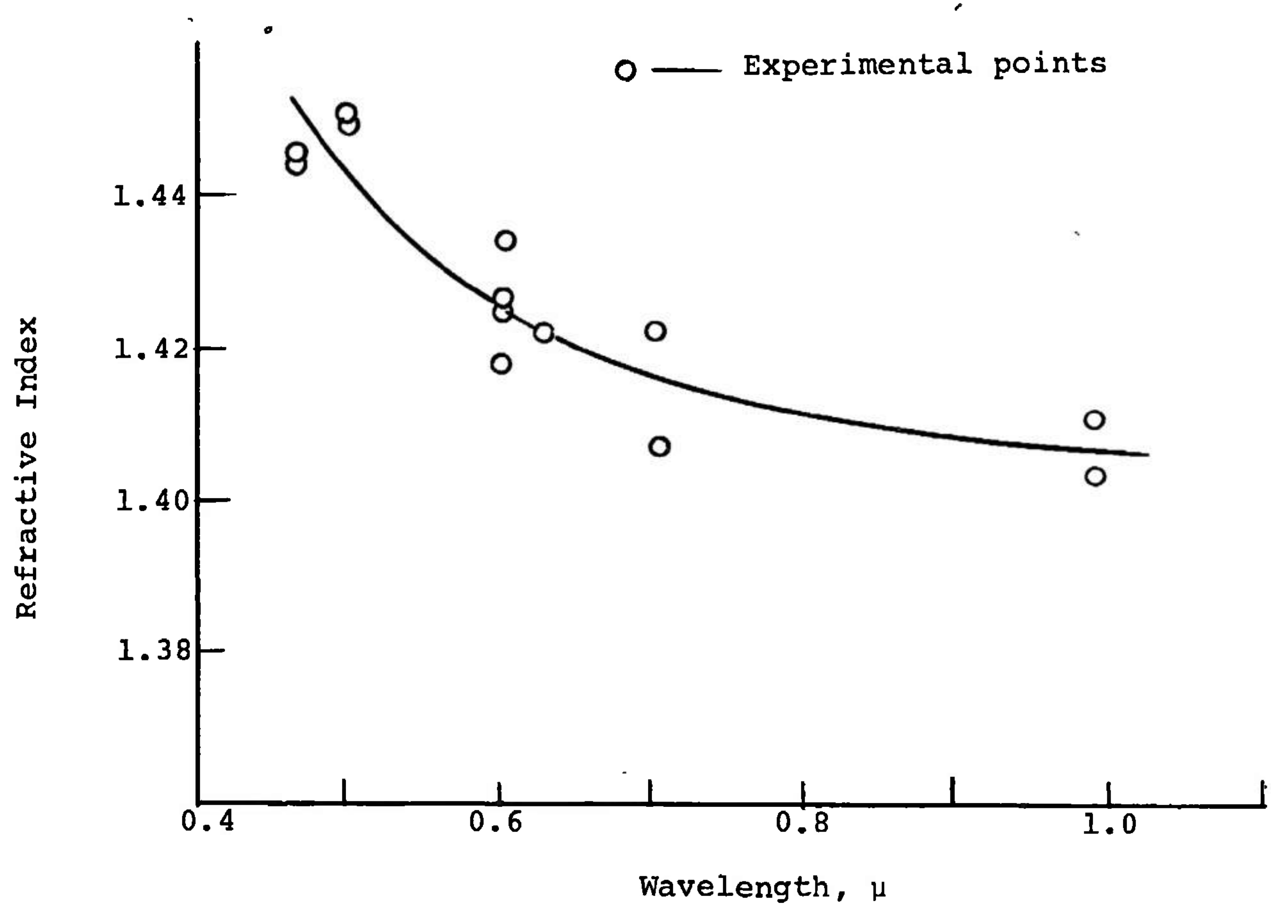

Figure 4. Refractive index of CO_2 cryodeposits.

Source: Müller, P. R. "Measurements of Refractive Index, Density, and Reflected Light Distributions for Carbon Dioxide and Water Cryodeposits and Also Roughened Glass Surfaces." Ph.D. dissertation, The University of Tennessee, Knoxville, June, 1969.

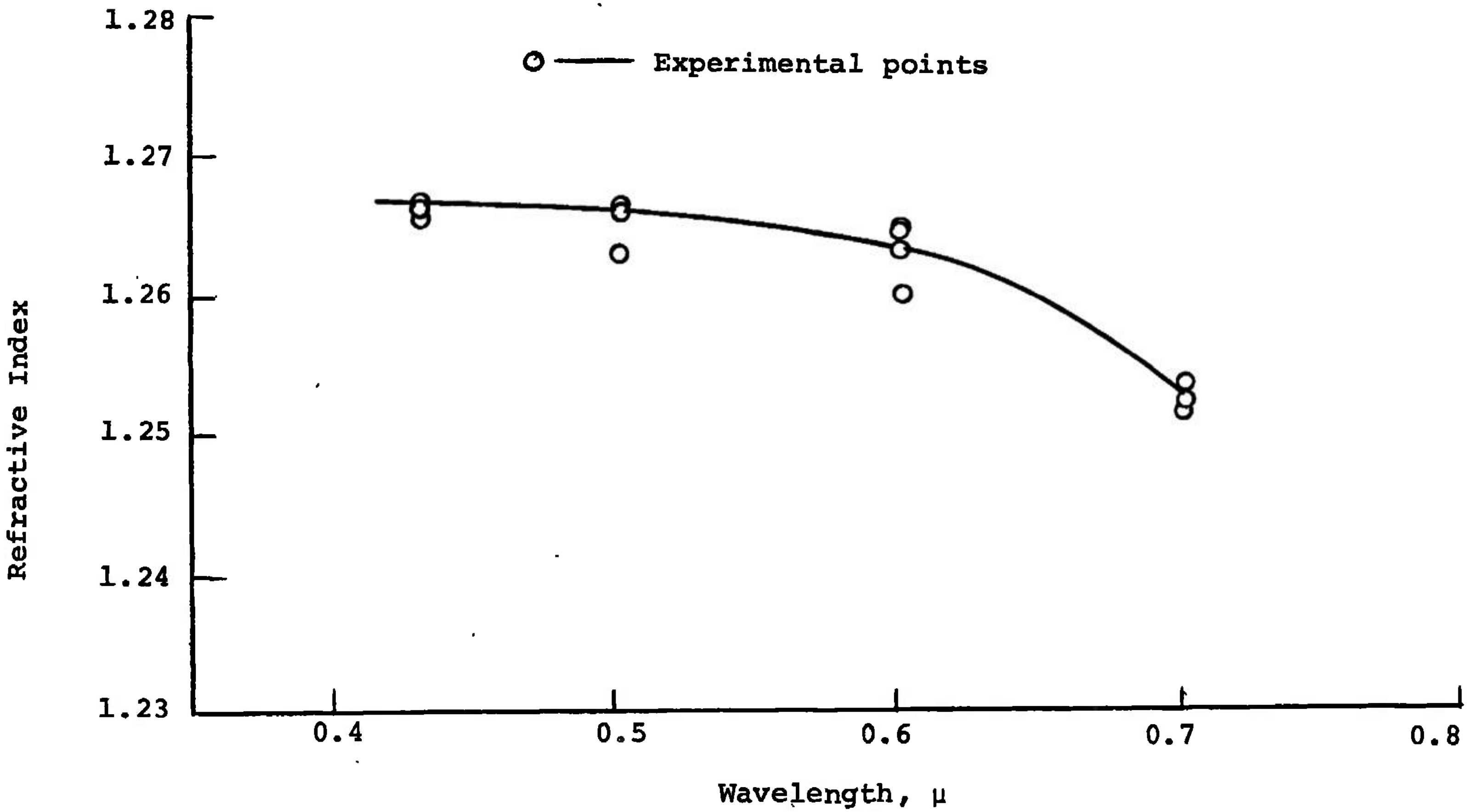

Figure 5. Refractive index of H_2O cryodeposits.

Source: Müller, P. R. "Measurements of Refractive Index; Density, and Reflected Light Distributions for Carbon Dioxide and Water Cryodeposits and Also Roughened Glass Surfaces." Ph.D. dissertation, The University of Tennessee, Knoxville, June, 1969.

CHAPTER III

ANALYSIS

I. STATEMENT OF PROBLEM

The physical problem is illustrated schematically in Figure 6. Since initially theory and data for the hemispherical-angular reflectance will be considered, the radiant energy is taken to be diffusely incident upon a differential area of a two-layered medium consisting of a semi-transparent layer, the deposit, and an opaque (non-transparent) substrate. The surrounding medium is considered to be a vacuum with refractive index equal to unity. The cryodeposit is assumed to be a dielectric; a dielectric is a substance which has a real number as its refractive index. The substrate is taken to be either a dielectric or a non-dielectric; a non-dielectric is a material which has a complex number for its refractive index. Since the index of refraction of the cryodeposit is different from unity, some of the energy incident will be reflected at the vacuum-deposit interface. Also since the substrate and cryodeposit will generally have different refractive indices, part of the energy incident on the substrate will be reflected back into the deposit. The other portion will be absorbed by the substrate.

The physical coordinate system is also described in Figure 6. Regions 1, 2, and 3 represent the vacuum, deposit,

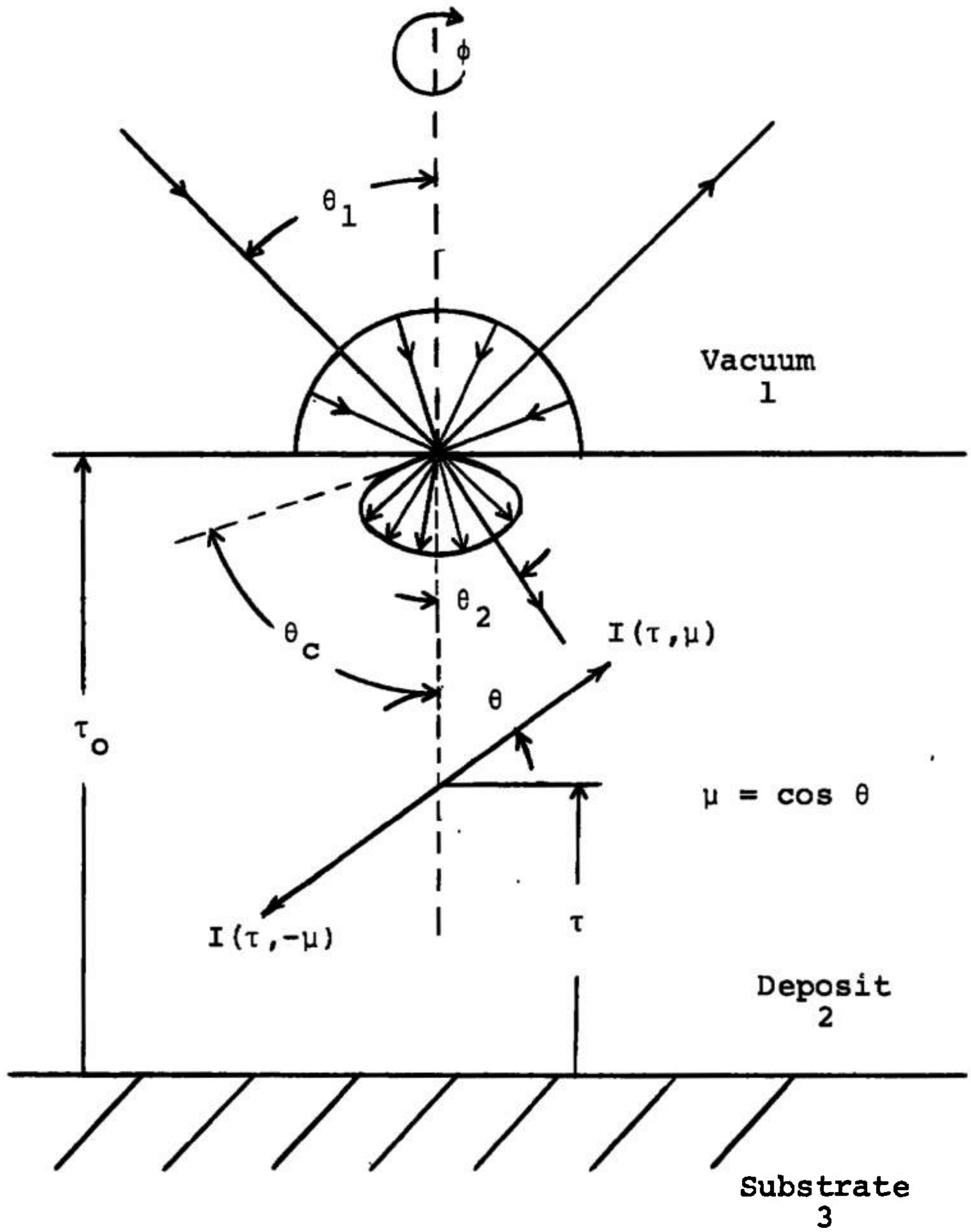

Figure 6. Geometrical arrangement.

and substrate respectively. Since in general the reflectance in going from medium 1 to medium 2 and the reflectance in transversing from medium 2 to medium 1 is not equal for a specified angle $\theta_1 = \theta_2$, the two reflectances will be designated ρ_{12} and ρ_{21} respectively. The foregoing also applies for the deposit-substrate interface.

Basic Assumptions

The two interfaces when assumed as smooth, are taken to reflect specularly so that the interface reflectances can be calculated according to the Fresnel reflection law.

The interior of the cryodeposit is taken to be an absorbing and scattering medium. Due to the very low temperatures involved (approximately 77 °K), emission is justifiably neglected. The scattering is assumed to be coherent (no frequency change). The directional distribution of the scattered energy is characterized by the scattering function $p(\theta', \phi'; \theta, \phi)$ such that $p(\theta', \phi'; \theta, \phi)d\omega/4\pi$ represents the probability that radiation incident in the direction (θ', ϕ') will be scattered in the direction (θ, ϕ). In this work the scattering is assumed to be isotropic; thus, radiation is scattered uniformly in all directions. The intensity field is also assumed to be axisymmetric; hence, the intensity field is independent of the azimuthal angle ϕ. The intensity field is also assumed to be one-dimensional, therefore, dependent only on one spacial coordinate, namely the y or τ coordinate.

The assumption of single scattering is also imposed. Because the radiative transport equation is based on conservation or balance about a differential element, dy, single scattering implies that a beam of intensity incident on an infinitesimal element can undergo at most one scatter. This does not mean that a beam of intensity can not be scattered many times as it travels through the deposit; it only means that scatter can occur only once in each differential element. In passing through many dy elements the beam may be scattered many times. Also, as usual in most continuum formulations, local thermodynamic equilibrium is assumed.

The incident radiation is taken to be unpolarized and assumed to obey Snell's refraction law.

Associated with Snell's law is the critical angle phenomena; Snell's law states

$$n_2 \sin \theta_2 = n_1 \sin \theta_1 \tag{1}$$

or

$$\sin \theta_2 = \left(\frac{n_1}{n_2}\right) \sin \theta_1 \tag{2}$$

where $n_1 = 1$ and $n_2 > 1$.

For diffusely incident radiation the maximum angle of incidence, θ_1, is 90 degrees. This shows that since $(n_1/n_2) < 1$, the radiation refracted into the deposit is contained in the angular region $0 < \theta_2 < \sin^{-1} (n_1/n_2) < 90$ degrees.

In conjunction with Snell's law is Fresnel's reflection law. Considering the assumptions made, Appendix A shows that the interface reflectances ρ_{12}, ρ_{21}, and ρ_{23} are functions only of the angle of incidence and the refractive indices of the two media about the interface.

A reflectance decrease is associated with the relative refractive index change at the substrate-deposit interface. Initially the bare substrate reflectance is given by

$$\rho_{ha}(\mu_1) = \rho_{13}(\mu_1) \tag{3}$$

(in accordance with Appendix A) since the intensity transverses directly from vacuum to substrate. As the deposit begins to form on the substrate, several monolayers of molecules accumulate. The thickness of the layer is so small that absorption and scattering do not effectively occur; however, the radiation must now transverse from vacuum indirectly to the substrate by transmitting across the extremely thin deposit. The hemispherical-angular reflectance of the thin layer and substrate is now given, as indicated in Appendix B, by

$$\rho_{ha}(\mu_1) = \rho_{12}(\mu_1) + \frac{\rho_{23}(\mu)[1 - \rho_{21}(\mu)][1 - \rho_{12}(\mu_1)]}{[1 - \rho_{21}(\mu)\rho_{23}(\mu)]} \tag{4}$$

This abrupt reflectance change from Equation 3 to Equation 4 occurs over a thickness of a monolayer. Plotted on a centimeter scale it appears to be a discontinuity as shown by the experimental data in Figure 3, page 16.

The radiative transport equation has been derived in detail by [16] and [17] and will not be repeated here. The transport equation describing the intensity field for the monochromatic, axisymmetric case is

$$\cos\,\theta\frac{dI(y,\theta)}{dy} = -\beta I(y,\theta) + \frac{\sigma}{2}\int_0^{\pi} I(y,\theta')\sin\,\theta' p(\theta,\theta')d\theta'$$

$$+ \frac{n^2}{\pi}\,k\;e_b(y) \tag{5}$$

The transport equation describes the change of the intensity in the direction θ at a thickness y due to transversing a differential thickness dy. The first term on the right represents the attenuation of the intensity as it passes through the slab dy due to both absorption and scattering. The second term represents the augmentation of the intensity by energy scattered within the slab due to all incident beams of energy. The last term represents the augmentation of the intensity as the result of emission from the elemental volume corresponding to dy.

Isotropic scattering corresponds to the condition that $p(\theta', \theta) = 1$; negligible emission implies that $e_b(y) = 0$. After introducing $\mu = \cos\,\theta$ the transport equation becomes

$$\frac{dI(y,\mu)}{dy} = -\,\frac{\beta}{\mu}\,I(y,\mu) + \frac{\sigma}{2\mu}\int_{-1}^{1} I(y,\mu')d\mu' \tag{6a}$$

It has been found convenient by other authors, Love [7] and Merriam [11], to non-dimensionalize Equation 6a in terms of optical thickness, τ, and the albedo parameter, W.

Defining

$$\tau = \int_{0}^{y} \beta dy \tag{6b}$$

$$W = \frac{\sigma}{\sigma + k} \tag{6c}$$

and

$$i(\tau,\mu) = \frac{I(\tau,\mu)}{I_o} \tag{6d}$$

where I_o is the incident diffuse intensity and introduction into Equation 6a yields

$$\frac{di(\tau,\mu)}{d\tau} = \frac{-i(\tau,\mu)}{\mu} + \frac{W}{2\mu} \int_{-1}^{1} i(\tau,\mu')d\mu' \tag{7}$$

Equation 7 together with boundary conditions constitutes the basic mathematical problem to be solved for the description of the intensity field under the assumptions that have been hithertofore stated.

II. BOUNDARY CONDITIONS

In the search for a realistic deposit model several combinations of boundary conditions were considered for the substrate- and vacuum-deposit interfaces. The six sets of boundary conditions employed were:

1. Specular reflector and transmitter on a specular substrate
2. Specular reflector and transmitter on a diffuse substrate
3. Diffuse reflector and transmitter on a specular substrate
4. Diffuse reflector and transmitter on a diffuse substrate
5. Diffuse reflector and specular transmitter on a specular substrate
6. Diffuse reflector and specular transmitter on a diffuse substrate

Specular Reflector and Transmitter on a Specular Substrate

As stated previously the incident intensity is diffusely distributed, that is, the incident intensity is the same from every direction. A specular reflector means that the angle of incidence is equal to the angle of reflection, but the magnitude of the reflection is dependent on the angle of incidence as given in Appendix A. In mathematical form the boundary conditions for this model are:

$$I(\tau_o, -\mu) = \rho_{21}(\mu) I(\tau_o, \mu) + [1 - \rho_{12}(\mu_1)] n^2 I_o \tag{8}$$

at the vacuum-deposit interface and

$$I(o, \mu) = \rho_{23}(\mu) I(o, -\mu) \tag{9}$$

at the deposit-substrate interface, or on a non-dimensional basis

$$i(\tau_o, -\mu) = \rho_{21}(\mu)i(\tau_o,\mu) + [1 - \rho_{12}(\mu_1)]n^2 \tag{10}$$

$$i(o,\mu) = \rho_{23}(\mu)i(o, -\mu) \tag{11}$$

Specular Reflector and Transmitter on a Diffuse Substrate

Case 2 differs from case 1 in that the substrate is diffuse. One usually associates diffuseness with a rough surface. Strictly speaking, diffuse only means that the intensity incident at any given angle is uniformly reflected in all directions. This, however, implies nothing about the magnitude of the diffuse reflectance. Most analyses use the diffuse reflectances as a parameter. In this work the diffusely reflected intensity will be taken as the specularly reflected Fresnel flux divided by π. Mathematically and in terms of the boundary conditions this means that at the substrate

$$i(o,\mu) = i(o) = \frac{1}{\pi}\int_o^{2\pi}\int_o^1 \rho_{23}(\mu)i(o, -\mu)\mu d\mu d\phi \tag{12}$$

$$i(o) = 2\int_o^1 \rho_{23}(\mu)i(o, -\mu)\mu d\mu \tag{13}$$

given the vacuum-deposit boundary condition is

$$i(\tau_o, -\mu) = \rho_{21}(\mu)i(\tau_o,\mu) + [1 - \rho_{12}(\mu_1)]n^2 \tag{14}$$

The definition of diffuse hemispherical-angular reflectance presented in Equation 13 means that the intensity incident for every direction is uniformly reflected into every other direction, but the magnitude of the radiation uniformly reflected into all directions is dependent on the angle of incidence.

Diffuse Reflector and Transmitter on a Specular Substrate

In case 3 the top interface is now taken to reflect and transmit the incident intensity diffusely. Again the diffuse intensity is assumed to be the integral of the specularly reflected and transmitted Fresnel flux, or stated algebraically

$$i(\tau_o, -\mu) = 2\int_o^1 \rho_{21}(\mu)\, i(\tau_o,\mu)\mu d\mu$$

$$+ 2\int_{\mu_c}^1 [1 - \rho_{12}(\mu_1)]\mu_1 d\mu_1 \tag{15}$$

and

$$i(o,\mu) = \rho_{23}(\mu)\, i(o, -\mu) \quad . \tag{16}$$

where μ_c is the cosine of the critical angle.

Diffuse Reflector and Transmitter on a Diffuse Substrate

Case 4 is the same as case 3 except that case 4 has a diffuse substrate; the associated boundary conditions are

$$i(\tau_o, -\mu) = 2\int_o^1 \rho_{21}(\mu) i(\tau_o,\mu)\mu d\mu$$

$$+\int_{\mu_c}^1 [1 - \rho_{12}(\mu_1)]\mu_1 d\mu_1 \tag{17}$$

and

$$i(o,\mu) = 2\int_o^1 \rho_{23}(\mu) i(o, -\mu)\mu d\mu \tag{18}$$

Diffuse Reflector and Specular Transmitter on a Specular Substrate

Case 5 is based on the experimental results of [5]; the vacuum-deposit interface is assumed to transmit the radiation incident upon the interface from either side in accordance with Snell's law and Fresnel's law. It is assumed that the intensity incident upon the interface from either side is reflected diffusely. The boundary conditions may be stated as

$$i(\tau_o, -\mu) = 2\int_o^1 \rho_{21}(\mu) i(\tau_o,\mu)\mu d\mu + [1 - \rho_{12}(\mu_1)]n^2 \tag{19}$$

and

$$i(o,\mu) = \rho_{23}(\mu) i(o, -\mu) \tag{20}$$

Diffuse Reflector and Specular Transmitter on a Diffuse Substrate

By changing the substrate from specular to diffuse, case 6 is obtained from case 5. Case 6 has the following boundary conditions

$$i(\tau_o, -\mu) = 2\int_o^1 \rho_{21}(\mu)i(\tau_o,\mu)\mu d\mu + [1 - \rho_{12}(\mu_1)]n^2 \tag{21}$$

and

$$i(o,\mu) = 2\int_o^1 \rho_{23}(\mu)i(o, -\mu)\mu d\mu \tag{22}$$

CHAPTER IV

SOLUTION OF TRANSPORT EQUATION

The solution of the radiation transport equation, Equation 7, is accomplished by the method of discrete ordinates. The integrodifferential equation is reduced to a system of simultaneous linear differential equations by replacing the integral term by a Gaussian quadrature. The quadrature has the form [18]

$$\int_{-1}^{1} f(x)\,dx = \sum_{j=1}^{p} a_j\, f(x_j) \tag{23}$$

where x_j are the discrete ordinates whose values depend on the order of the quadrature, p, and a_j are the weighting factors. With this substitution, Equation 7 becomes

$$\frac{di(\tau,\mu_\ell)}{d\tau} = \frac{-i(\tau,\mu_\ell)}{\mu_\ell} + \frac{W}{2\mu_\ell} \sum_{j=1}^{p} a_j\, i(\tau,\mu_j) \tag{24}$$

where $\ell = 1, \ldots\ldots, p$.

Thus Equation 7 has been reduced to a system of simultaneous linear differential equations. Two types of quadratures have been employed by various authors. Love and Hsia [9] have applied the quadrature formulas separately to the ranges of -1 to 0 and 0 to 1. Love [19] has demonstrated that, for the isothermal case, the three coordinate approximations on μ is quite accurate; this is equivalent to using 6 points in the range from -1 to 1, Love and Hsia [9] used the equivalent of 8 quadrature points in the range from -1 to 1. Wolf [13] used the single Gaussian quadrature of eighth order which has the form Equation 23. Merriam [11] also employed the single Gaussian quadrature and 24 quadrature points were used in Equation 23. Hottel, et al. [10] mentioned that some authors prefer to split up the integral from -1 to 0 and 0 to 1 because of the discontinuity in intensity at $\mu = 0$ at the bounding surfaces, and also pointed out that this complication results in no improvement of accuracy. In Reference [10] the single Gaussian quadrature of orders 4, 12, 20, and 24 were employed. The results presented for the comparison of different orders of quadrature showed that the intensity field varied only slightly as the order of quadrature was increased from 4 to 24. Based on these results and an effort to obtain a computer program which would converge in a reasonable amount of computer time, it was decided to use the single Gaussian quadrature, Equation 23, of order 10 for the hemispherical-angular reflectance calculations.

After the transport equation, Equation 7, was reduced to a system of differential equations, Equation 24, it was decided to solve the system by the Milne predictor-corrector method. The number of steps used in the numerical integration was varied from 50 to 200; however, most of the results presented were calculated with 50 steps for the range

$0 \leq \tau_o \leq 5.0$. The mathematical expressions of the predictor-corrector method from [20] adapted to $i(\tau,\mu_\ell)\,[\ell = 1, \ldots, p/2]$ are

Predictor

$$i(\tau_{n+1},\mu_\ell) = i(\tau_{n-3},\mu_\ell) + \frac{4h}{3}\left[2\frac{di}{d\tau}(\tau_n,\mu_\ell) - \frac{di}{d\tau}(\tau_{n-1},\mu_\ell) + 2\frac{di}{d\tau}(\tau_{n-2},\mu_\ell)\right] \quad (25)$$

Corrector

$$i(\tau_{n+1},\mu_\ell) = i(\tau_{n-1},\mu_\ell) + \frac{h}{3}\left[\frac{di}{d\tau}(\tau_{n-1},\mu_\ell) + 4\frac{di}{d\tau}(\tau_n,\mu_\ell) + \frac{di}{d\tau}(\tau_{n+1},\mu_\ell)\right] \quad (26)$$

and for $i(\tau,\mu_\ell)\,[i = \frac{p}{2} + 1, \ldots, p]$

Predictor

$$i(\tau_{m-1},\mu_\ell) = i(\tau_{m+3},\mu_\ell) + \frac{4h}{3}\left[2\frac{di}{d\tau}(\tau_m,\mu_\ell) - \frac{di}{d\tau}(\tau_{m+1},\mu_\ell) + 2\frac{di}{d\tau}(\tau_{m+2},\mu_\ell)\right] \quad (27)$$

Corrector

$$i(\tau_{m-1},\mu_\ell) = i(\tau_{m+1},\mu_\ell) + \frac{h}{3}\left[\frac{di}{d\tau}(\tau_{m+1},\mu_\ell) + 4\frac{di}{d\tau}(\tau_m,\mu_\ell) + \frac{di}{d\tau}(\tau_{m-1},\mu_\ell)\right] \quad (28)$$

where $n = 4, 5, \ldots N$ and $m = N - 4, N - 3, \ldots 1$ and where N is the number of stations employed in marching from 0 to τ_o and h is the step size ($\tau_o/[N - 1]$).

In order to use Equation 25, the derivatives at τ_n, τ_{n-1}, and τ_{n-2} must be known. These values can be determined directly from the given differential equation only after the corresponding values at τ_1, τ_2, τ_3, and τ_4 are known. Hence, a starting equation must be used in order to obtain these needed preliminary estimates. The starting method used was the modified Euler method which will be described shortly. For the quadrature points $\ell = 1, \ldots, p/2$ Equation 25 estimates a value of $i_{pr}(\tau_{n+1},\mu_\ell)$; Equation 26 corrects this estimate. The new values of $i_{co}(\tau_{n+1},\mu_\ell)$ thus found can in their turn be used as a new estimated value and Equation 26 used over again to correct it. It has been proven that, if the original estimate is not too far away from the true value, and if h is sufficiently small, the repeated use of Equation 26 will yield a sequence of values of $i_{co}(\tau_{n+1},\mu_\ell)$ which will converge. Equations 27 and 28 are similarly used for the quadrature points $\ell = p/2 + 1, \ldots, p$.

It was found that in the range $0 \leq \tau_o \leq 5.0$ the corrector only had to be used repeatedly at $\tau_o = 5$ for 50 steps or 51 stations. However, one may use less steps and possibly use the corrector repeatedly at more stations. The fastest method is dependent on one's experience with the problem at hand.

For the evaluation of the values at the first four τ stations the modified Euler method of [21] was used. Basically the modified Euler technique is for $i(\tau,\mu_\ell)[\ell = 1, ..., p/2]$

$$i(\tau_{n+1},\mu_\ell) = \frac{h}{2}\left[\frac{di}{d\tau}(\tau_n,\mu_\ell) + \frac{di}{d\tau}(\tau_{n+1},\mu_\ell)\right] \quad (29)$$

where n = 1, 2, 3 and for $i(\tau,\mu_\ell)[\ell = p/2 + 1, ..., p]$

$$i(\tau_m,\mu_\ell) = \frac{h}{2}\left[\frac{di}{d\tau}(\tau_{m-1},\mu_\ell) + \frac{di}{d\tau}(\tau_m,\mu_\ell)\right] \quad (30)$$

where m = N - 1, N - 2, N - 3.

I. DESCRIPTION OF ITERATION SCHEME

Since the current problem is a boundary-valued problem, even before the modified Euler technique can be employed, it is necessary to make an initial guess at the intensity field at the vacuum-deposit interface. It would be advantageous to develop an algebraic expression to deploy in a computer program for the purpose of providing this initial guess. The actual expression for the initial guess equation will be presented in Chapter VII. For present purposes it is only necessary to mention that the initial guess expressions are of the forms:

$$i(\tau,\mu) = f(\tau,\mu,W,\tau_o,\rho_{12},\rho_{23},\rho_{21},n) \quad (31)$$

$$i(\tau, -\mu) = g(\tau,\mu,W,\tau_o,\rho_{12},\rho_{23},\rho_{21},n) \quad (32)$$

Thus for all of the given input parameters it is possible not only to estimate the dimensionless intensity field in the quadrature directions μ_ℓ at τ_o, but also to estimate the entire field in the quadrature directions at any τ station.

After many attempts at how to best make an initial guess, it was decided to use equations having the form of Equations 31 and 32 to guess the intensity field at each of the N stations corresponding to τ in each of the p quadrature directions corresponding to μ.

The actual iteration routine used was a forward and backward integration scheme. An outline of the iteration scheme proceeds as follows:

1. The input parameters such as refractive indices, optical thickness, and albedo are chosen.
2. The interval between 0 and τ_o is divided into equal intervals at N stations and the order, p, of the single Gaussian quadrature is selected.
3. Equations 31 and 32 are used to obtain an initial guess of the entire dimensionless radiation field in the quadrature directions at every τ station including $\tau = 0$ and $\tau = \tau_o$, such as the guesses $i(\tau_o, \mu_\ell)$ $[\ell = 1, \ldots, p/2]$.
4. Now Equation 24, $[\ell = p/2 + 1, \ldots, p]$ is integrated backward (downward) over τ from τ_o to 0 by holding the guessed values of $i(\tau, \mu_\ell)$ $\ell = 1, \ldots, p/2$ constant and calculating new values

of $i(\tau,\mu_\ell)[\ell = p/2 + 1, \ldots, p]$ by use of Equations 27, 28, and 30.

5. After arriving at $\tau = 0$ the boundary conditions presented in Chapter III are used to compute new values of $i(0,\mu_\ell)[\ell = 1, \ldots, p/2]$.

6. Now Equation 24 $[\ell = 1, \ldots, p/2]$ is integrated forward (upward) from 0 to τ_o by holding the newly calculated $i(\tau,\mu_\ell)[\ell = p/2 + 1, \ldots, p]$ values constant and computing new values of $i(\tau,\mu_\ell)[\ell = 1, \ldots, p/2]$ through use of Equations 25, 26, and 29. After arriving at $\tau = \tau_o$ new values of $i(\tau_o,\mu_\ell)[\ell = 1, \ldots, p/2]$ are available.

7. Next the values of $|i(\tau_o,\mu_\ell)_1 - i(\tau_o,\mu_\ell)_o|_\ell$ $[\ell = 1, \ldots, p/2]$ are compared with a given tolerance (in this case the maximum value had to be less than 0.001). If the difference is greater than the given tolerance the boundary conditions at the vacuum-deposit interface are used to find new values $i(\tau_o,\mu_\ell)[\ell = p/2 + 1, \ldots, p]$, and the entire forward and backward marching process is repeated again beginning with part 4 of this outline.

The marching process is repeated again to find values $i(\tau_o,\mu_\ell)[\ell = 1, \ldots, p/2]$. This procedure is repeated continuously until the maximum difference between two successive iterations is within the given tolerance.

The solution of the system of equations is obtained in terms of the quadrature directions; the intensity is given in a direction which corresponds to one of the μ_ℓ quadrature ordinates. If a solution is desired in a direction which is not a quadrature direction, interpolation or extrapolation must be used among the solutions in the quadrature directions. Likewise, if the flux at a point within the deposit is desired, the integration over intensity can be performed numerically by the same order quadrature as was chosen for Equation 24.

CHAPTER V

THEORETICAL RESULTS

I. CASE 1: SPECULAR REFLECTOR AND TRANSMITTER ON A SPECULAR SUBSTRATE

The physical description of case 1 has been presented in Chapter III. Now the behavior of the theoretical results will be discussed in light of the analytical structure of the model. The boundary conditions for case 1 are given by Equations 10 and 11. The hemispherical-angular reflectance was defined as the intensity reflected in a given viewing direction divided by the diffusely incident intensity, I_o. Expressed mathematically the reflectance $\rho_{ha}(\mu_1)$ for case 1 is

$$\rho_{ha}(\mu_1) = \frac{\rho_{12}(\mu_1)I_o}{I_o} + \frac{[1 - \rho_{21}(\mu)]}{n^2} \frac{I(\tau_o,\mu)}{I_o} \tag{33}$$

or in terms of quadrature directions

$$\rho_{ha}(\mu_{1\ell}) = \rho_{12}(\mu_{1\ell}) + [1 - \rho_{21}(\mu_\ell)]\frac{i(\tau_o,\mu_\ell)}{n^2} \tag{34}$$

where $\mu_c < \mu_\ell < 1$ and $\ell = 1, \ldots, P/2$ and also $\mu_{1\ell}$ and μ_c are related by Snell's law:

$$\mu_{1\ell} = [1 - (1 - \mu_\ell^2)n^2]^{1/2} \tag{35}$$

Figure 7 illustrates the dependence of $\rho_{ha}(\mu_1)$ on

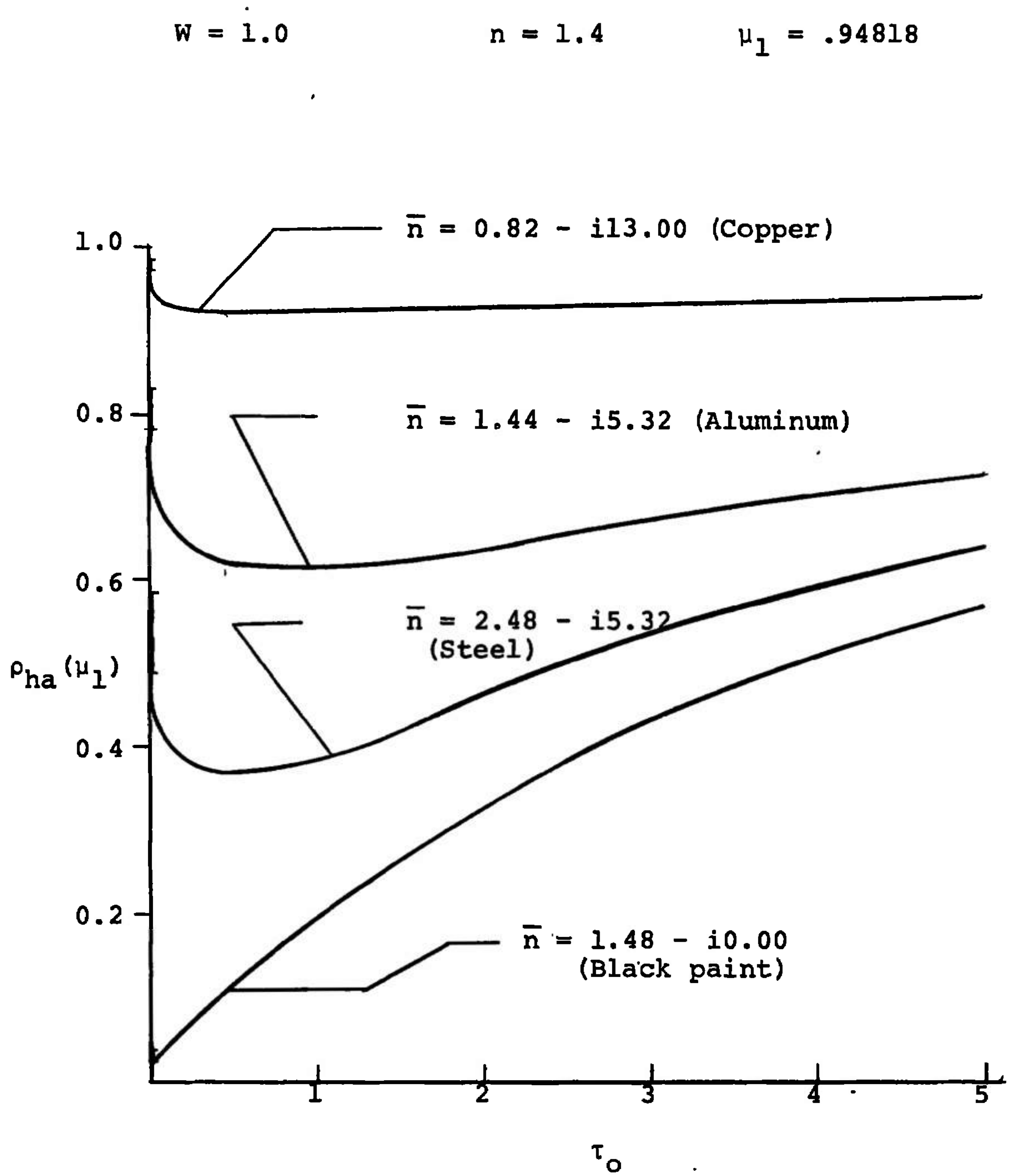

Figure 7. Variation of $\rho_{ha}(\mu_1)$ with τ_o for various substrates for a case 1 deposit.

optical thickness for various substrate reflectances. Of noticeable importance is that even though the film is purely scattering (W = 1.0) the reflectance may decrease before increasing. Initially the bare substrate has a reflectance value $\rho_{ha}(\mu_1) = \rho_{13}(\mu_1)$. The incident radiation goes directly from vacuum to substrate. After a monolayer of molecules has formed the radiation must travel from the vacuum, penetrate through a film whose refractive index is greater than unity and impinge on the substrate. The reflectance is now given by Equation 176. There is a decrease in reflectance because as the radiation penetrates into the deposit the beams of intensity are refracted into directions which are at smaller angles of incidence to the substrate normal than when no deposit was present. In fact, the incident irradiation is contained in $0° < \theta_1 < 90°$, but inside the monolayer film the irradiation (most of which transmits through the vacuum-deposit interface) is now contained in $0° < \theta < \theta_c$. As the angle of incidence between substrate normal and the incident intensity decreases, the reflectance decreases. Thus since the substrate reflectance decreases, the intensity absorbed by the substrate increases. This initial decrease actually appears as a discontinuity. It is interesting to note that both the value given by Equation 176 and the numerical solution converges to the same value by setting $\tau_o = 0$; but of course, use of Equation 176 is obviously more simple. To summarize, this initial drop is due to three effects:

1. Because of refraction the angles of incidence of the intensity at the substrate are reduced thus causing a decrease in reflectance as a result of the more normal incidence angles.
2. It is known that the greater the refractive index ratio between two media, the greater the reflectance. With a bare substrate the refractive index ratio is n_3/n_1 or n_3 since $n_1 = 1$. After the monolayer film forms, the refractive index ratio at the substrate interface is now n_3/n_2 where $n_2 > 1$ (for H_2O $n_2 \simeq 1.2$ and for CO_2 n_2 1.4 in the visible wavelength region). Thus since the refractive index ratio decreases, the reflectance at the substrate decreases. For $n_3/n_1 = 1$ the reflectance is zero for all angles of incidence. So as n_3/n_2 decreases the substrate absorbs more radiation. This phenomena will be referred to as the relative refractive index change and it is believed that this is the principal cause of the initial reflectance drop.
3. The third cause of the decrease is due to the infinite series of reflections which occur at the top and bottom interfaces. After radiation reflects off the substrate it is incident again at the top interface where some is transmitted and a portion is reflected back down toward the substrate; hence the substrate has another

opportunity at the absorption of some of this intensity. At the substrate part is absorbed and a portion is reflected back again toward the top interface. This sets up an infinite series of reflections which gives the substrate many opportunities at absorption of the radiation. This effect is not of major importance but does have a finite contribution to the initial decrease.

Although the three reasons for the initial decrease have been discussed separately, they are really coupled together and can be calculated by Equation 176. Again it should be remembered that the optical thickness involved is so small that the effect of absorption and scattering is negligible for the monolayer deposit.

As the optical thickness begins to increase, $\rho_{ha}(\mu_1)$ decreases again for moderate and highly reflecting substrates. After the diffusely incident intensity penetrates the vacuum-deposit interface all of the transmitted intensity is contained only in the directions $0° < \theta < \theta_c$ for the monolayer deposit. Therefore the region $0° < \theta < \theta_c$ is intensity rich and the directions $\theta_c < \theta < 90°$ are void of radiant energy. Then as the geometric thickness increases further, the deposit begins to approach optical thickness values where absorption and scattering become significant. Of course, for $W = 1$ only scattering occurs. Because the deposit is still very thin, any given beam of intensity will probably only be scattered a few times due to the short path lengths involved. Now that scattering has begun to occur and because the scattering is isotropic, intensity will be scattered in all directions and therefore it is only natural that some energy will be scattered out of the intensity rich directions ($0° < \theta < \theta_c$) and into the void directions ($\theta_c < \theta < 90°$). The intensity in the rich regions has a large likelihood of escaping the deposit; however, intensity scattered into the directions $\theta_c < \theta < 90°$ is incident at the top interface at angles greater than the critical angle and undergoes total internal reflection. This intensity is totally internally reflected, allowing the substrate to have another opportunity at absorption which it did not possess for the monolayer film since the monolayer deposit contained no intensity past the critical angle. This accounts for the second decrease of $\rho_{ha}(\mu_1)$ as the thickness begins to increase. The second decrease for the highly reflecting substrate is small since even though total internal reflection occurs the substrate reflectance is still very high, so most of the intensity scattered past the critical angle is reflected back and forth between the two interfaces and upon traveling back and forth many times may be scattered again into directions less than the critical angle. Thus escape again becomes possible. The moderately reflecting substrates show a larger second decrease since more of the totally internally reflected intensity will be absorbed at these substrates and thus less will be reflected back to make escape possible. The low reflecting substrate does not exhibit this second decrease. The substrate is almost "black," therefore 98 per cent of the intensity incident upon it will be absorbed. Thus for all practical purposes, intensity only impinges on this substrate once and is absorbed. Again isotropic scattering directs intensity in all directions and scatters some energy out of the deposit and some energy past the critical angle. The portion trapped past the critical angle is totally internally reflected and then is effectively totally absorbed by its first encounter with the substrate. Therefore, the energy scattered past the critical angle only has its absorption by the substrate delayed, instead of being absorbed directly like the downward intensity located in directions less than the critical angle. The portion scattered upward at directions less than the critical angle is spared interaction with the highly absorbing substrate and hence escapes the deposit contributing to increasing $\rho_{ha}(\mu_1)$ as the thickness increases. This is why for a highly absorbing substrate $\rho_{ha}(\mu_1)$ is a monotonically increasing function of optical thickness.

It should be noticed that the intensity reflected into the viewing direction is composed of several basic components. For a monolayer deposit the intensity is composed of two components. The first is due to the reflection from the top interface and the second basic component is due to intensity incident upon the substrate and reflected back out of the deposit. After the geometric thickness increases to where scattering is important, a third component of the viewed intensity due to internal scattering must be considered. For the moderate and highly reflecting substrates, the second decrease occurs because intensity is scattered from the second component into all directions including directions past the critical angle. The intensity scattered from other directions into the reference direction is not enough to replenish that which has been scattered out of the reference direction. For the black paint substrate the second component is essentially zero since practically nothing reflects from the substrate. As scattering becomes prominent the intensity reflected from the top interface is supplemented by the internal scattering of the intensity transmitted downward through the top interface. Thus the reflectance becomes a monotonically increasing function of optical thickness.

As the optical thickness increases further (for moderate to highly reflecting substrates) there arrives a thickness at which the totally reflected intensity has a large likelihood of being rescattered, thus being scattered into directions less than the critical angle and hence escaping the deposit. Also as the thickness increases further, scattering becomes more and more predominant thus permitting less energy to penetrate to the absorbing substrate and therefore causing $\rho_{ha}(\mu_1)$ to increase steadily as the thickness increases. It would appear that if a highly scattering deposit approaches a $\rho_{ha}(\mu_1)$ value independent of the substrate, it must do so at a very large optical thickness.

Figure 8 illustrates the refractive index effect on $\rho_{ha}(\mu_1)$. The higher refractive index film has a greater initial decrease corresponding to the greater relative refractive index decrease. The reflection at other thicknesses is less for the higher refractive index because the critical angle is smaller. The smaller critical angle produces more trapping and the higher refractive index causes more direct angles of incidence on the substrate due to greater refraction.

One of the criteria in choosing an analytical model for the cryodeposit is its $\rho_{ha}(\mu_1)$ dependence on viewing angle. Figure 9 shows that as the viewing angle increases, $\rho_{ha}(\mu_1)$ also increases. The angular dependence is stronger for a highly absorbing substrate and becomes weaker as the substrate reflectance increases. The reflectance is greater at larger viewing angles due to the Fresnel reflection of the top interface and also due to the augmentation as a result of scattering associated with longer path lengths. The initial decrease shows essentially the same angular dependence as the Fresnel reflectance of the substrate. The Fresnel curves demonstrate a strong angular variation for dielectrics and indicates an almost totally flat curve for metals.

Figure 10 indicates the dependence of $\rho_{ha}(\mu_1)$ on optical thickness as a function of albedo. For values of

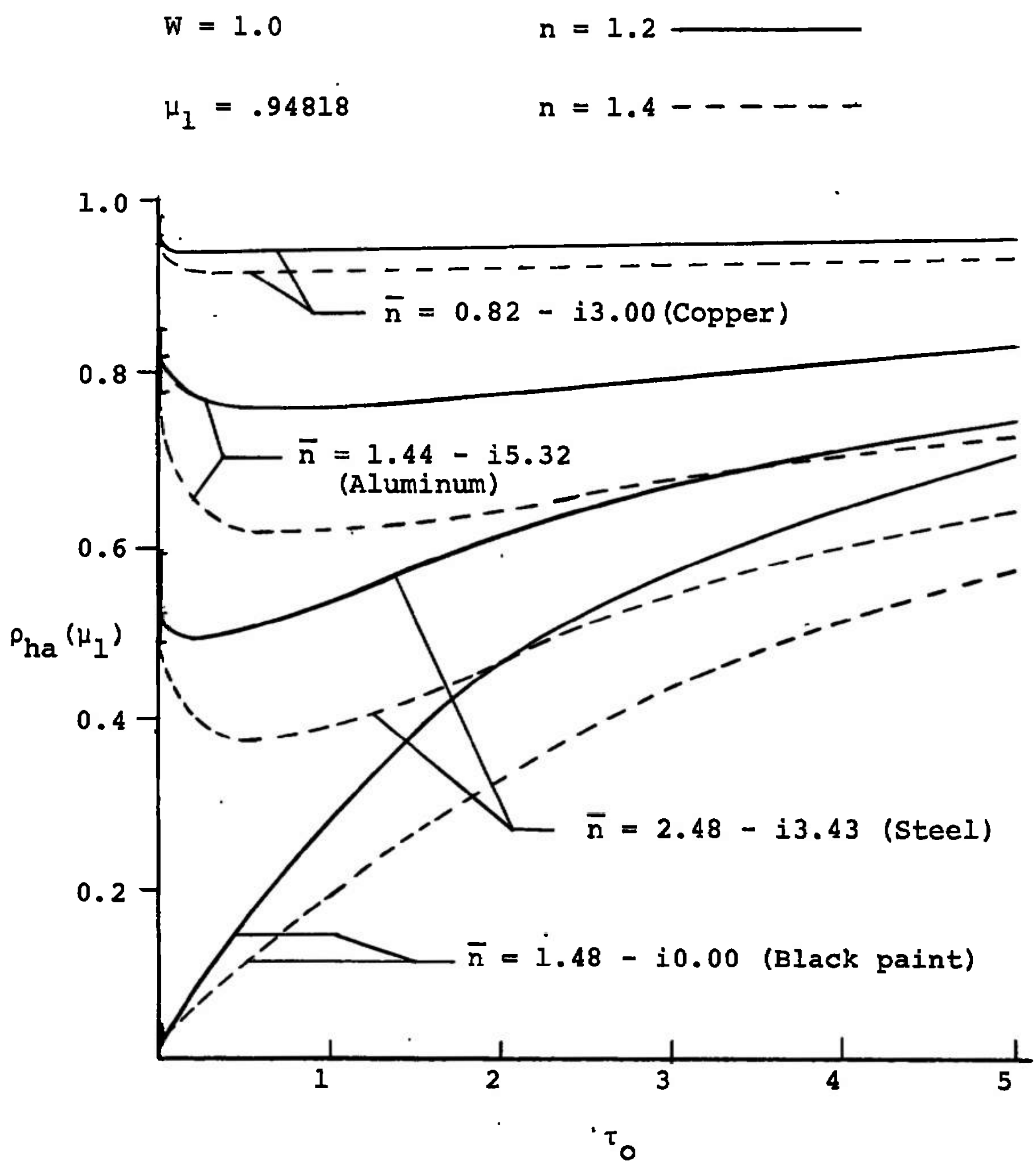

Figure 8. Effect of refractive index on $\rho_{ha}(\mu_1)$ for a case 1 film.

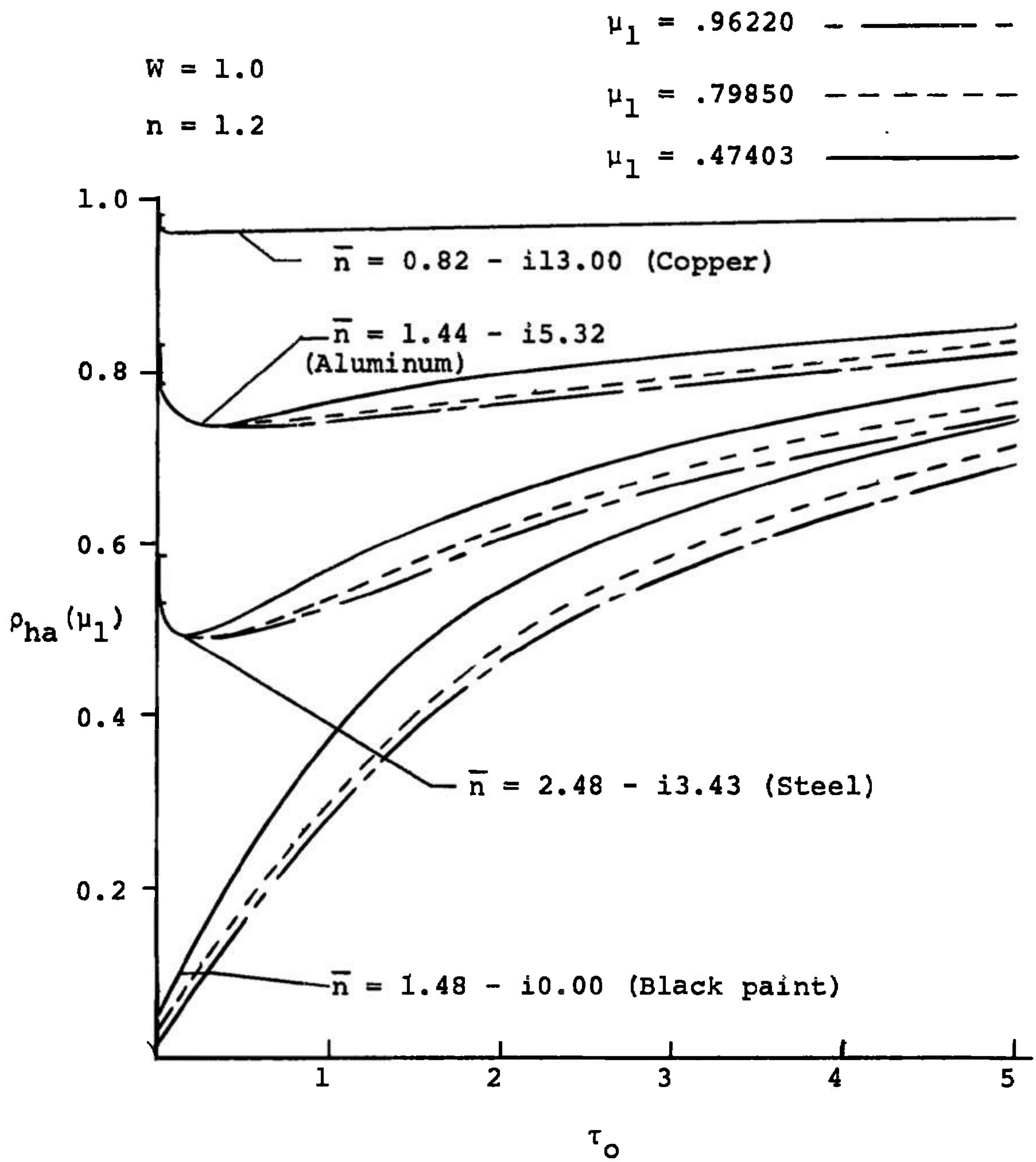

Figure 9. Viewing angle dependence of $\rho_{ha}(\mu_1)$ for a case 1 film for various substrates as a function of optical thickness.

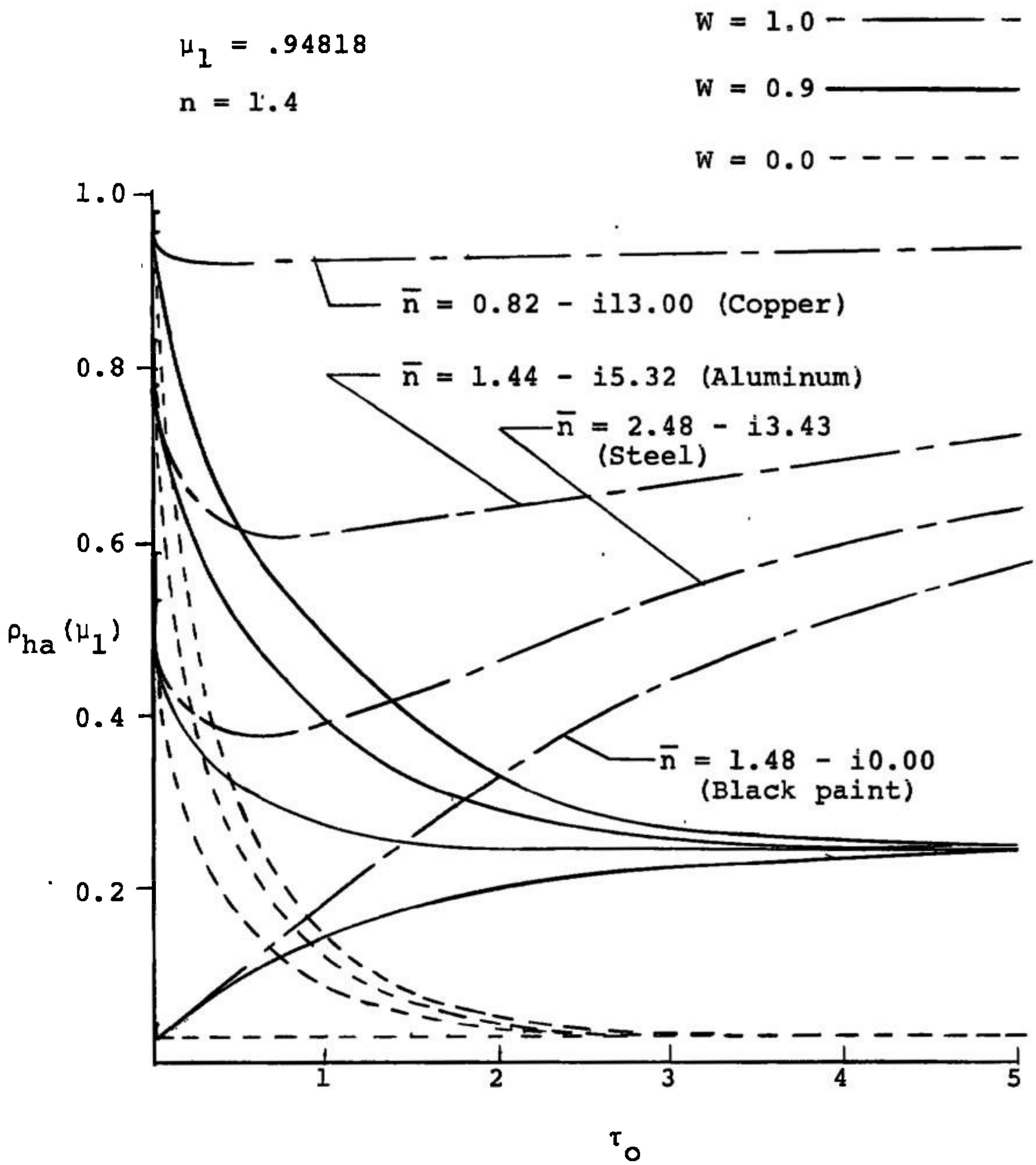

Figure 10. Dependence of $\rho_{ha}(\mu_1)$ on optical thickness as a function of albedo, W, for a case 1 deposit.

$0 < W < 0.9$ the reflectance becomes independent of the substrate for a sufficiently large optical thickness. As W increases the τ_o required for a limiting ρ_{ha} value also increases. If the radiative and optical properties of a film are known this could be important in determining how thick a coating is necessary to change a highly reflecting surface to a low reflector. Economically this could be of value by preventing valuable coatings from being sprayed or deposited too thick. Finally it should be noted from a comparison of Figure 10 with the experimental data shown in Chapter II, that the area of interest for the cryodeposit in the visible wavelength region is for $0.9 < W < 1.0$. This is also the region in which it was indicated in Chapter II that previous authors have encountered difficulties in obtaining a solution.

Figure 11 shows the angular dependence of the dimensionless intensity field at given values of optical thickness. For the small optical thickness not much scattering has occurred and the critical angle effect is prominent. At angles greater than the critical angle the only intensity present is that which has been scattered into these directions. The intensity for angles less than θ_c is greater because it contains intensity which has been forward and backward scattered and also contains the intensity transmitted through the top interface and reflected from the substrate. Also the intensity in the upward direction is less than the intensity in the downward direction due to the

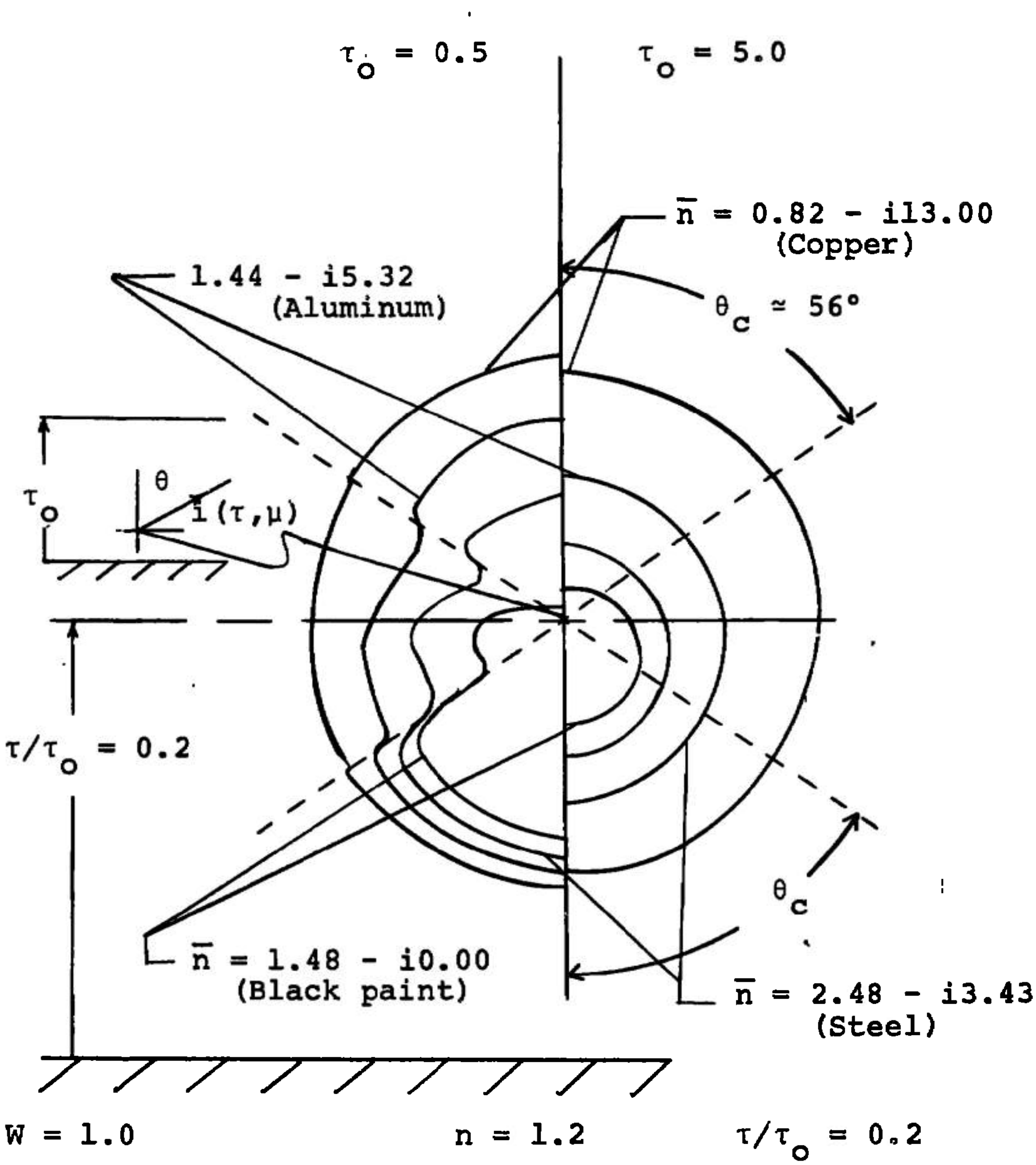

Figure 11. Angular dependence of the dimensionless intensity field, $i(\tau,\mu)$, at fixed points for two optical thicknesses for a case 1 deposit.

substrate absorption. At the large optical thickness the profiles possess no sharp variations since a high degree of scattering has occurred, and likewise the scattering has produced more diffuse intensity distributions.

Figure 12 demonstrates the refractive index effects on the directional intensity profile. The critical angle is smaller for the higher refractive index and the dimensionless intensity is greater due to the solid angle decrease. It is this decrease in the critical angle which causes more trapping of the scattered intensity.

Illustrated in Figure 13 is the dimensionless intensity profiles within the deposit along the quadrature directions. The objective is to transverse a path from the vacuum-deposit interface down to the substrate and then back up again along fixed directions. Two characteristic intensity profiles are labeled (A and B) for explanation purposes. The point C represents the normalized diffusely incident intensity which has a normalized value of unity. Upon crossing the top interface the transmitted intensity undergoes a discontinuous increase by the amount $I_2 = I_1 n^2 [1 - \rho_{12}]$ due to the solid angle decrease. Following direction $\overleftarrow{A}$, the intensity is attenuated due to scattering as it transmits toward the substrate. Arriving at the substrate, E, the intensity is almost totally absorbed by the black paint. A small portion is reflected back in the forward direction, $\vec{A}$, as indicated at point F. As the intensity travels upward toward the top interface it is augmented as a

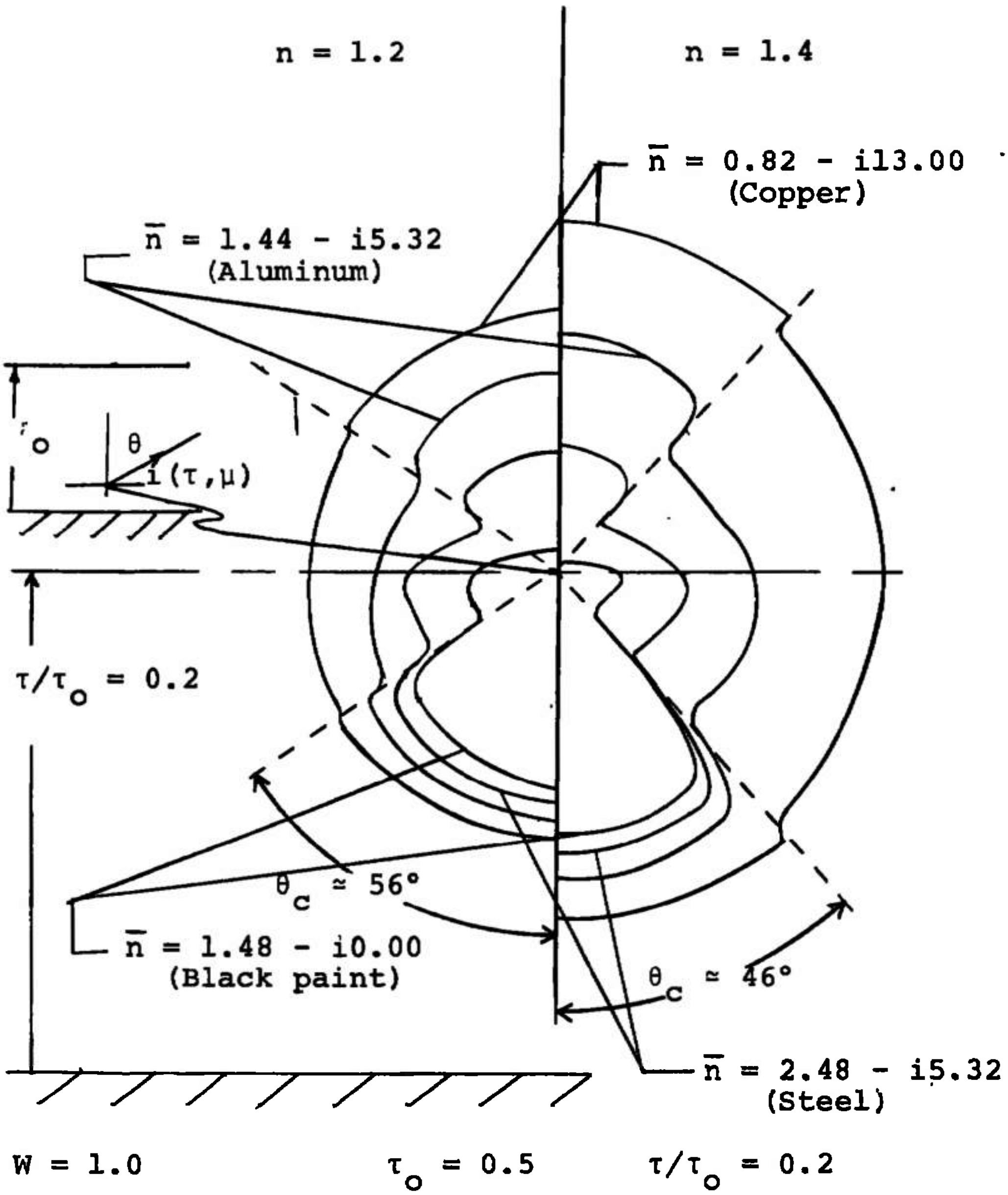

Figure 12. Refractive index effect on the angular distribution of the dimensionless intensity at a fixed point for a case 1 film.

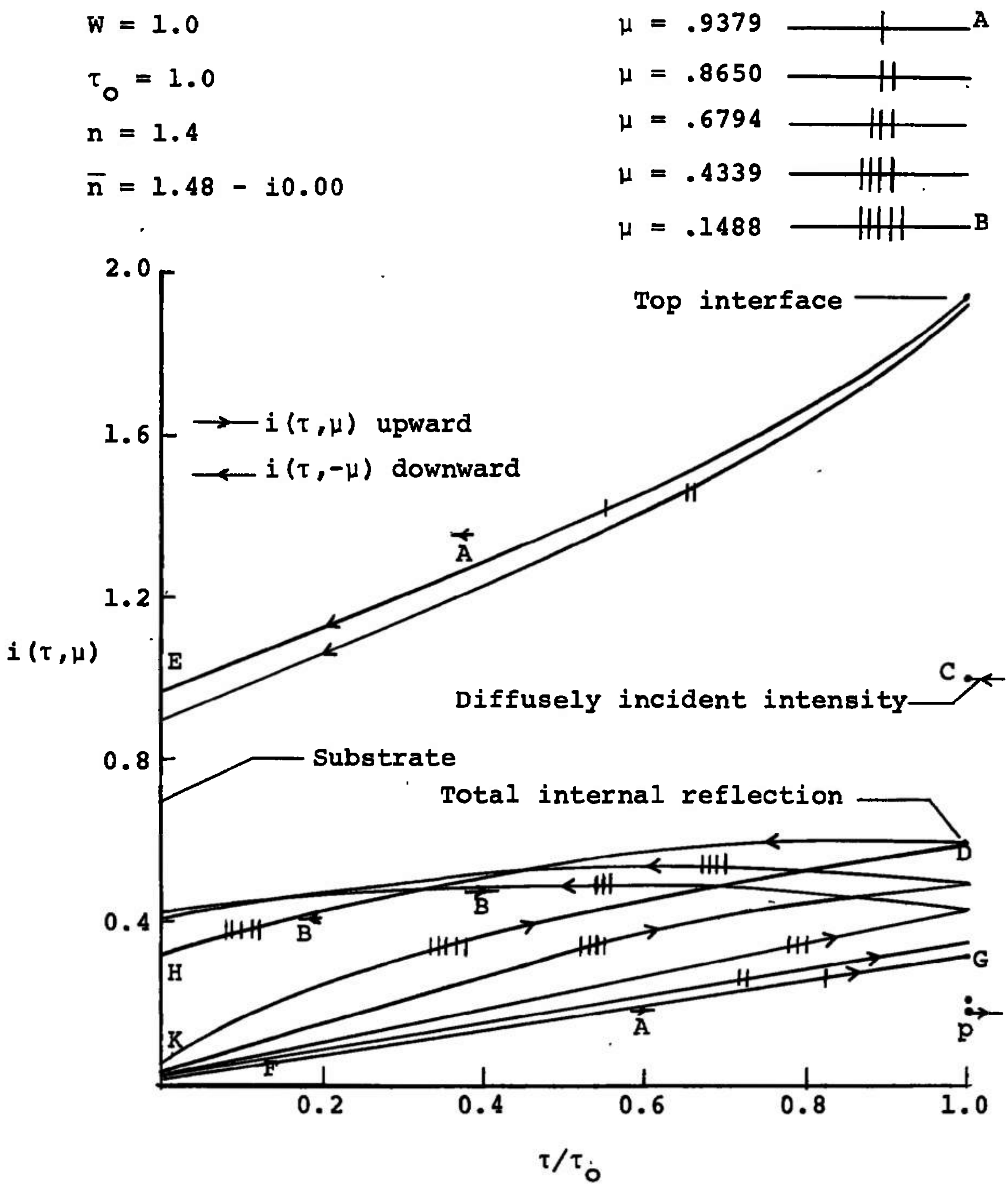

Figure 13. Dimensionless intensity profiles within a deposit along fixed directions for a case 1 film.

result of scattering of the downward intensity into the upward directions. After arriving at the top interface, G, the intensity is reduced discontinuously by the amount $I_1 = (I_2/n^2)[1 - \rho_{21}']$ due to the solid angle increase and attains the value indicated at P. The point P represents the hemispherical-angular reflectance. The curve with two slashes also has the same interpretation except for a different fixed direction.

Curve B represents another characteristic direction. Intensity in this direction is due only to intensity scattered past the critical angle. Beginning at K the intensity increases in the upward direction due to scattering into this direction from other directions. The intensity $\vec{B}$ is totally internally reflected at the top interface, D, since the intensity is incident at a direction greater than the critical angle. After being totally internally reflected, $\overleftarrow{B}$ is attenuated as a result of scattering as it travels toward the substrate. Upon arriving at the substrate, H, the intensity is partially reflected upward as indicated by point K. The curves with three and four slashes have a similar interpretation for other quadrature directions. Also of interest is that the profiles are not highly non-linear which implies that the numerical solution should converge rapidly and not encounter any instabilities associated with rapidly changing slopes.

II. CASE 2: SPECULAR REFLECTOR AND TRANSMITTER ON A DIFFUSE SUBSTRATE

Case 2 is similar to case 1 except that now the substrates are taken to reflect diffusely. The boundary conditions for case 2 are given by Equations 13 and 14. The hemispherical-angular reflectance, ρ_{ha}, is given by Equation 34, but for case 2 $i(\tau_o,\mu_\ell)[\ell = 1, \ldots, p/2]$ will differ significantly from that of case 1.

Since the substrate is diffuse the bare substrate reflectance is given by

$$\rho_{ha}(\mu_1) = 2\int_o^1 \rho_{13}(\mu_1)\mu_1 d\mu_1 \tag{36}$$

or in terms of quadrature integration

$$\rho_{ha}(\mu_{1_\ell}) = \sum_{j=1}^{p} \rho_{13}(z_j)z_j a_j \tag{37}$$

where $y_j = x_j/2 + 1/2$.

Figure 14 depicts the dependence of ρ_{ha} on optical thickness as a function of refractive index. Still noticeable is the initial ρ_{ha} decrease. Case 2 indicates a greater decrease than case 1. The reason is because for the monolayer film of case 1 the substrate is specular, hence intensity can exist only in directions less than θ_c in both the upward and downward directions. For case 2 the intensity transmits through the top interface into angles less

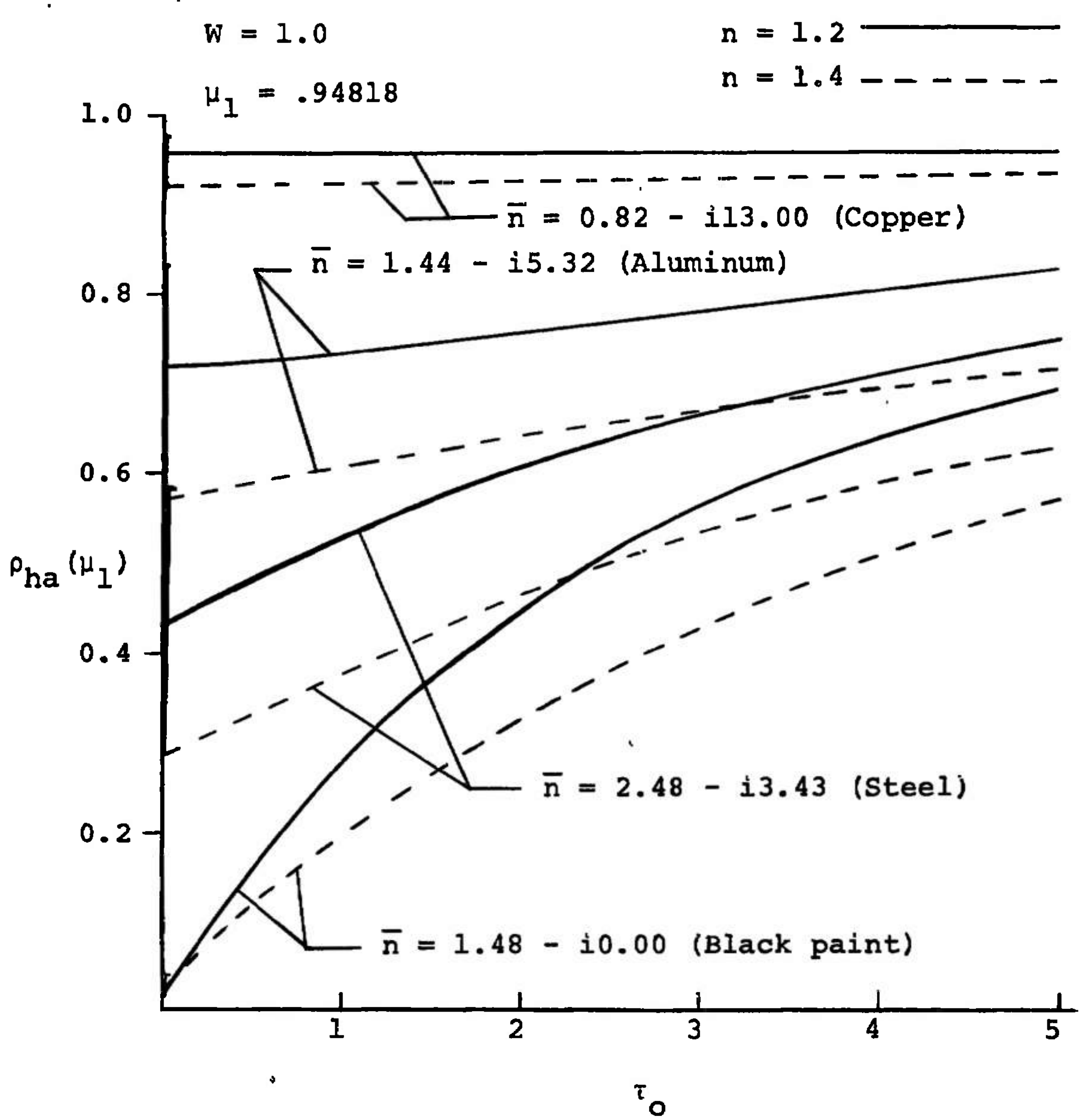

Figure 14. Effect of refractive index on $\rho_{ha}(\mu_1)$ for a case 2 film.

than θ_c; however, after reflection at the substrate, the intensity is directed uniformly into all directions including angles greater than θ_c. When the intensity reflected into angles greater than θ_c is reflected at the top interface these rays undergo total internal reflection and are therefore trapped and reflected back and forth between substrate (partially absorbing) and top interface (totally reflecting) until being almost entirely extinguished. Thus as opposed to case 1, intensity is directed into angles greater than θ_c even before internal scattering becomes appreciable. Since there are no regions void of radiation when the film becomes thick enough for scattering to become significant, the net effect is not to decrease ρ_{ha} due to scattering into $\theta_c < \theta < 90°$, but to increase ρ_{ha} due to scattering intensity from this region, allowing it to escape rather than remain trapped. After the initial decrease, ρ_{ha} becomes a monotonically increasing function of optical thickness. As the thickness increases the isotropic scattering dominates, therefore scattering more and more energy out of the deposit and allowing less energy to penetrate to the substrate. The reflectance is lower for the higher refractive index again due to the increased trapping associated with the smaller critical angle.

Figure 15 shows the same general angular dependence of ρ_{ha} as case 1, that is, ρ_{ha} increases with increasing viewing angles and the strength of the angular dependence decreases as the substrate reflectance increases. At $\tau_o = 0$

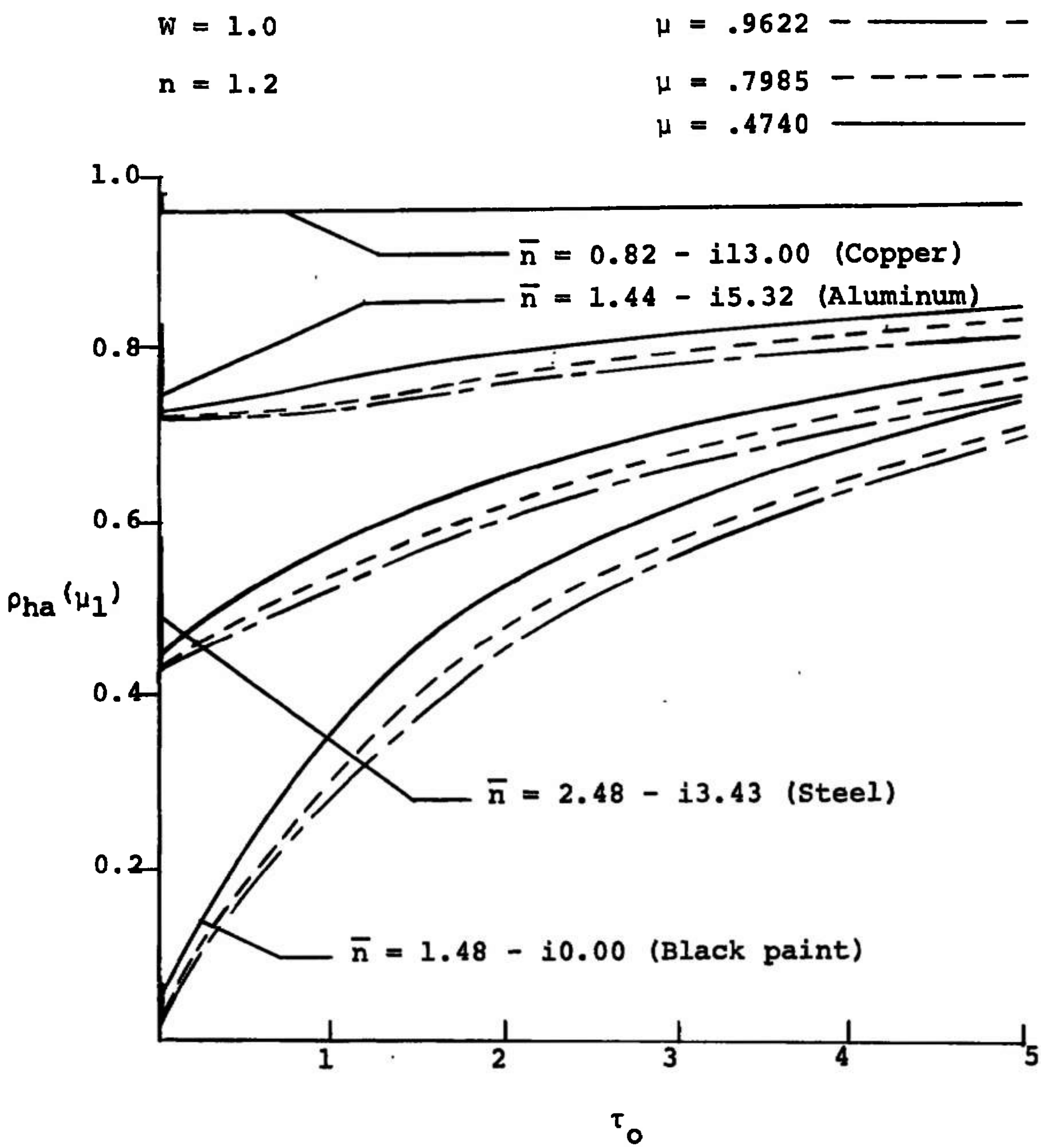

Figure 15. Viewing angle dependence of a case 2 film for various substrates as a function of optical thickness.

there is little angular reflectance dependence. Only a small angular dependence was noticeable due to the Fresnel reflection of the vacuum-deposit interface. Also depicted by Figure 16 is the same quantitative dependence with albedo as in case 1. The limiting τ_o at which ρ_{ha} becomes independent of substrate is about the same as case 1 for an absorbing film. The common value of ρ_{ha} at the limiting optical thickness is also the same. It appears that the diffuse substrate only has an effect (different from case 1) on the reflectance at small optical thicknesses. For the sake of clarity, symbols have been placed along the ordinate scale in order to indicate the difference between the bare substrate reflectance and the reflectance decrease due to the relative refractive index change for the various substrates.

The effect of the diffuse substrate on the angular distribution of the dimensionless intensity at a given point inside the film is illustrated in Figure 17. The intensity in the downward direction is affected by the critical angle phenomena associated with the top surface. The intensity directed upward has a smoother distribution due to the diffuse substrate. In the downward direction the intensity is greater than that in the upward direction due to the absorption of the substrate. Also indicated is the decrease of θ_c for the higher refractive index.

Figures 18 and 19 show the effect of scattering by comparison at two points within a deposit for two different

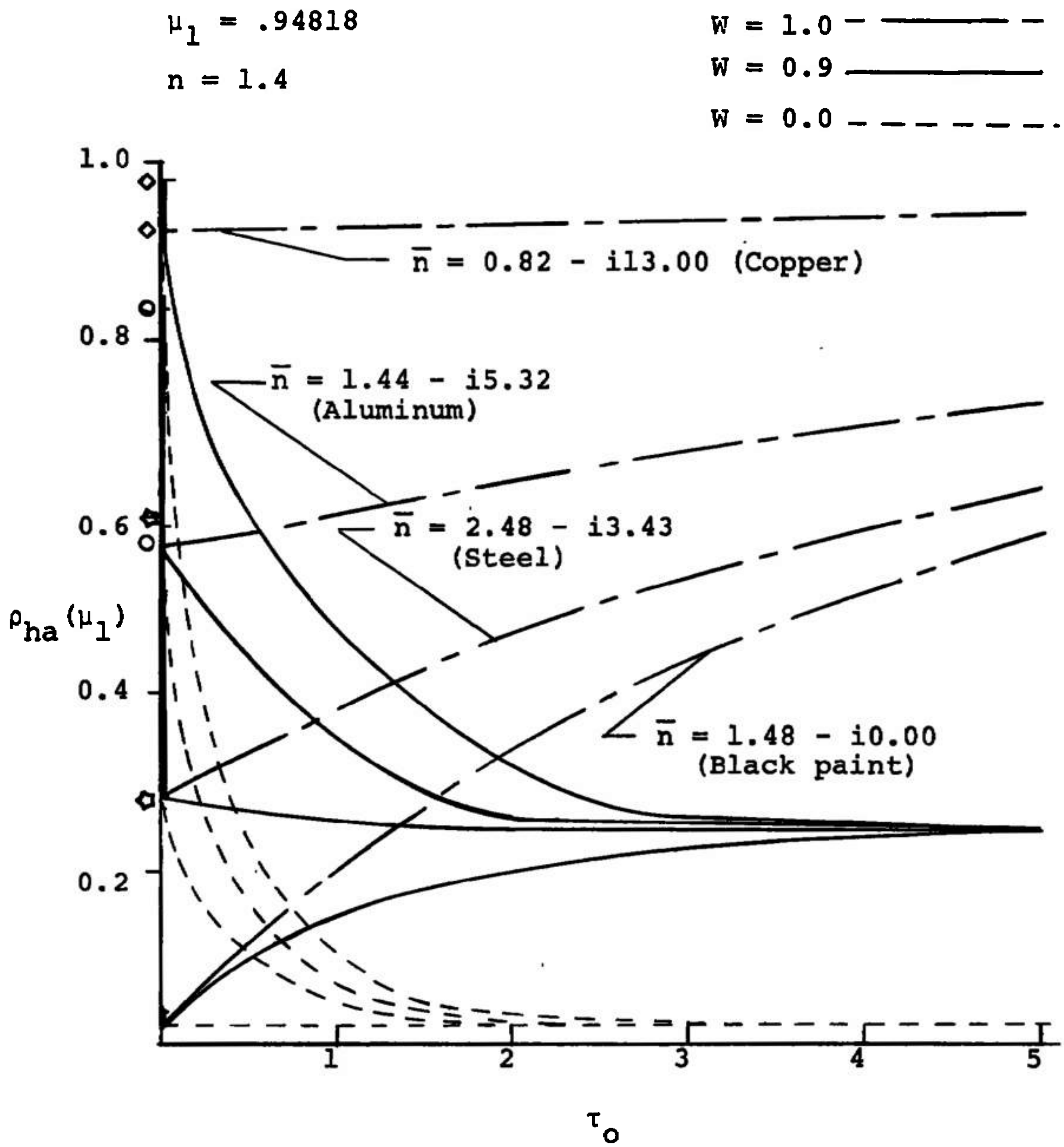

Figure 16. Dependence of $\rho_{ha}(\mu_1)$ on optical thickness as a function of albedo, W, for a case 2 deposit.

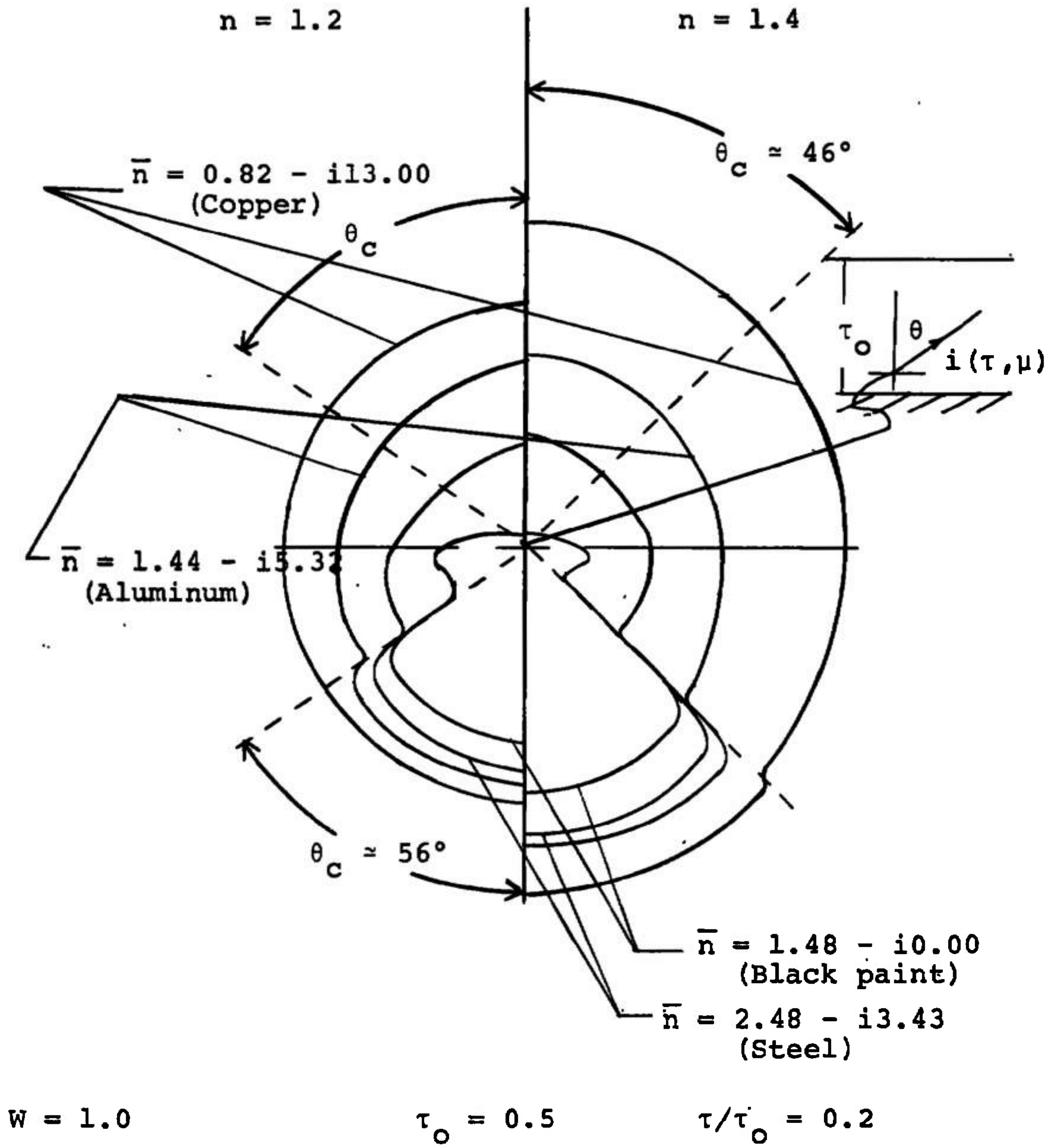

Figure 17. Refractive index effect on the angular distribution of the dimensionless intensity at a fixed point for a case 2 film.

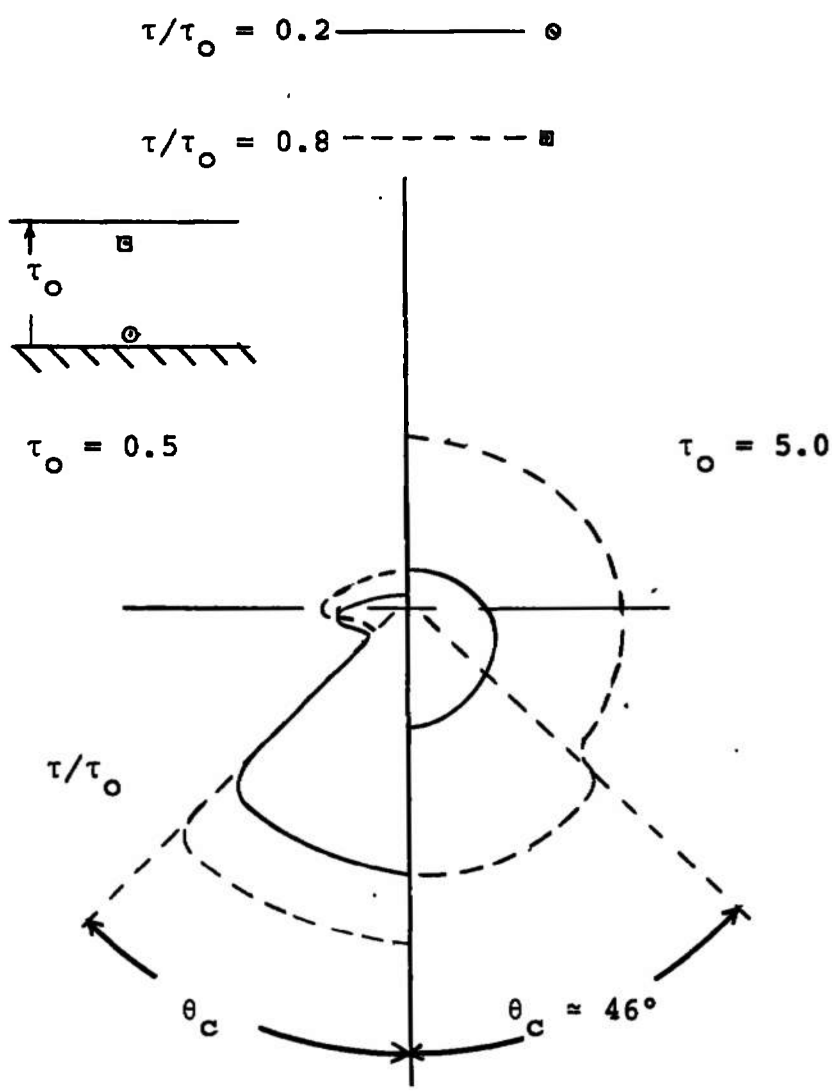

$\bar{n} = 1.48 - i0.00$ $\quad$ $n = 1.4$ $\quad$ $W = 1.0$

Figure 18. Angular distribution of the dimensionless intensity at two points within two case 2 deposits on a black paint substrate.

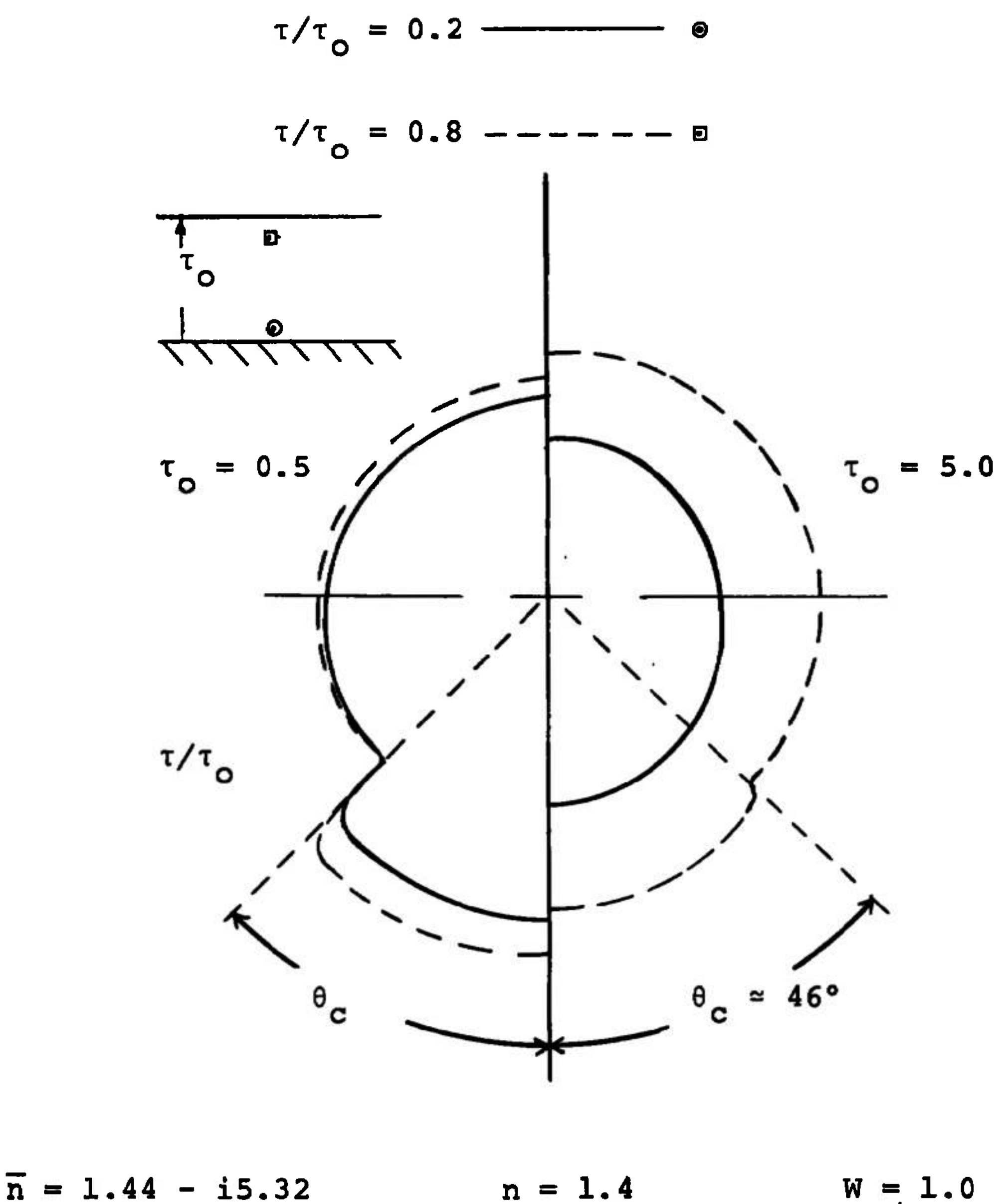

Figure 19. Angular distribution of the dimensionless intensity at two points within two case 2 deposits on an aluminum substrate.

optical thicknesses. Figure 18 shows that for a black paint substrate the shape of the intensity profile is primarily determined by the two interface boundary conditions. The $\tau_o = 0.5$ deposit has the characteristic critical angle effect for intensity directed in the downward direction and the smooth profile for intensity in the upward direction. The intensity in the upward direction at $\tau/\tau_o = 0.8$ is greater than for $\tau/\tau_o = 0.2$ due to more scattering in the forward direction; the intensity is attenuated due to scattering as the rays travel downward. For a large optical thickness, Figure 18 indicates that for a point near the top interface the specular transmission is significant. However for a point near the substrate the intensity profile is very smooth due to the diffuse substrate and the occurrence of substantial scattering.

In both Figures 18 and 19 the enclosed areas can "roughly" be associated with flux. It is obvious that for the thin deposit there is more energy near the substrate than for the thick deposit, and hence more energy is available for absorption by the substrate for the thin deposit. The reason for less energy being available near the substrate for the large deposit is due to attenuation of the rays in the downward direction caused by scattering. Figure 19 shows, in general, the same phenomena except for a moderately reflecting substrate. The main difference here is that the intensity in the upward direction is much greater than in Figure 18 since the substrate is no longer nearly "black."

Illustrated in Figure 20 are the dimensionless intensity profiles for a case 2 deposit. Two characteristic intensity profiles are labeled (A and B). The point C represents the normalized diffusely incident intensity. Upon crossing the top interface, the transmitted intensity undergoes a discontinuous increase due to the solid angle change and due to internal reflection. Following direction $\overleftarrow{A}$, the intensity is attenuated due to scattering as it transmits toward the substrate. Arriving at the substrate, E, the intensity is almost totally absorbed by the diffusely reflecting black paint. A small portion is diffusely reflected back in the forward direction, $\vec{A}$, as indicated at point F; the reflection is seen to be diffuse since the intensity is the same in all directions at the substrate. As the intensity transverses upward it is augmented as a result of scattering. After arriving at G, the intensity is reduced discontinuously, and the hemispherical-angular reflectance is represented by point P.

Curve B represents another characteristic direction. Intensity in this direction is due to intensity scattered past the critical angle and also intensity diffusely reflected from the substrate. Beginning at F the intensity increases in the upward direction due to scattering. The intensity $\vec{B}$ is totally internally reflected at the top interface, D, since the intensity is incident at a direction greater than θ_c. After being totally internally reflected,

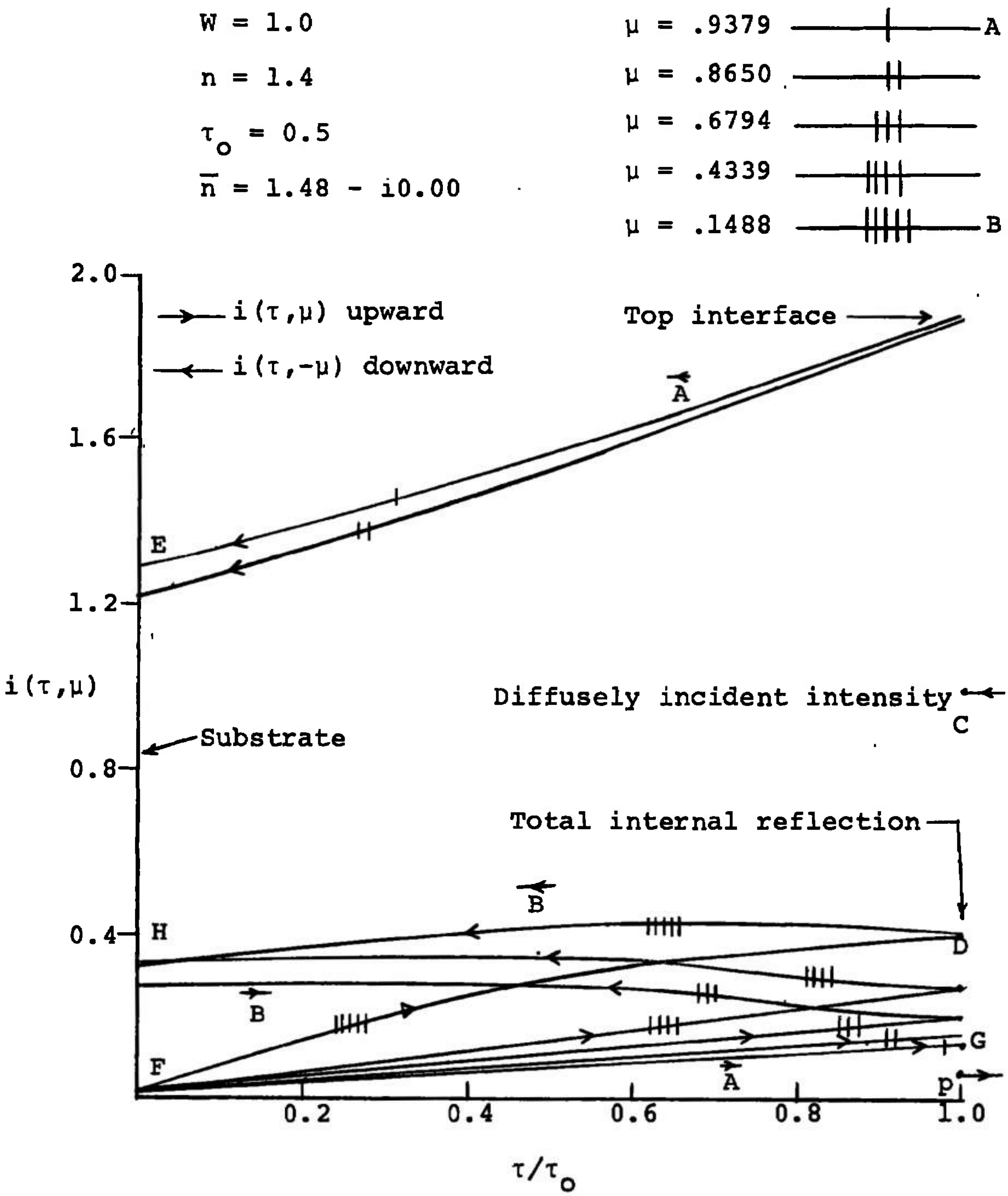

Figure 20. Dimensionless intensity profiles within a deposit along fixed directions for a case 2 film.

$\vec{B}$ is attenuated as a result of scattering as it proceeds toward the substrate, H, where it is diffusely reflected back to point F. Again the profiles are not highly non-linear, indicating the numerical solution should be rapidly convergent and accurate.

Presented in Figures 21 and 22 is a comparison of the specular reflector and transmitter for the two types of substrates--specular and diffuse. Figure 21 shows that the effect of a diffuse substrate is to make the initial decrease greater. Also the difference in $\rho_{ha}(\mu_1)$ between the two cases is only significant at small optical thicknesses. The reflectance at larger optical thicknesses becomes independent of the angular nature of the substrate reflectance. For the black paint substrate even at small thicknesses the ρ_{ha} difference was negligible, as shown. This implies that if a substrate is black it absorbs almost everything incident upon it and that it does not matter whether the reflection occurs diffusely or specularly. The significance is that hemispherical-angular data taken on a black substrate, at this viewing angle, has no dependence on the type of angular reflection which takes place at the substrate; hence the data can be more clearly analyzed in terms of scattering effects without much concern over any substrate effects. At $\tau_o = 0.5$ the reflectance data for a moderate or highly reflecting substrate is very dependent on the angular nature of the substrate reflectance.

Figure 22 illustrates the influence of the critical

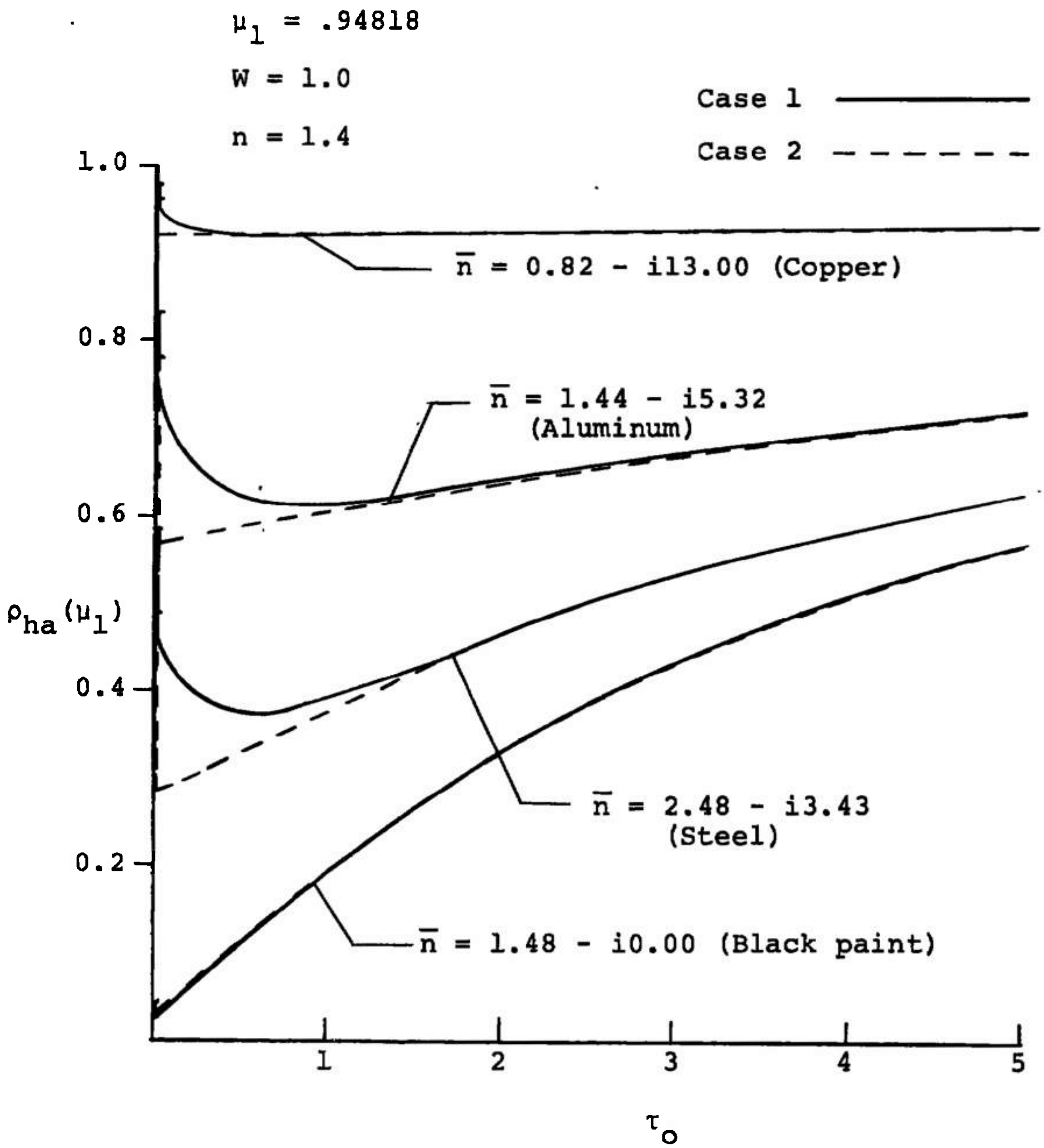

Figure 21. Comparison of case 1 and case 2 deposits for the dependence of $\rho_{ha}(\mu_1)$ as a function of optical thickness.

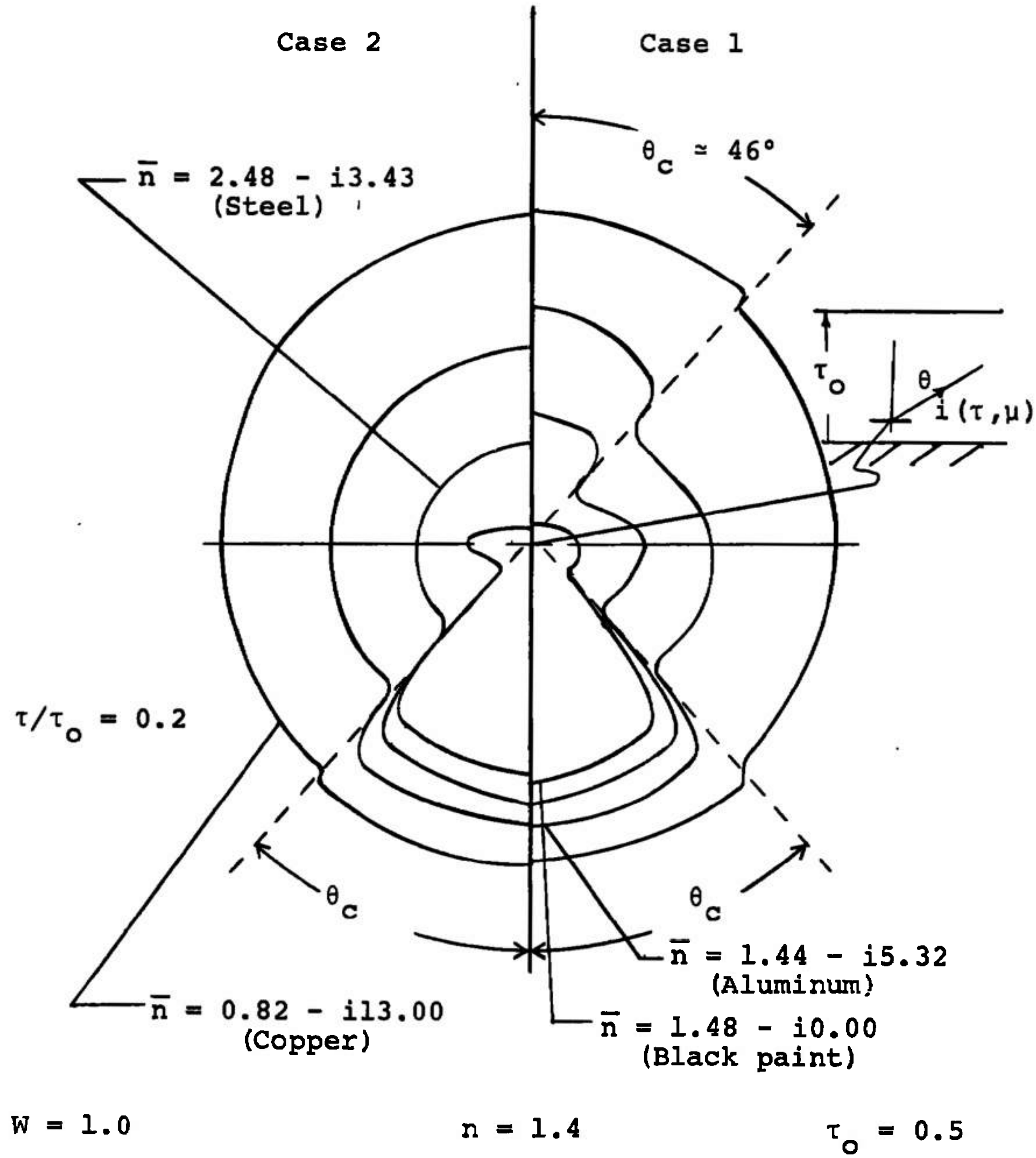

Figure 22. Comparison of the angular distribution of the dimensionless intensity at a fixed point for case 1 and case 2 deposits.

angle phenomena on the downward intensity in both cases. The upward intensity of case 2 has a smooth distribution due to diffuse reflection, and case 1 has the characteristic distribution for specular reflection from the substrate. Also the intensity in the upward direction is greater for the specular substrate than for the diffuse substrate on the moderately reflecting substrates.

III. CASE 3: DIFFUSE REFLECTOR AND TRANSMITTER ON A SPECULAR SUBSTRATE

For case 3 it was assumed that the top interface reflected and transmitted radiation diffusely. As an approximation the diffuse reflector and transmitter should correspond to a geometrically rough surface. This by no means is the best model of a geometrically rough surface; however the development of reflectance and transmission relations for a given degree of mean surface roughness has not yet been developed anywhere near to that of smooth Fresnel surfaces. The model for calculation of the diffuse interface reflectance was proposed in Chapter III. The boundary conditions correspond to Equations 15 and 16. The boundary condition, Equation 15, expressed in terms of the Gaussian quadrature is

$$i(\tau_o,-\mu_\ell) = \sum_{j=1}^{p} \rho_{21}(z_j)\, i(\tau_o,z_j)\, z_j a_j$$

$$+ (1 - \mu_c) \sum_{j=1}^{p} [1 - \rho_{12}(y_j)]y_j a_j \tag{38}$$

where

$$z_j = \frac{x_j}{2} + \frac{1}{2}$$

$$y_j = \frac{(1 - \mu_c)}{2} x_j + \frac{(1 + \mu_c)}{2}$$

and $\ell = 1, \ldots, p/2$.

The values of $i(\tau_o, z_j)$ are not the same as the solutions in the quadrature directions, x_j. The values of $i(\tau_o, z_j)$ are obtained by using a Lagrangian interpolation among the solution in the quadrature directions. The expression for the hemispherical-angular reflectance, ρ_{ha}, is given by

$$\rho_{ha}(\mu_1) = \rho_{ha} = 2 \int_0^1 \rho_{12}(\mu_1)\mu_1 d\mu_1$$

$$+ 2 \int_{\mu_c}^{1} [1 - \rho_{21}(\mu)]i(\tau_o, \mu)\mu d\mu \tag{39}$$

or in terms of quadrature integration

$$\rho_{ha}(\mu_{1_\ell}) = \rho_{ha} = \sum_{j=1}^{p} \rho_{12}(z_j) z_j a_j$$

$$+ (1 - \mu_c) \sum_{j=1}^{p} [1 - \rho_{21}(y_j)]i(\tau_o, y_j) y_j a_j \tag{40}$$

where $\ell = 1, \ldots, p/2$ and z_j and y_j are defined the same as for Equation 38.

Since the interfaces are assumed to be diffuse, there is no viewing angular dependence because by definition the reflection is the same in all directions.

Figure 23 demonstrates that the initial decrease is drastic compared to that of cases 1 and 2. Symbols have been placed along the ordinate scale in order to indicate the difference between the bare substrate reflectance and the reflectance decrease due to the relative refractive index change. The decrease for case 3 is related not only to the relative refractive index change, but also to increased trapping. The intensity transmitted through the top interface is spread uniformily in all directions; some of these directions correspond to extremely long path lengths and are effectively trapped. Also radiation which transmits into near normal directions, after being reflected from the substrate, encounters a high internal reflectance at the top interface, and thus not as much is allowed to escape the film. In cases 1 and 2, for near normal directions, the internal reflectance is almost zero.

As the optical thickness increases and scattering begins to occur, there is an increase in ρ_{ha} due to scattering. Since initially there are no directions void of energy, the scattering contributes monotonically to increasing ρ_{ha} with increasing optical thickness. The higher refractive index deposit has lower ρ_{ha} values because of the

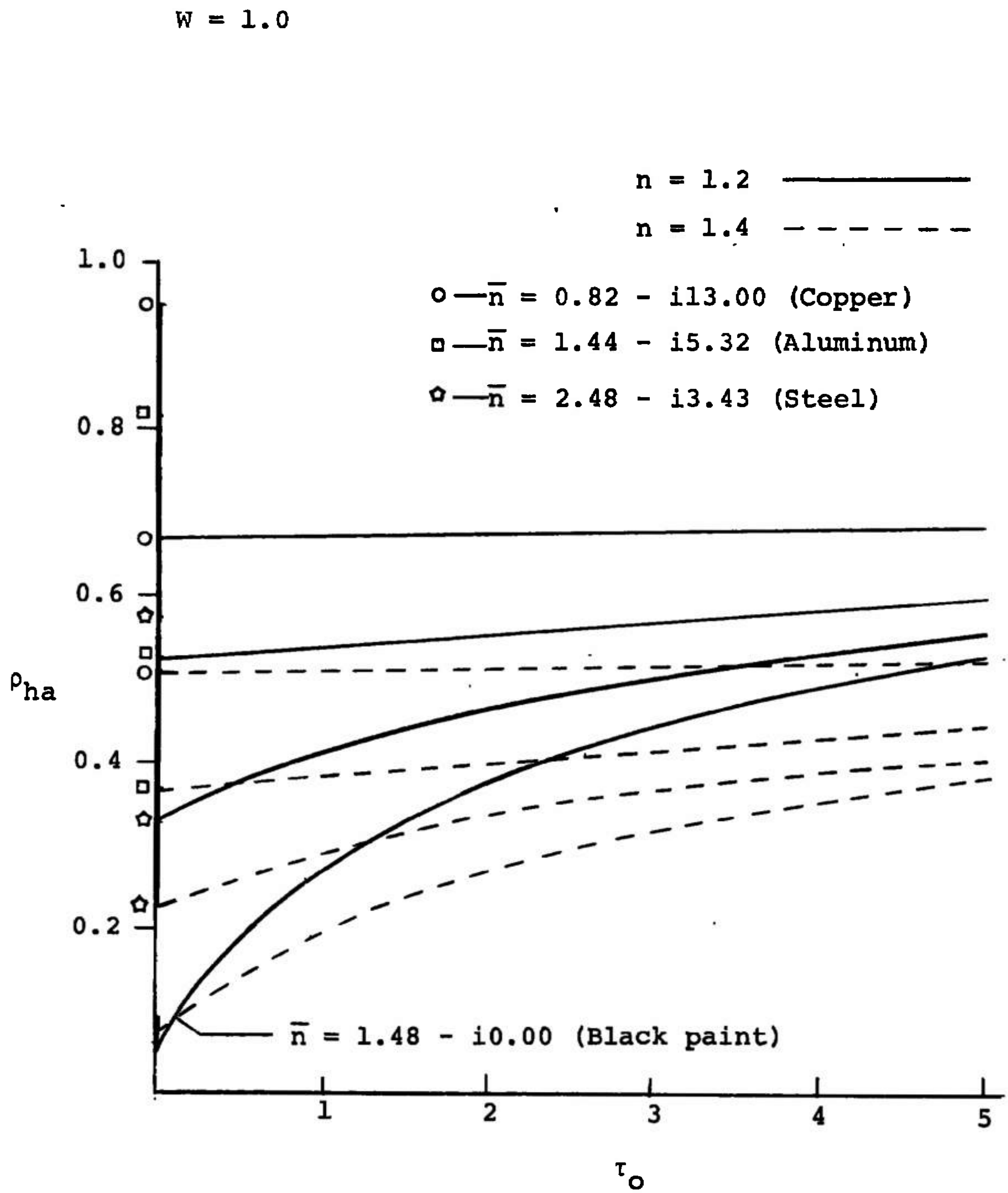

Figure 23. Effect of refractive index on ρ_{ha} for a case 3 film.

influence of the relative refractive index change at the substrate and also because the internal reflectance at the vacuum-deposit interface is higher, thus allowing less energy to escape. The diffuse top interface appears to have a dominating effect on the reflectance since there is not as sharp an increase in ρ_{ha} with optical thickness as in the two previous models. The ρ_{ha} values are substantially lower than for cases 1 and 2 at corresponding τ_o values.

Figure 24 shows the variation of ρ_{ha} as a function of W. The absorbing deposits again approach a common limiting value, but this value is less than that of cases 1 and 2 due to the increased trapping of the diffuse boundaries. Figure 25 indicates the directional intensity profiles are very smooth even for a small optical thickness. This should be expected since the scattering is isotropic and the bounding interfaces are diffuse. Because of the relative refractive index change and the increased internal reflection at the top interface, the intensity for the higher refractive index is the smaller.

Demonstrated by Figure 26 is that the intensity in the upward directions is higher near the top of the deposit than near the bottom due to scattering. Also evident is that for the small optical thickness there is more energy located near the substrate where the absorption occurs. Illustrated in Figure 27 is that for a moderately high reflecting substrate and $\tau_o = 0.5$, the intensity profiles are almost uniform throughout the deposit. For $\tau_o = 5.0$

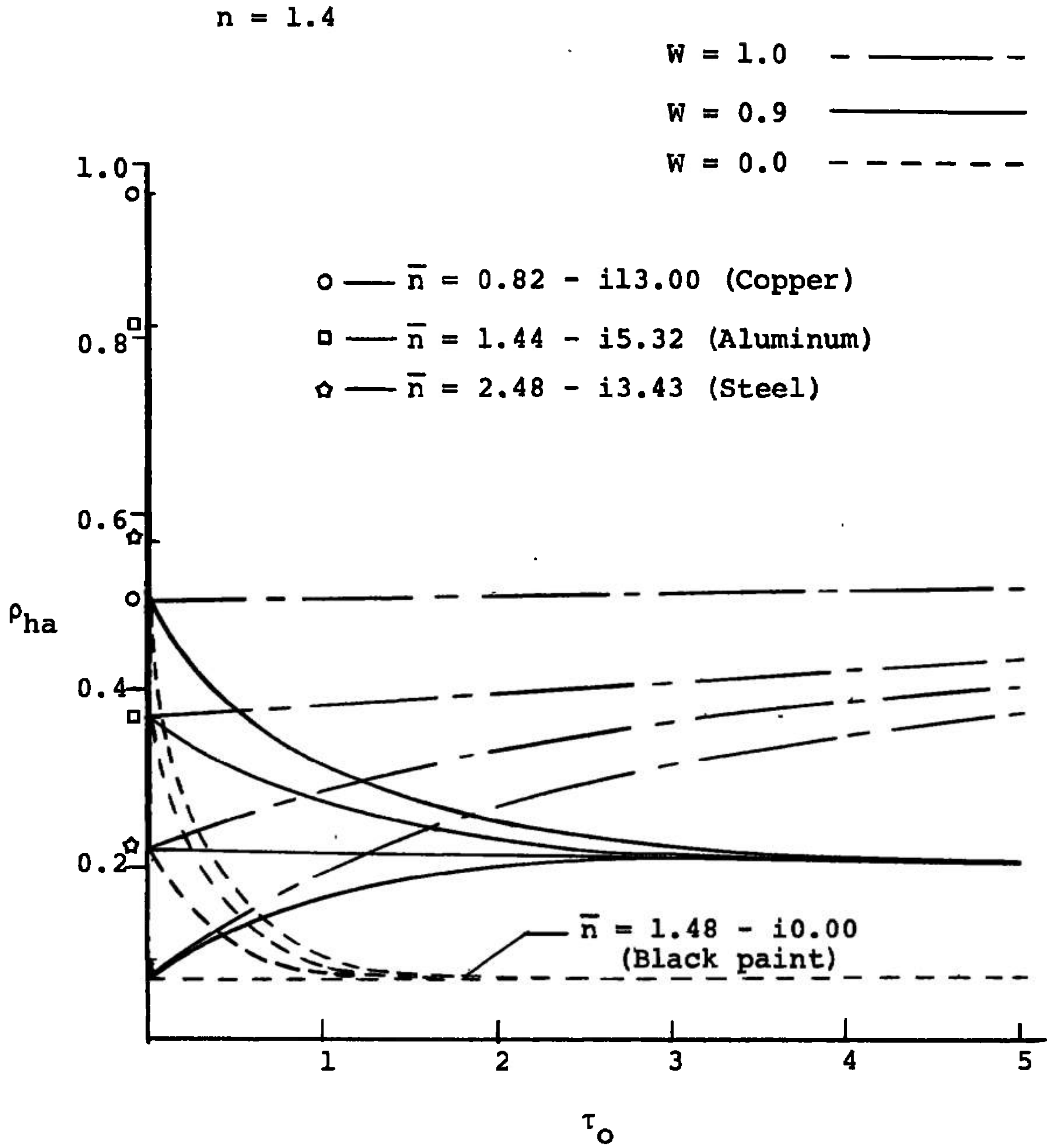

Figure 24. Dependence of ρ_{ha} on optical thickness as a function of albedo, W, for a case 3 deposit.

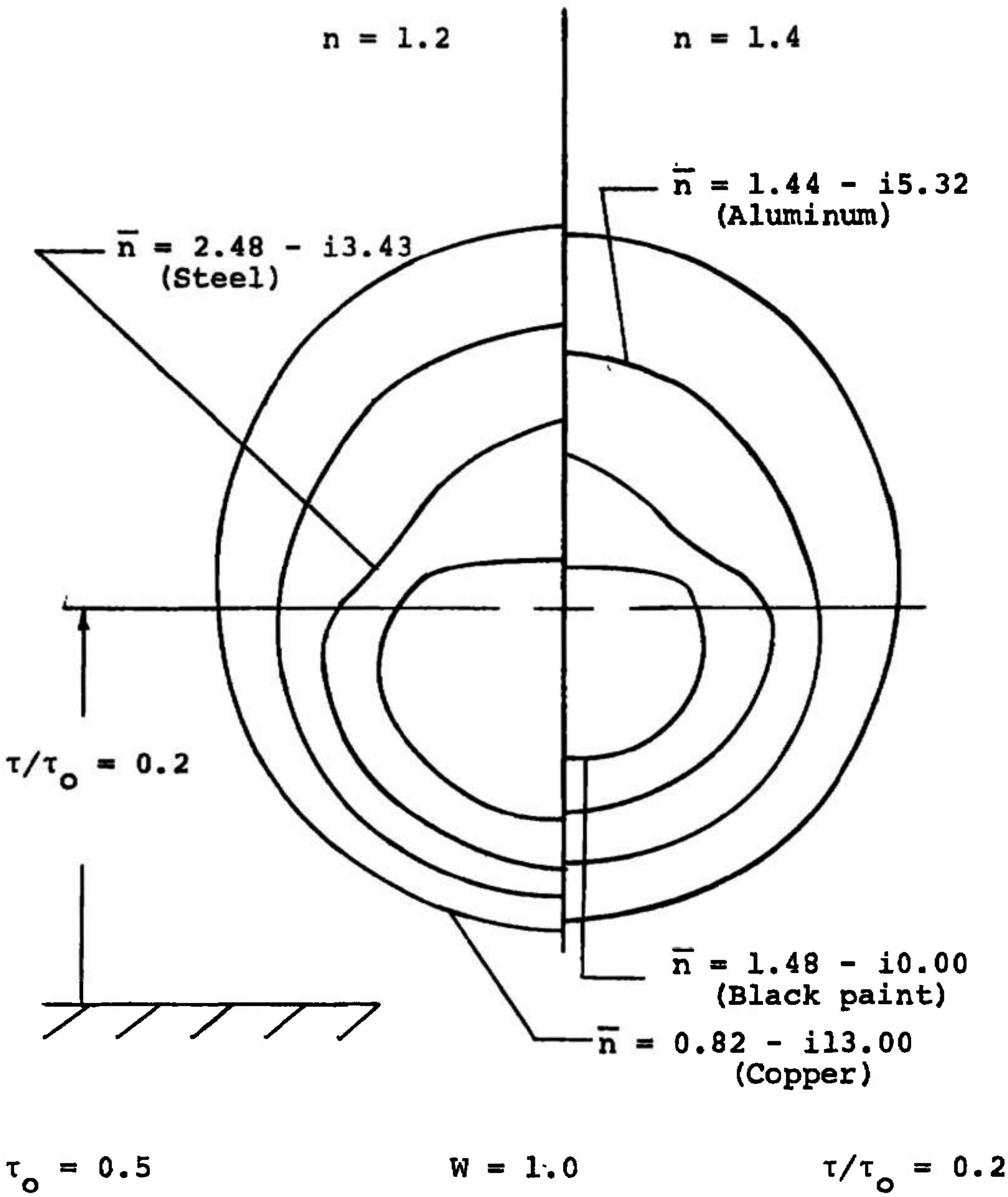

Figure 25. Refractive index effect on the angular distribution of the dimensionless intensity at a fixed point for a case 2 film.

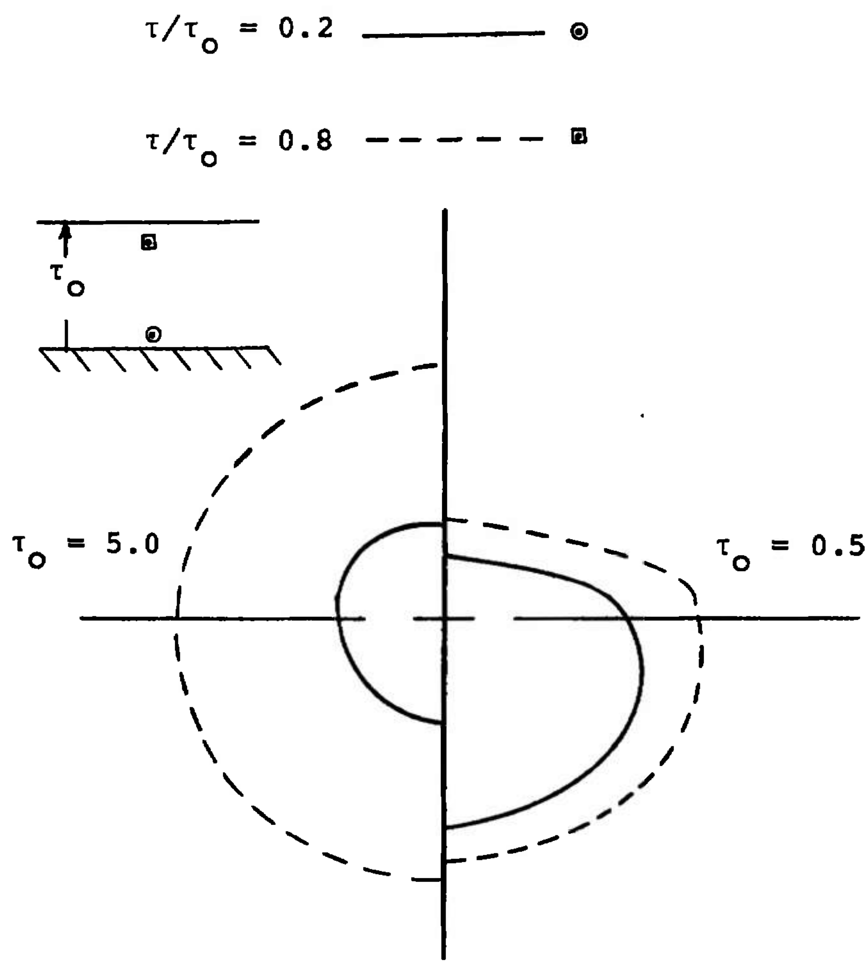

$\bar{n} = 1.48 - i0.00$ (Black paint)

$W = 1.0$ $n = 1.2$

Figure 26. Angular distribution of the dimensionless intensity at two points within two case 3 deposits on a black paint substrate.

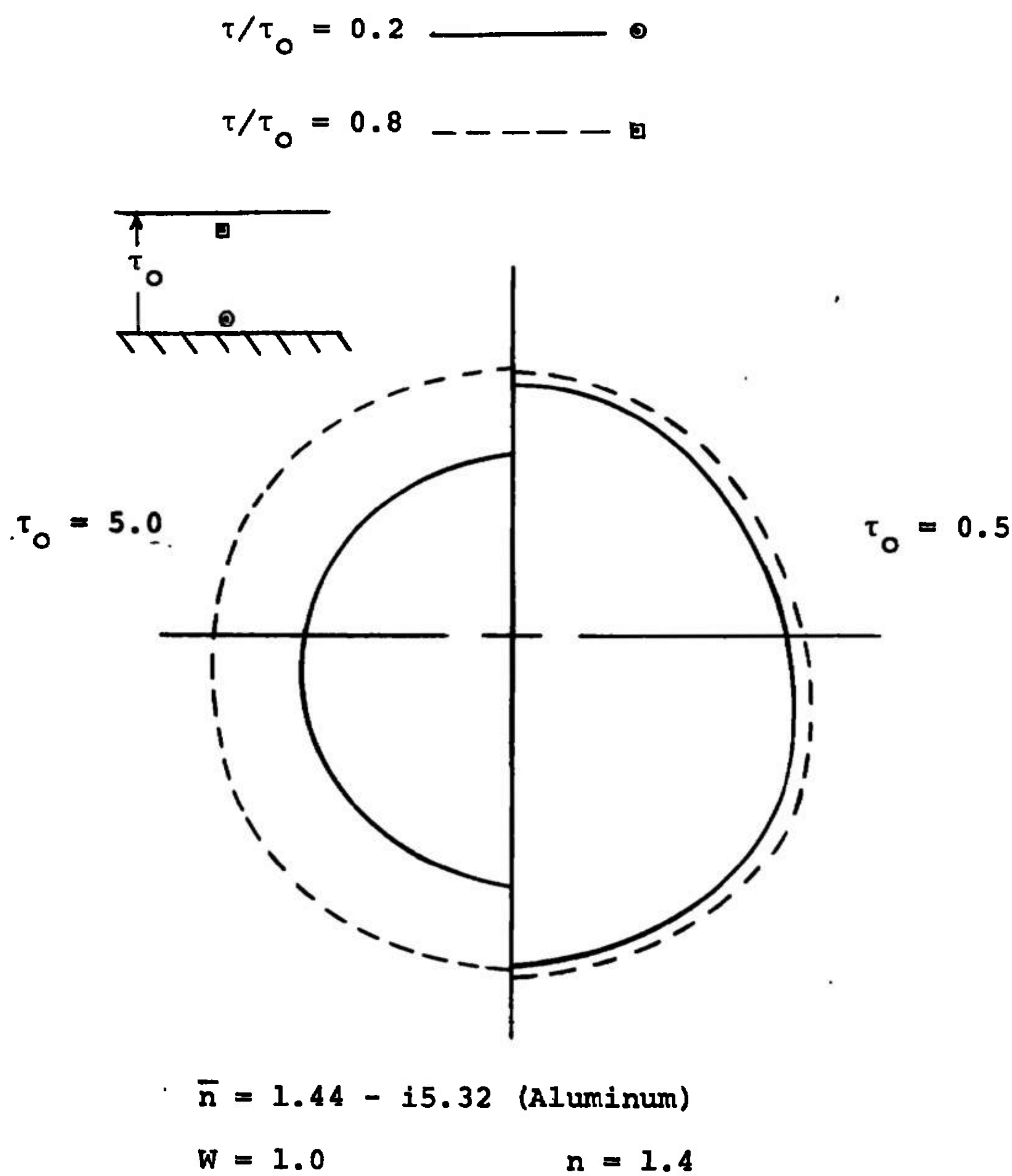

Figure 27. Angular distribution of the dimensionless intensity at two points within two case 3 deposits on an aluminum substrate.

the intensity near the substrate is much lower than near the top since scattering has caused substantial attenuation.

Shown in Figure 28 is the dimensionless intensity profiles for a case 3 deposit. A characteristic intensity profile is labeled A. The point C represents the normalized diffusely incident intensity. Upon crossing the top interface the transmitted intensity undergoes a discontinuous decrease, H. This is because now the intensity is diffusely transmitted into all directions and the main effect is a uniform decrease by an amount equal to all of the intensity which does not transmit through the top interface. Following direction $\overleftarrow{A}$, the intensity is attenuated due to scattering as it transmits toward the substrate, E. After almost complete absorption at E, the intensity is specularly reflected, F. As the intensity transverses upward from F, it is attenuated slightly due to scattering, but the intensity increases since it is strongly augmented as a result of scattering from other directions into the direction $\vec{A}$. After arriving at G, the intensity is partially internally reflected back to H and partially transmitted to point P, which represents the hemispherical-angular reflectance.

IV. CASE 4: DIFFUSE REFLECTOR AND TRANSMITTER ON A DIFFUSE SUBSTRATE

Case 4 is similar to case 3 except that the substrate is taken to be diffuse. The boundary conditions are given by Equations 38 and 18. Expressing Equation 18 in terms of

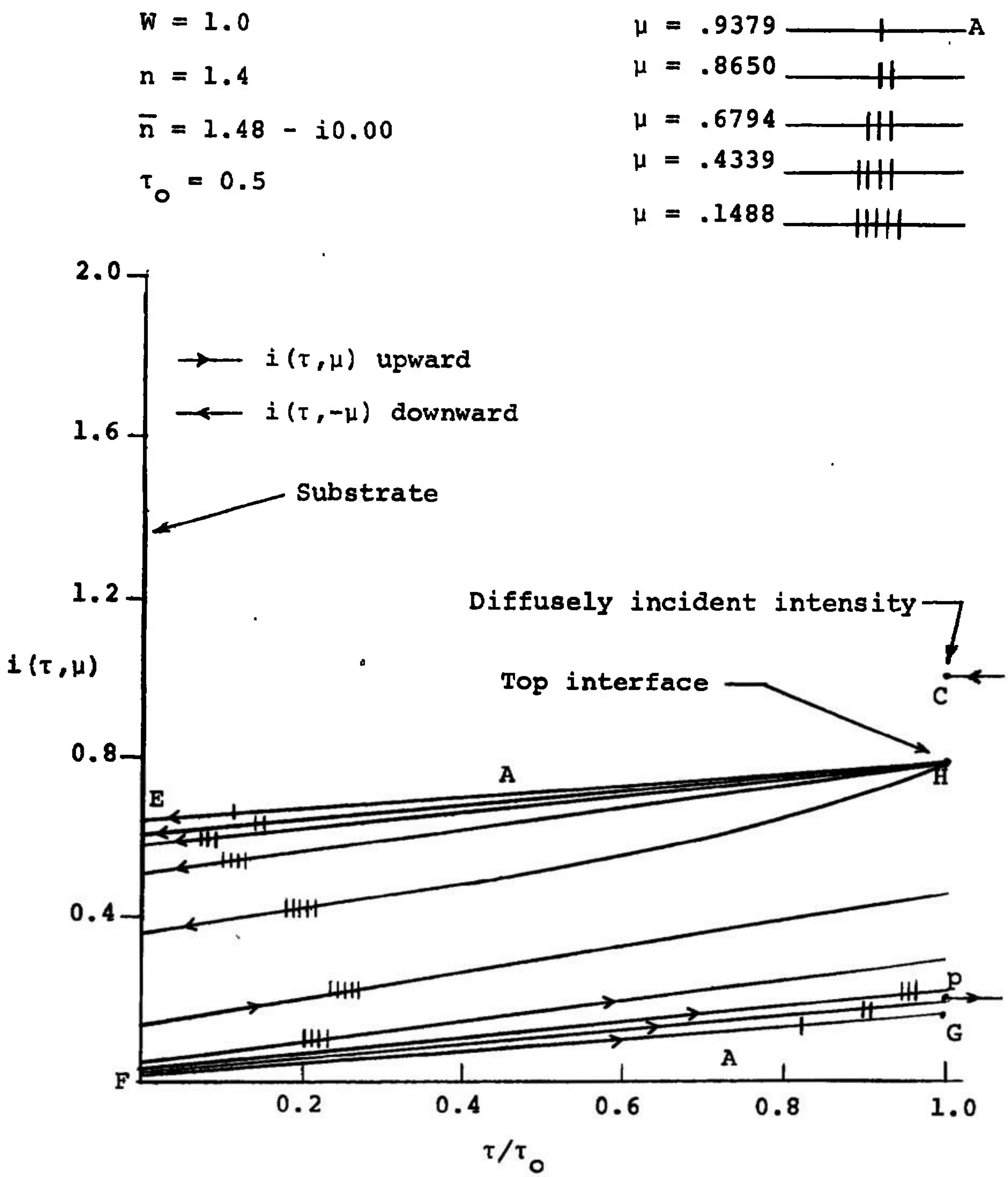

Figure 28. Dimensionless intensity profiles within a deposit along fixed directions for a case 3 film.

the quadrature

$$i(0,\mu_\ell) = \sum_{j=1}^{p} \rho_{23}(z_j)\, i(0,-z_j)\, z_j a_j \tag{41}$$

$\ell = 1, \ldots, p/2$ where z_j is a given in Equation 38 and $i(0,-z_j)$ is the magnitude of the downward intensity. The expression for ρ_{ha} is Equation 40. All of the results for case 4 almost exactly coincided with the results of case 3 except for very small optical thicknesses. Even for the small optical thicknesses the ρ_{ha} difference between the two cases was only minor. The reason for this difference, described in Figure 29, is because the initial reflectance decrease is not quite as low for the specular substrates as for the diffuse substrates. It would appear that the diffuse top interface almost completely dominates over any type of substrate effect as opposed to cases 1 and 2. Since the results of cases 3 and 4 are almost identical, only Figure 29 is provided in order to show the only difference of any interest.

V. CASE 5: DIFFUSE-REFLECTOR AND SPECULAR-TRANSMITTER ON A SPECULAR SUBSTRATE

The boundary conditions associated with cases 5 and 6 are approximations based on the rough glass reflection and transmission measurements presented in Reference [5]. The boundary conditions for case 5 are given by Equations 19 and 20. Expressed in terms of the quadrature integration

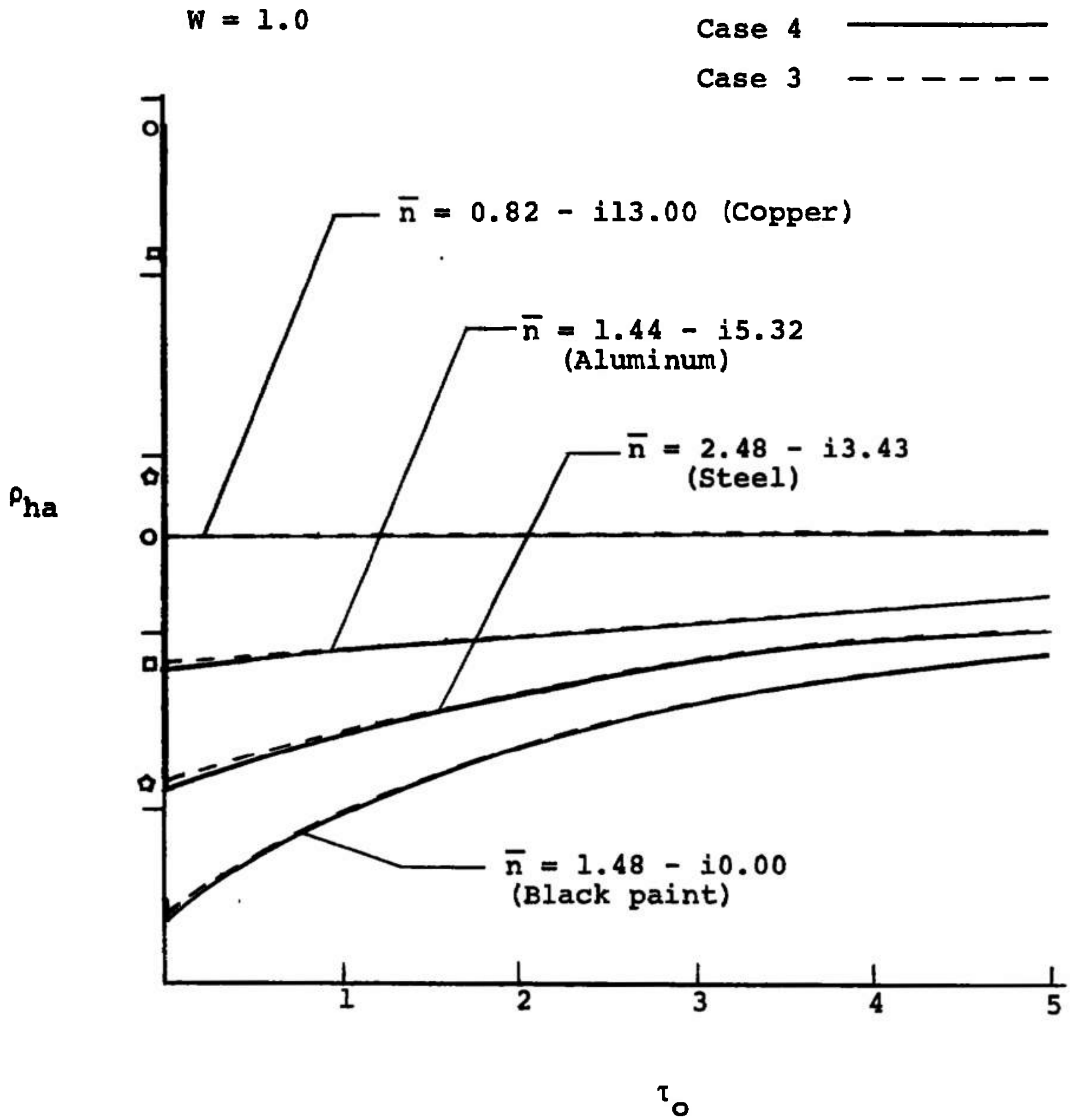

Figure 29. Comparison of case 3 and case 4 deposits for the dependence of ρ_{ha} as a function of optical thickness.

formula, Equation 19 becomes

$$i(\tau_o,-\mu_\ell) = [1 - \rho_{12}(\mu_{1_\ell})]n^2 + \sum_{j=1}^{p} \rho_{21}(z_j)\ i(\tau_o,z_j)z_j a_j \quad (42)$$

and similarly $\rho_{ha}(\mu_1)$ becomes

$$\rho_{ha}(\mu_{1_\ell}) = \sum_{j=1}^{p} \rho_{12}(z_j)z_j a_j + \frac{[1 - \rho_{21}(\mu_\ell)]}{n^2}\ i(\tau_o,\mu_\ell) \quad (43)$$

where $\ell = 1, \ldots, p/2$ and again where z_j are given as in Equation 38 and also where μ_{1_ℓ} and μ_ℓ are related by Snell's law in Equation 35.

Figure 30 demonstrates the variation of ρ_{ha} with optical thickness, τ_o, as a function of the albedo parameter. The two highest reflecting substrates show a slight initial increase after the monolayer deposit is formed. This type of phenomena at first sight seems strange, but Figure 31, taken from [2], shows that an initial increase may be realistic for highly reflecting substrates. The cause for this initial increase proved to be only an angular effect as indicated by Figure 32. Presented in Figure 33 is a quantitative argument of why there is an initial increase in the reflectance of case 5 for the near normal directions at $\tau_o = 0$. For case 1 the intensity is reflected from and

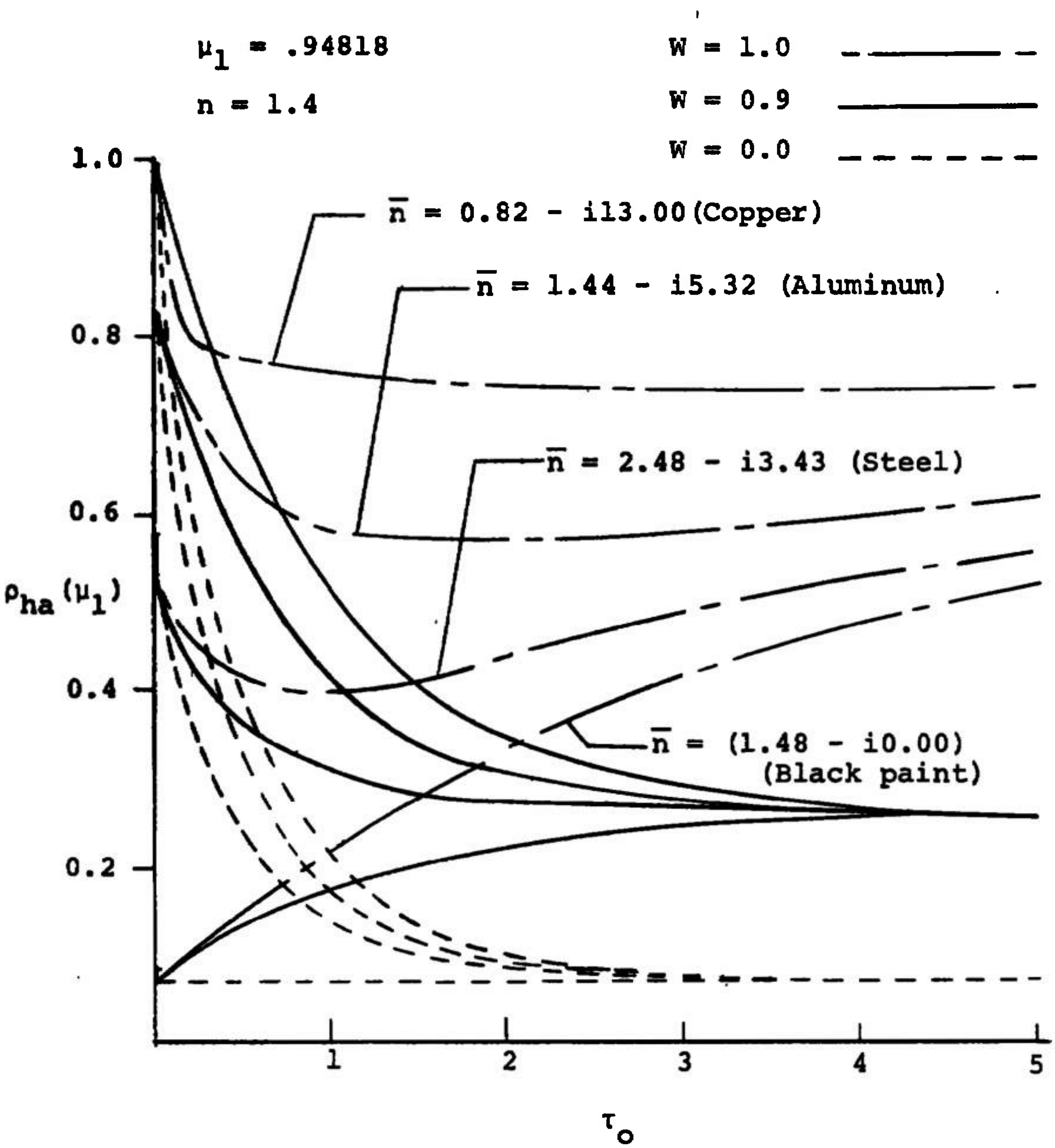

Figure 30. Dependence of $\rho_{ha}(\mu_1)$ on optical thickness as a function of albedo, W, for a case 5 deposit.

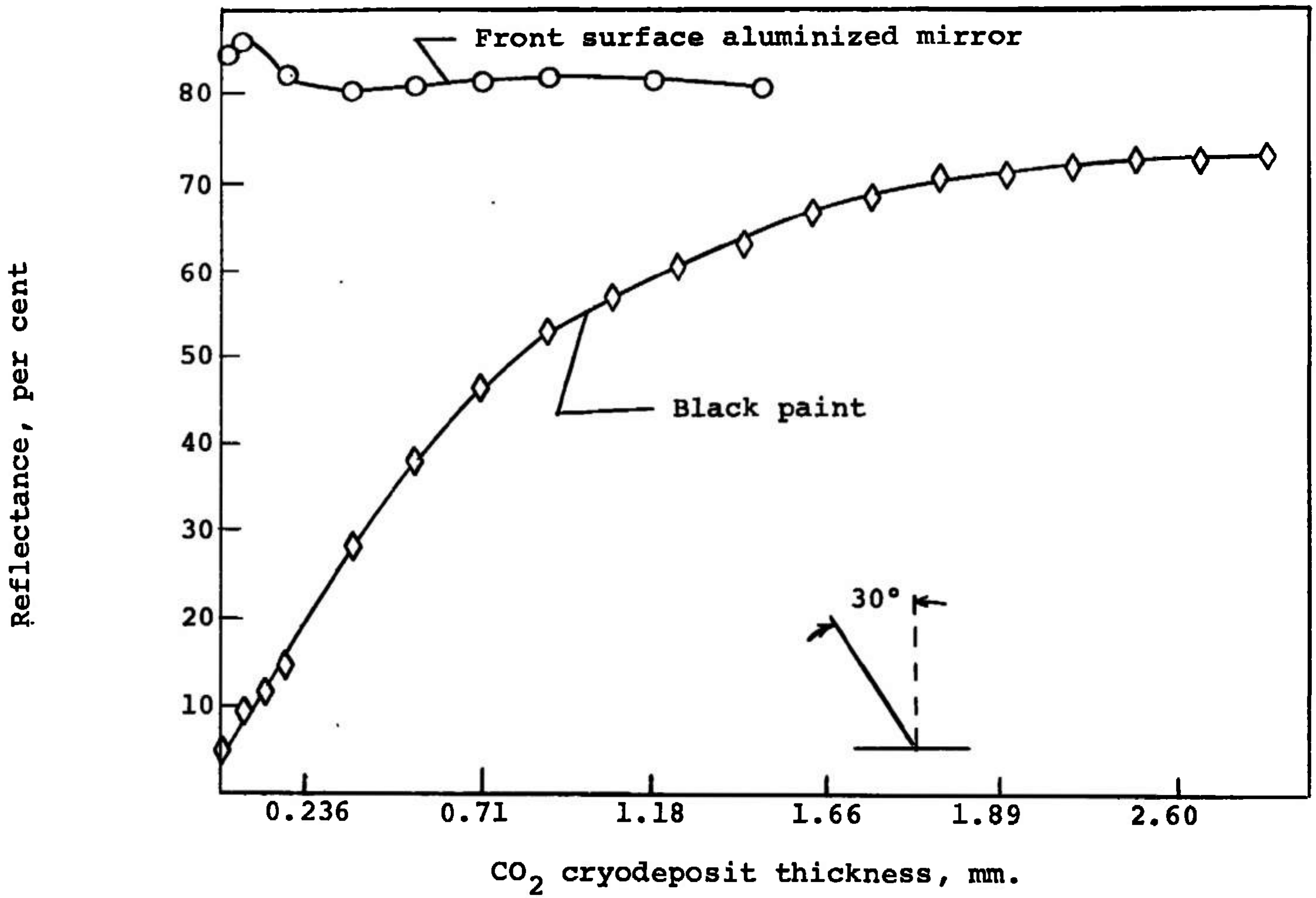

Figure 31. Substrate effects on the total reflectance of CO_2 cryodeposit.

Source: McCullough, B. A., B. E. Wood, and J. P. Dawson. "Thermal Radiative Properties of Carbon Dioxide Cryodeposits from 0.5 to 1.1 Microns," Arnold Engineering Development Center TR-65-94, Arnold Air Force Station, Tennessee, August, 1965.

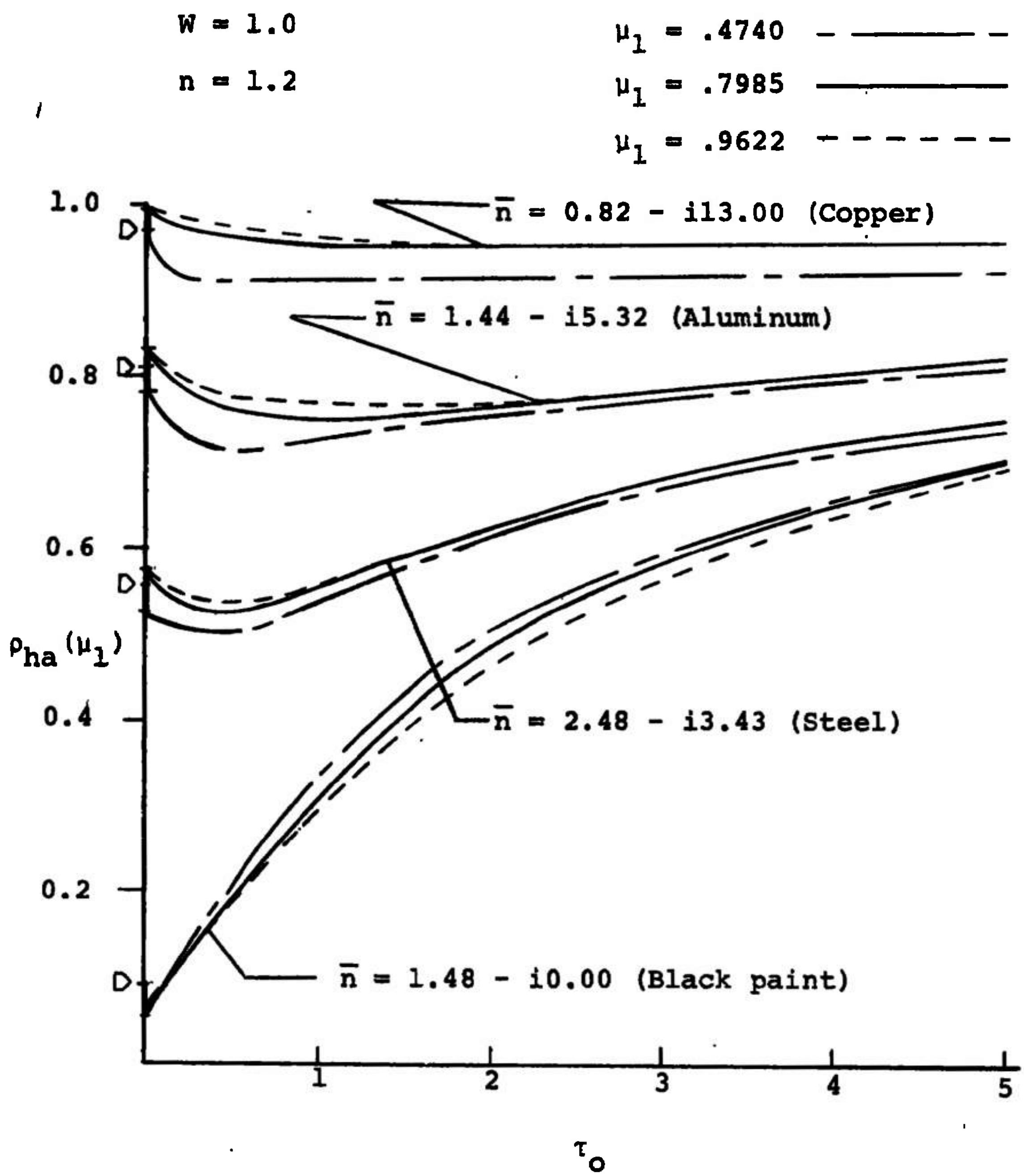

Figure 32. Viewing angle dependence of $\rho_{ha}(\mu_1)$ for a case 5 film for various substrates as a function of optical thickness.

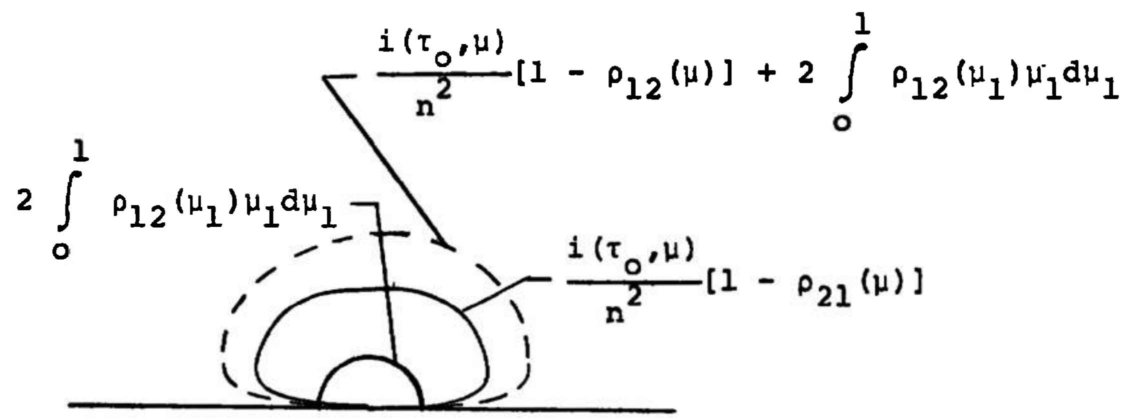

Case 5

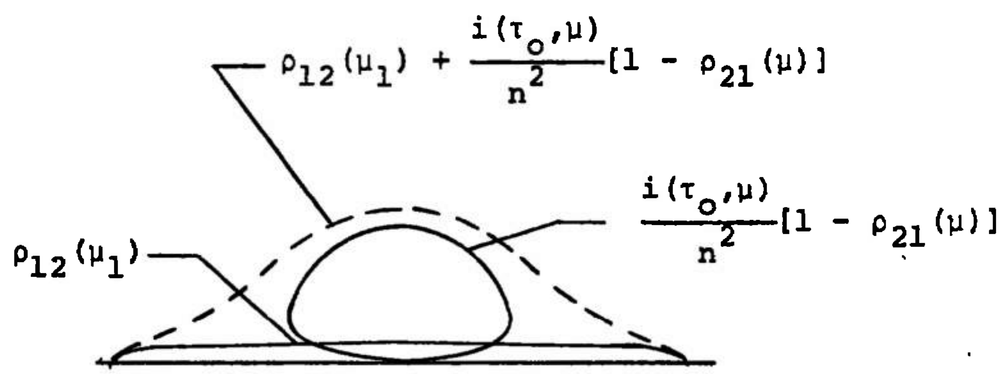

Case 1

Figure 33. Reason for the initial increase at $\tau_0 = 0$ for a case 5 film.

transmitted through the top interface specularly. This accounts for the increase in reflectance with increasing viewing angles. For case 5 the intensity is specularly transmitted and diffusely reflected. Effectively this causes an intensity increase in the near normal directions and a decrease in the intensity at the larger viewing angles. The net effect is a reflectance decrease with increasing angles of incidence. For the highly reflecting substrates the transmitted intensity is higher. Thus the intensity transmitted into the near normal directions for a highly reflecting substrate is an intensity increase large enough to dominate over the relative refractive index effect. The effect on the lower reflecting substrates is not an initial increase but rather a less drastic initial decrease than case 1 due to the relative refractive index change. The symbols on the ordinate of Figures 32 and 34 indicate the bare substrate reflectance. Similar to the other cases as shown in Figure 30, there is a limiting ρ_{ha} value as τ_o increases for the absorbing films ($W \neq 1.0$). These limiting values are greater than case 1 since the initial drop is lower. As indicated in Figure 32, this initial increase is only an angular effect due to focusing of the intensity into the nearer normal directions. As the viewing angle increases the initial reflectance tends to decrease since the energy at the high viewing angles has been channeled into nearer normal viewing angles due to the diffuse reflection. Also evident is that ρ_{ha} for case 5 is not a monotonically

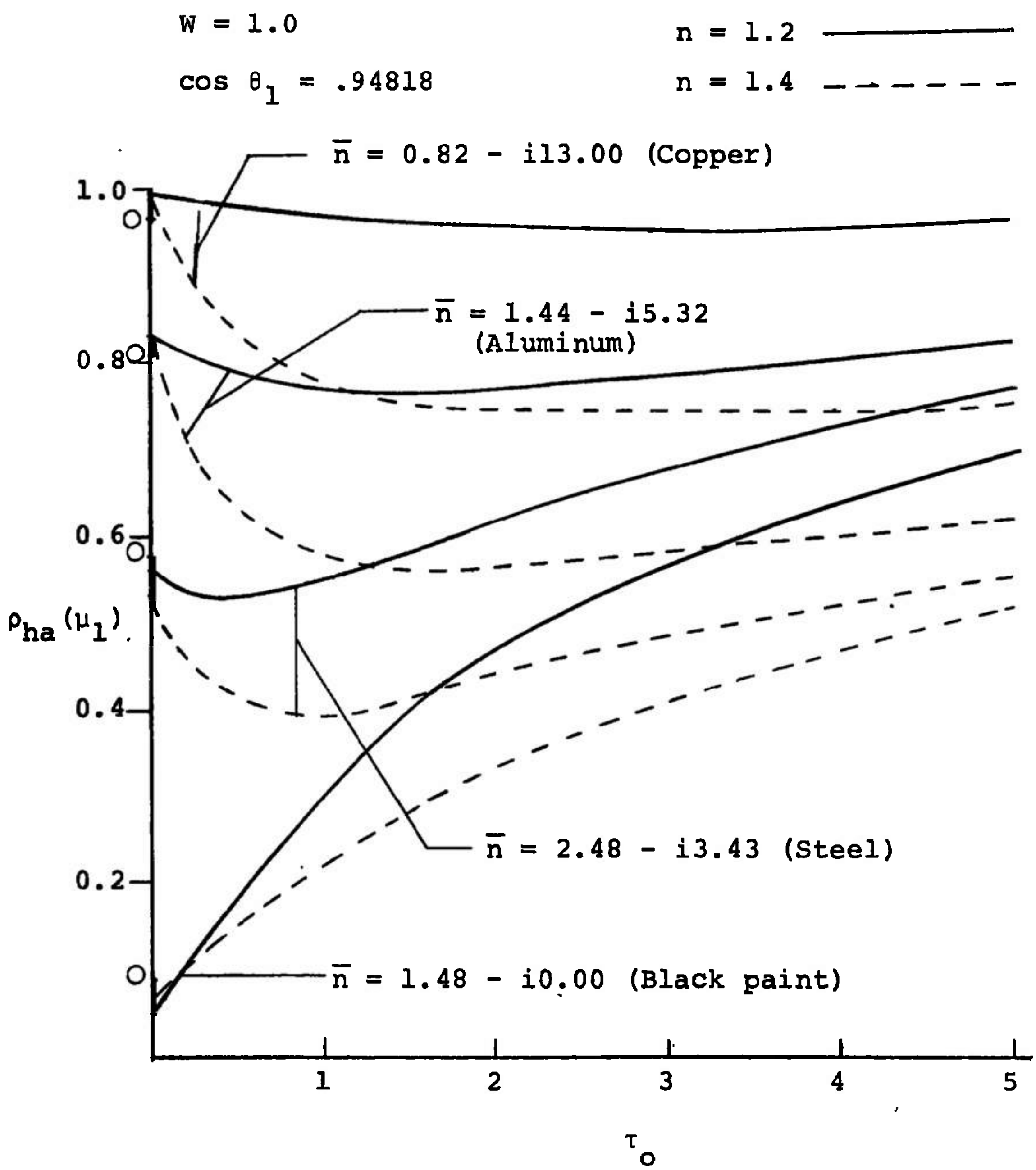

Figure 34. Effect of refractive index on $\rho_{ha}(\mu_1)$ for a case 5 film.

increasing function of viewing angle.

Illustrated in Figure 34 is that ρ_{ha} is a much stronger function of refractive index than case 1. For case 1, at $\tau_o = 0$, there were some directions ($\theta > \theta_c$) which were void of radiant intensity. In case 5, at $\tau_o = 0$, since the top interface is diffuse for energy incident from within, there are no regions void of radiant energy. However, the directions past θ_c should be lean in radiant energy since the substrate is specular. In case 1 as the optical thickness begins to increase, scattering commences to occur. Energy is scattered past the critical angle where total internal reflection and hence trapping occur. Intensity scattered past θ_c corresponds to long path lengths into which the scattered energy is total internally reflected. Since the path lengths are long the intensity in these directions undergo substantial rescattering before being reincident on the absorbing substrate.

For case 5, by the definition of diffuse reflection given by Equation 12, as τ_o increases to where scattering becomes important, energy is scattered past the critical angle. However besides being trapped, energy is diffusely distributed; therefore much of the scattered intensity is directed into short path lengths where rescattering is less probable and more interaction with the absorbing substrate is highly probable. Therefore case 5 has more substrate interaction than case 1. This substrate interaction is a strong function of the relative refractive index change.

For $n = 1.2$ there is not much difference (except for $\tau_o = 0$) between cases 1 and 5. For $n = 1.4$ the interaction with the substrate is stronger thus causing a larger ρ_{ha} decrease as scattering becomes effective. Also due to the short path lengths of the reflected, scattered intensity caused by the diffuse reflectance, the τ_o at which ρ_{ha} begins to increase again is larger for case 5 than for case 1. The scattering will not dominate until the deposit thickness τ_o becomes thick enough to constitute large path lengths. As τ_o increases to large values the scattering dominates and less intensity is able to penetrate to the substrate where absorption occurs, thus ρ_{ha} increases again.

The angular intensity profiles of Figure 35 demonstrate the characteristic critical angle effects. Comparing Figure 35 with Figure 12, page 56, reveals that for $n = 1.2$ the intensity directed into angles greater than θ_c is about the same for both cases 1 and 5; for $n = 1.4$ case 5 directs less intensity into angles greater than θ_c and channels more toward the absorbing substrate. Thus less energy past the critical angle is available for rescattering as τ_o increases, and hence the reflectance for $n = 1.4$ is less in case 5 than for case 1. The main factor for this is the diffuse reflectance increase of case 5 is more significant than the specular reflectance increase of case 1 in varying n from 1.2 to 1.4.

Figures 36 and 37 demonstrate the effects of a high degree of scattering associated with large optical

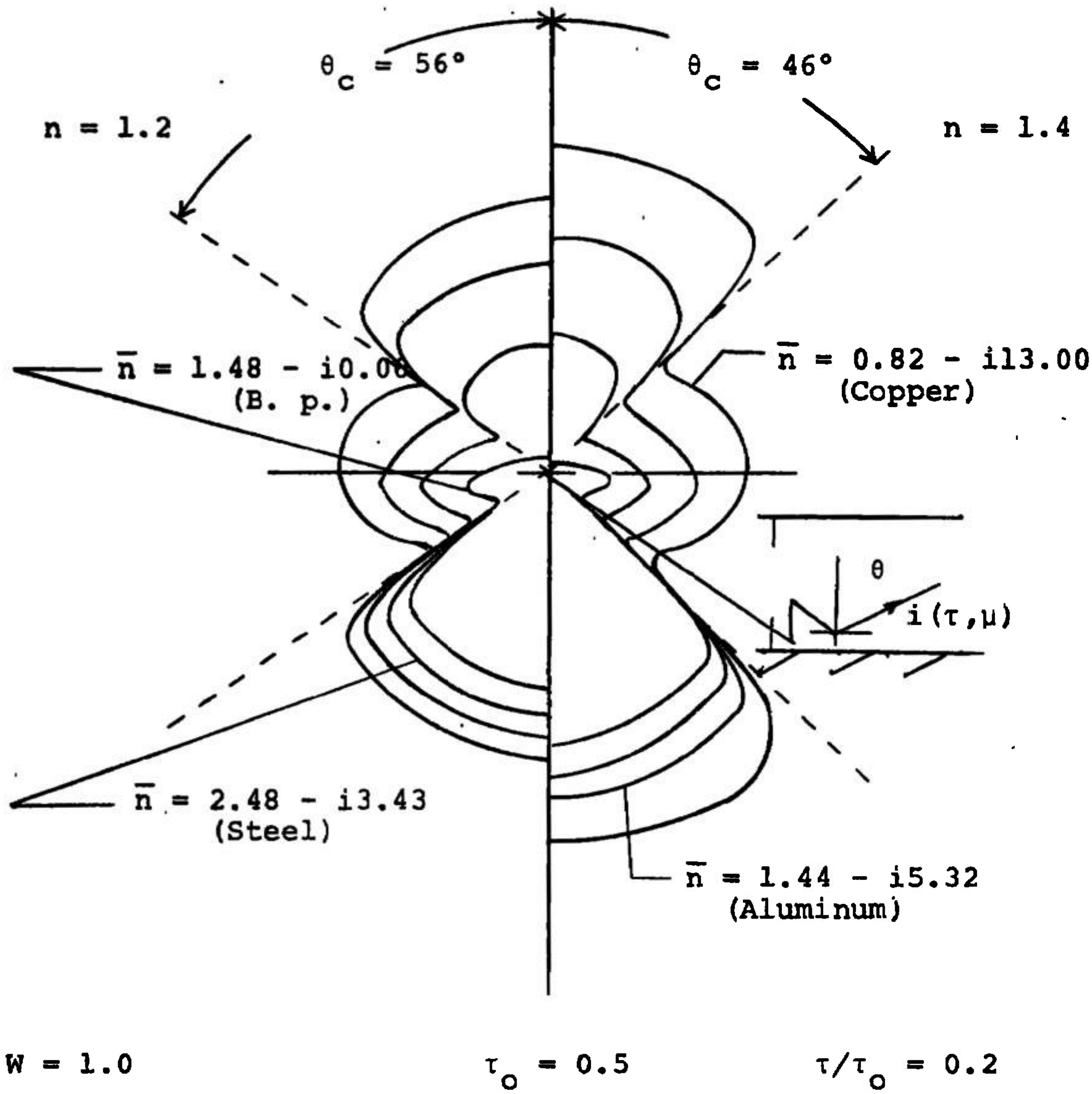

Figure 35. Refractive index effect on the angular distribution of the dimensionless intensity for a case 5 film.

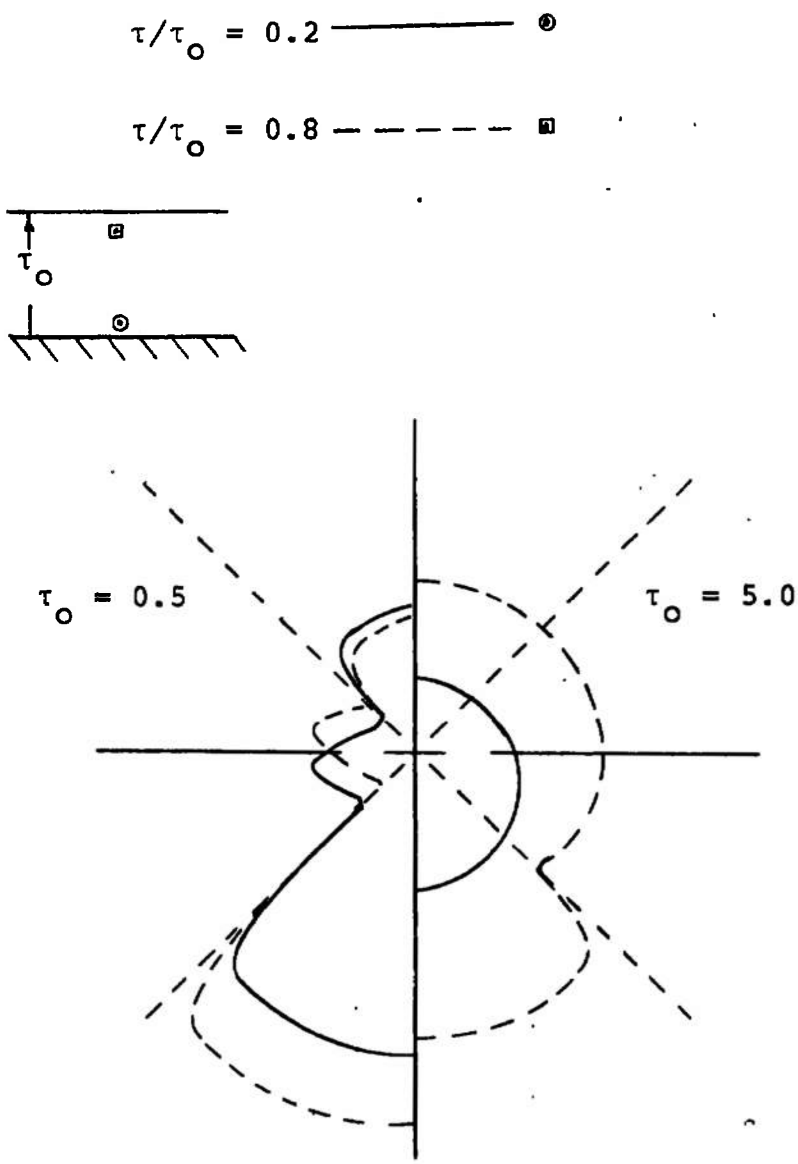

$W = 1.0$ $\quad n = 1.4$ $\quad \bar{n} = 2.48 - i3.43$

Figure 36. Angular distribution of the dimensionless intensity at two points within two case 5 deposits on a steel substrate.

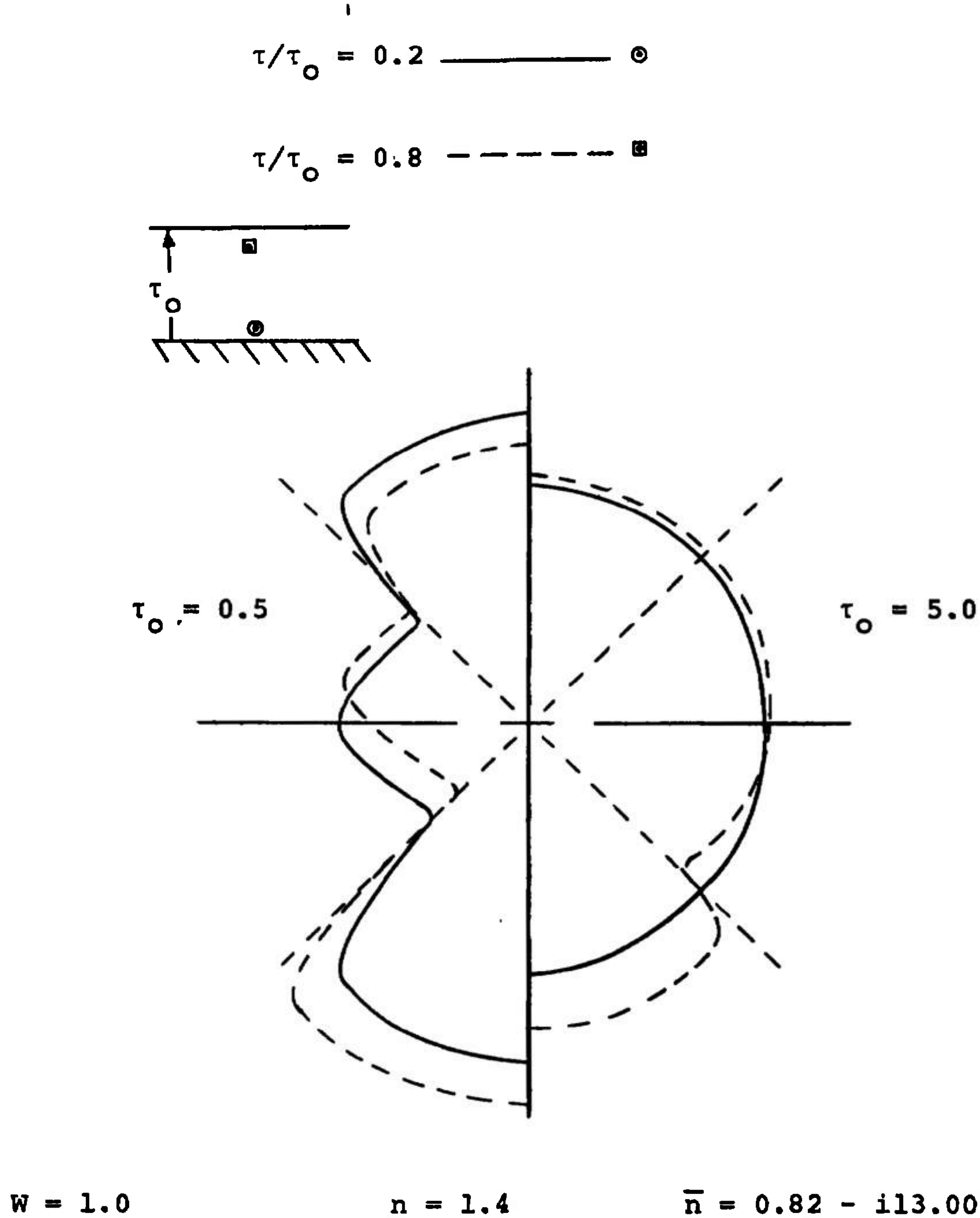

Figure 37. Angular distribution of the dimensionless intensity at two points within two case 2 deposits on a copper substrate.

thicknesses. For $\tau_o = 5.0$ and $\tau/\tau_o = .8$, the downward intensity is influenced by the critical angle associated with the top interface. The upward intensity at $\tau/\tau_o = .8$ is very distant from the influence of the bottom interface, and hence scattering has smoothened the upward intensity profiles. For $\tau/\tau_o = .2$ and $\tau_o = 5.0$, the internal scattering completely dominates the distribution shape in all directions. At the smaller optical thicknesses the film is so thin that the influence of the boundary conditions has a strong effect at all positions within the deposit.

Presented in Figure 38 are the dimensionless intensity profiles for a case 5 deposit. Two characteristic profiles are labeled (A and B). The point C represents the normalized diffusely incident intensity. After crossing the top interface, the transmitted intensity discontinuously increases due to the solid angle change and the internal diffuse reflection. Following $\overleftarrow{A}$, the intensity is attenuated due to scattering as it approaches the substrate, E. Arriving at E, the intensity is specularly reflected to point F. Following $\vec{A}$ from point F, the intensity is slightly attenuated as it approaches the top interface. It appears that the intensity scattered from and into $\vec{A}$ must be nearly equal. After arriving at G, part of $\vec{A}$ is diffusely internally reflected and the other portion is specularly transmitted to point P, which represents $\rho_{ha}(\mu_1)$.

Curve B represents another characteristic direction. Starting at J the intensity in this direction is composed of

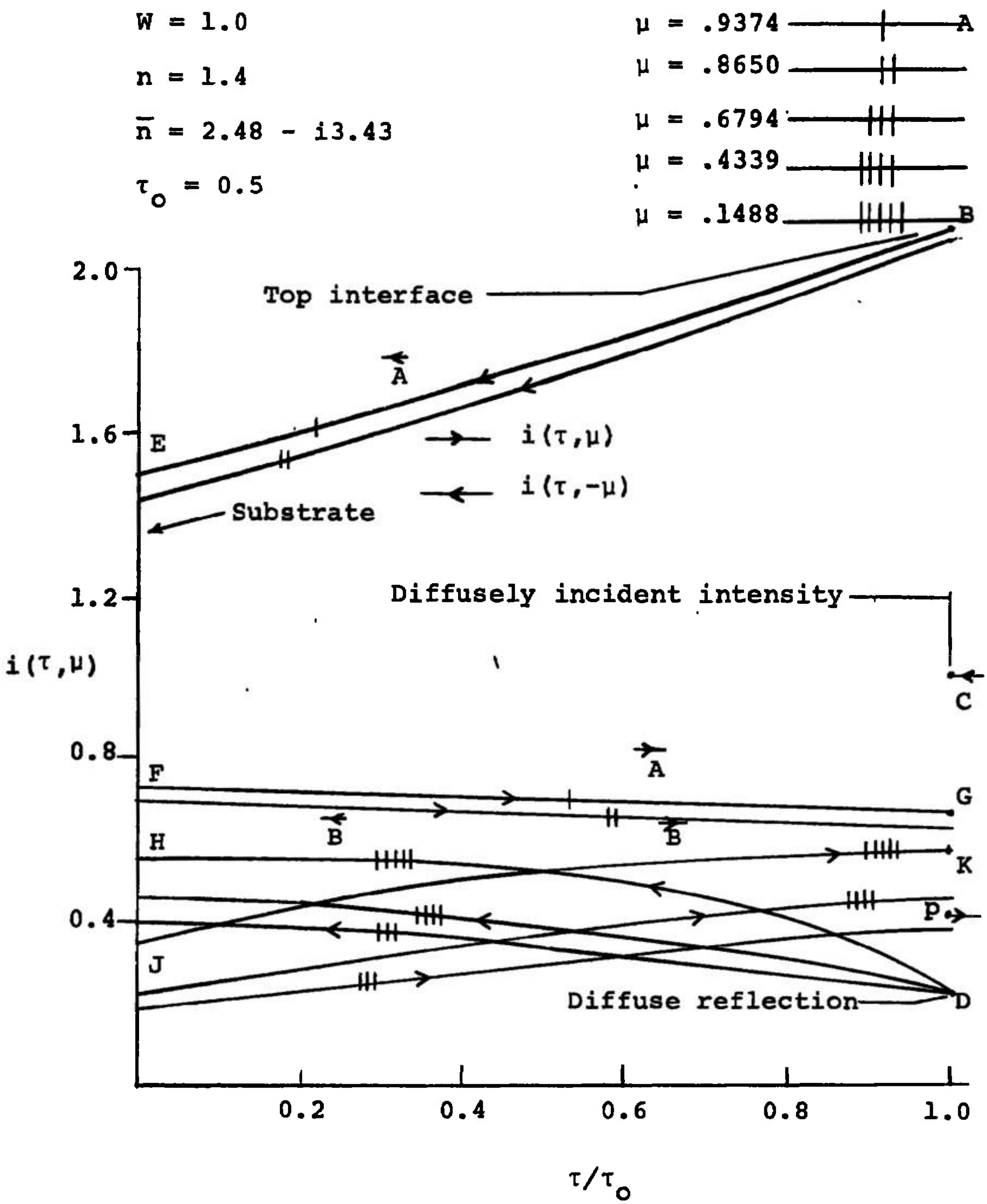

Figure 38. Dimensionless spatial intensity distributions within a deposit along fixed directions for a case 5 film.

scattered energy and energy associated with the diffuse reflection from the top interface. The intensity $\vec{B}$ is augmented due to scattering until it reaches K where it is totally and diffusely internally reflected to point D. As $\overleftarrow{B}$ propagates toward the substrate it is augmented again due to scattering. Upon reaching the substrate at H, it is specularly reflected to J. The curve with two slashes is similar to A. The other curves have the same interpretation as B.

VI. CASE 6: DIFFUSE-REFLECTOR AND SPECULAR-TRANSMITTER ON A DIFFUSE SUBSTRATE

The difference between cases 5 and 6 is that case 6 has a diffuse substrate. The boundary conditions are represented by Equations 21 and 22. Expressed in terms of the quadrature integration formula these boundary conditions become Equations 40 and 41. The expression for ρ_{ha} is the same as Equation 43.

The effect of the diffuse substrate, shown in Figure 39, is similar to that observed for cases 1 and 2. The symbols placed along the ordinate of Figures 39 and 40 are used to indicate the difference between the bare substrate reflectance and the reflectance decrease due to the relative refractive index change. The initial decrease is noticeably deeper because more intensity is reflected into directions past the critical angle. Also as τ_o increases there is no second decrease. Since the substrate is diffuse there are no directions inside the deposit which are void or lean of

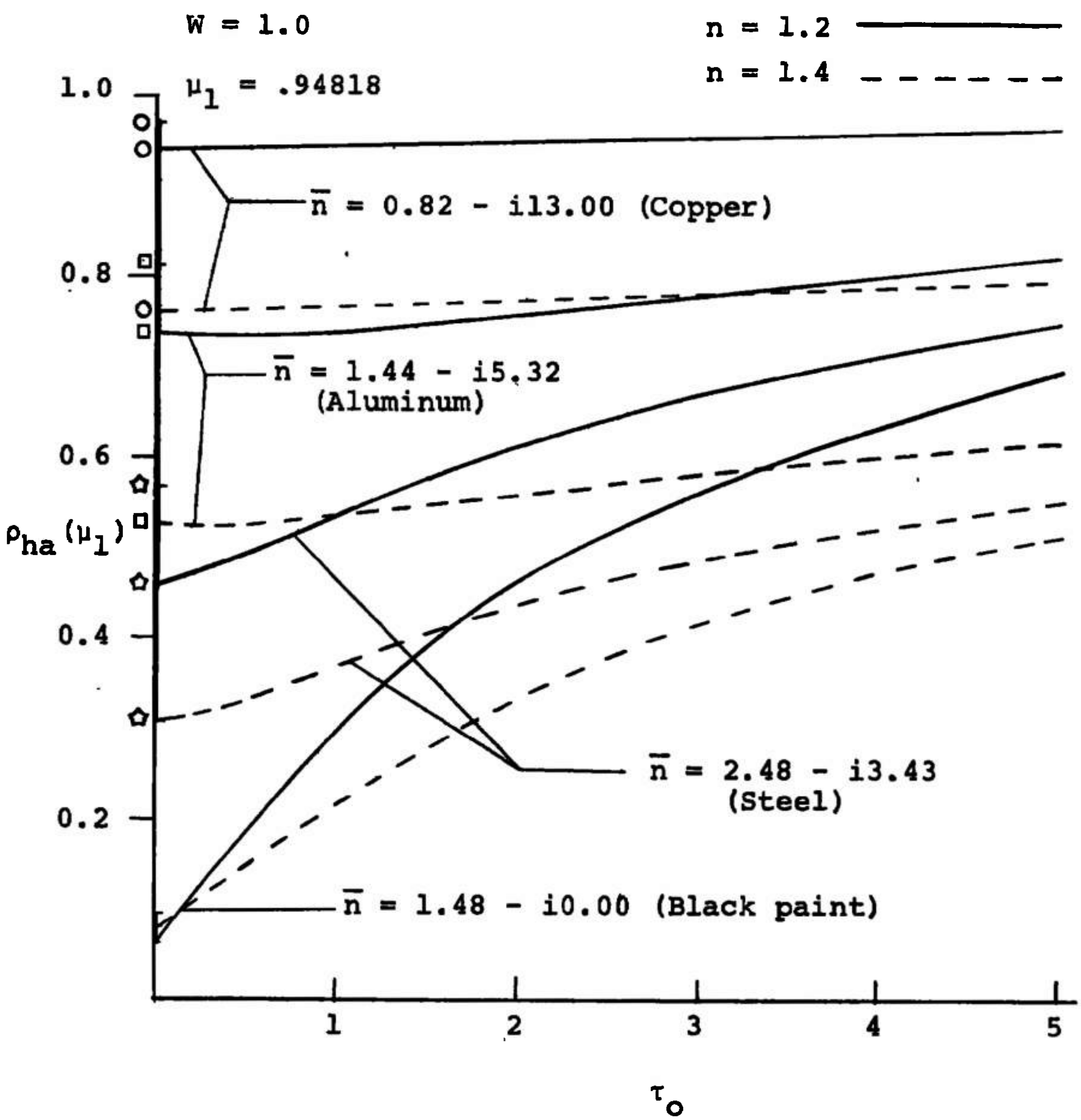

Figure 39. Effect of refractive index on $\rho_{ha}(\mu_1)$ for a case 6 film.

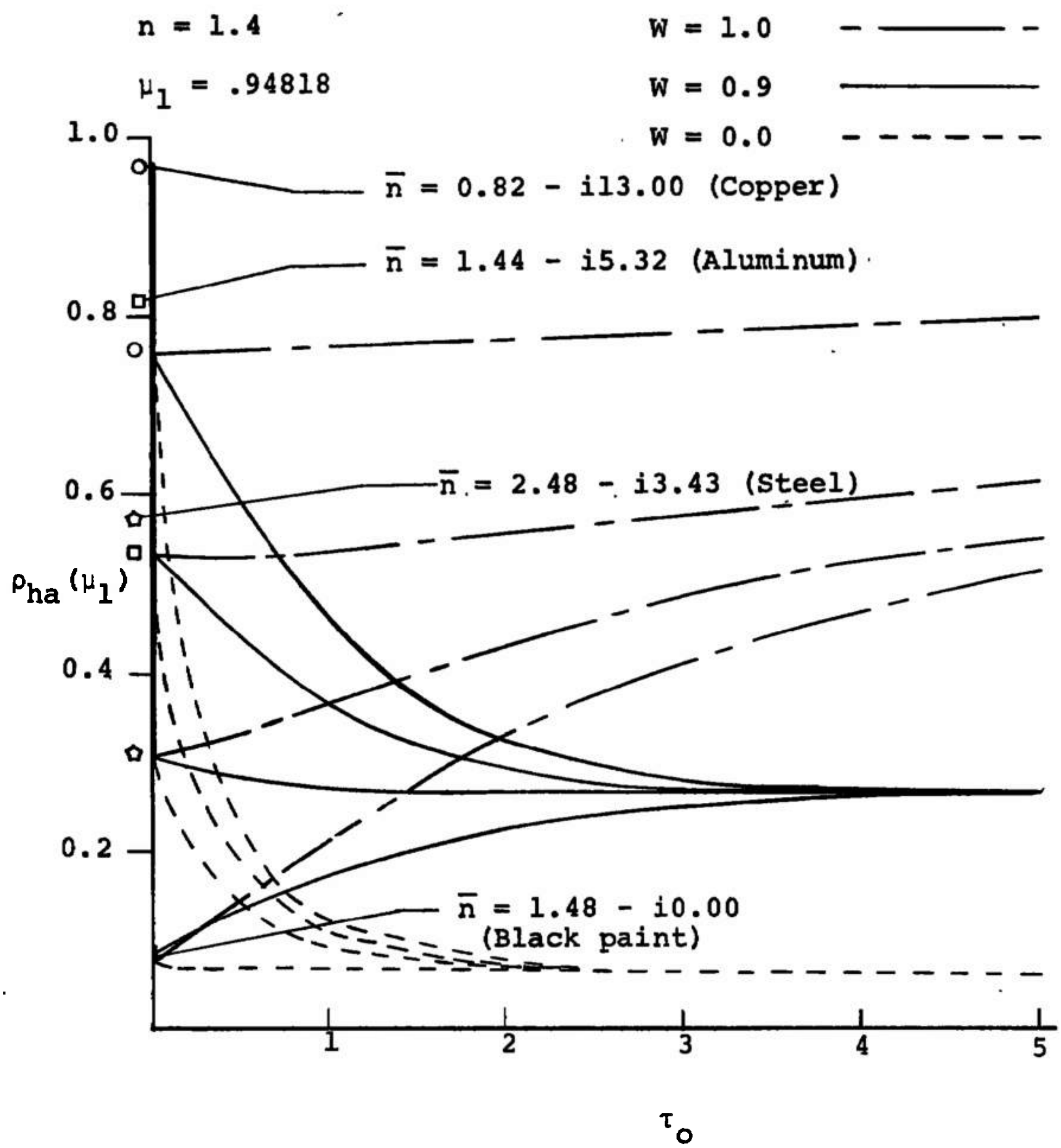

Figure 40. Dependence of $\rho_{ha}(\mu_1)$ on optical thickness as a function of albedo, W, for a case 6 deposit.

radiant energy. The net effect is that scattering causes ρ_{ha} to increase monotonically as τ_o increases for all substrates. Also evident is the stronger dependence on refractive index change as opposed to case 2.

Illustrated in Figure 40 is the influence of the albedo parameter. The limiting values of ρ_{ha} are the same for cases 5 and 6. Thus the angular nature of the substrate is shown to have no effect on the reflectance of absorbing films at large optical thicknesses. Figure 41 indicates the same type of viewing angle variation as for case 5. The angular dependence shows that ρ_{ha} decreases as the viewing angle increases. This again is due to the focusing of radiant intensity into directions nearer the normal. The characteristic intensity profiles were very similar to that of case 5 except for the diffuse reflectance at the substrate and hence will not be shown here.

The influence of the boundary conditions are shown in Figure 42. The downward intensity shows the characteristic critical angle profile. The upward intensity profile is very smooth as dictated by the diffuse substrate. The diffuse substrate only uniformly distributes the intensity in the region $0 < \theta < 90°$. The range $180°-\theta_c < \theta < 180°$ is effected predominately by the critical angle transmission of the top interface. The intensity in the region $90° < \theta < 180°-\theta_c$ is mainly due to scattering. Since the optical thickness is small and hence scattering is not dominant yet, only a small amount of intensity has been scattered into

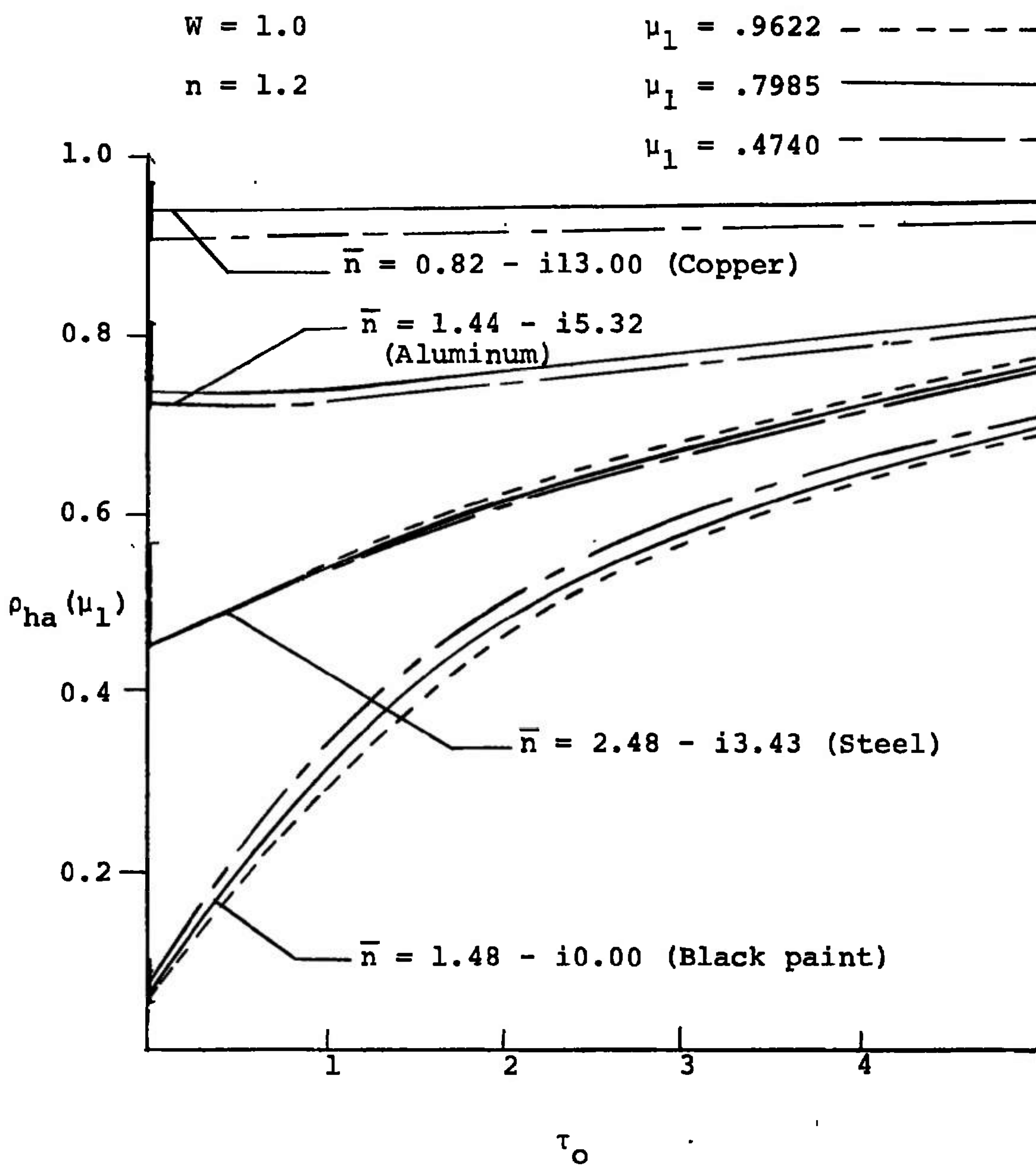

Figure 41. Viewing angle dependence of a case 6 film for various substrates as a function of optical thickness.

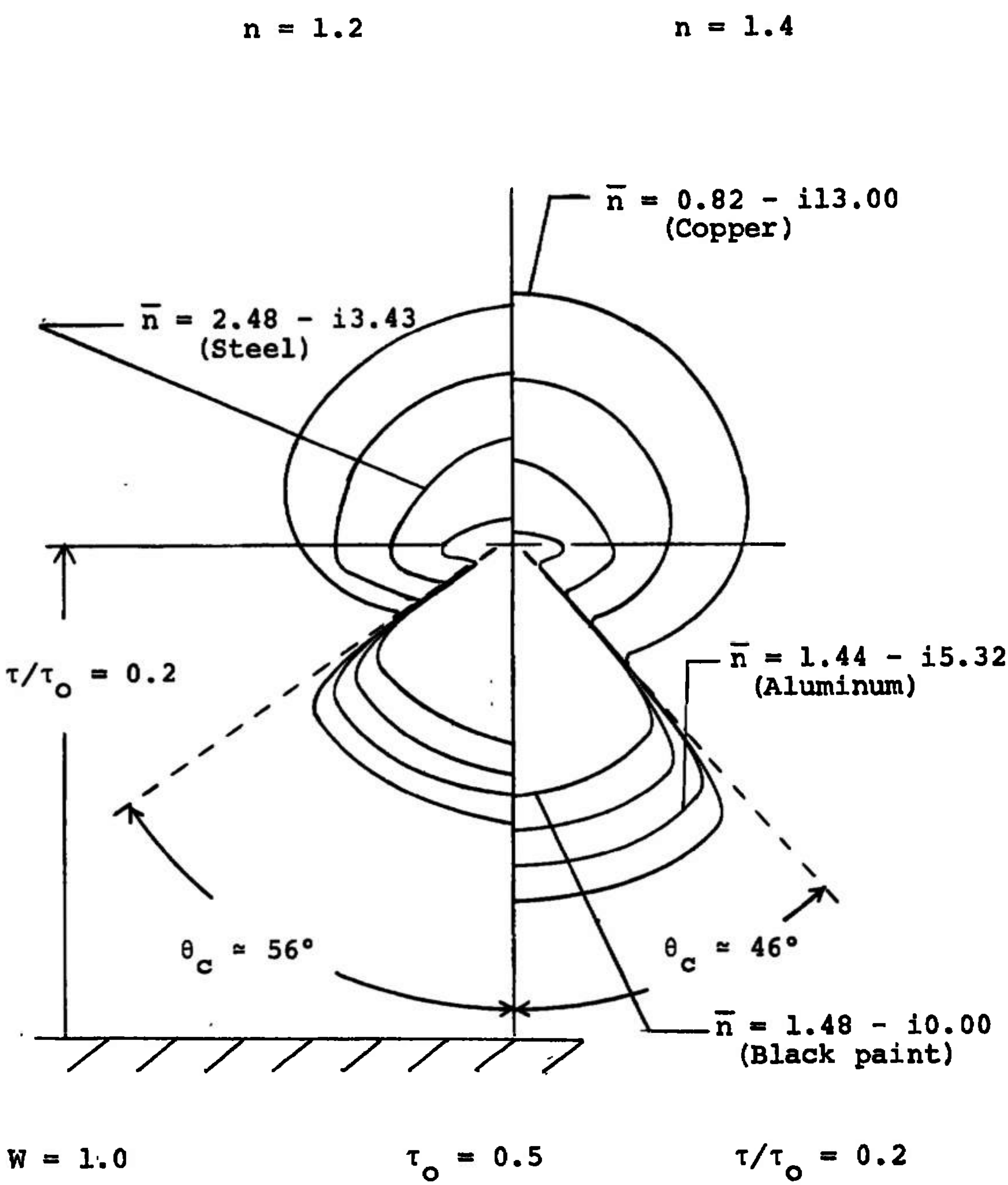

Figure 42. Refractive index effect on the angular distribution of the dimensionless intensity for a case 6 film.

this region. This is why there is a decrease in the intensity distribution between $90° < \theta < 180° - \theta_c$. Of course, since the profile must be continuous, the intensity profiles must match at $\theta = 90°$ and $\theta = 180° - \theta_c$. Also of interest from Figure 42 is how the change in refractive index from $n = 1.2$ to $n = 1.4$ causes a great increase in the amount of intensity channeled into shorter path lengths toward the substrate.

Figure 43 reveals the importance of optical thickness upon scattering. For $\tau_o = 0.5$ scattering has not yet become dominant and the intensity profiles have the critical angle influence throughout the deposit. At $\tau_o = 5.0$ the deposit is thick enough for scattering to dominate the profile distribution. The profiles are more uniform and smooth due to the strong scattering associated with the large optical thickness.

Figures 44 and 45 are provided as a means of comparing the main differences between cases 5 and 6. The angular nature of the substrate appears only to be of significance at small optical thicknesses The black paint substrate showed negligible ρ_{ha} differences for all $\tau_o > 0$. Only a slightly deeper initial drop was noticeable for the black paint substrate.

Similar to the comparison of cases 1 and 2, the primary value is that if a thick coating is to be sprayed or somehow deposited on a high or low reflecting substrate that not much care is necessary as to whether the substrate is

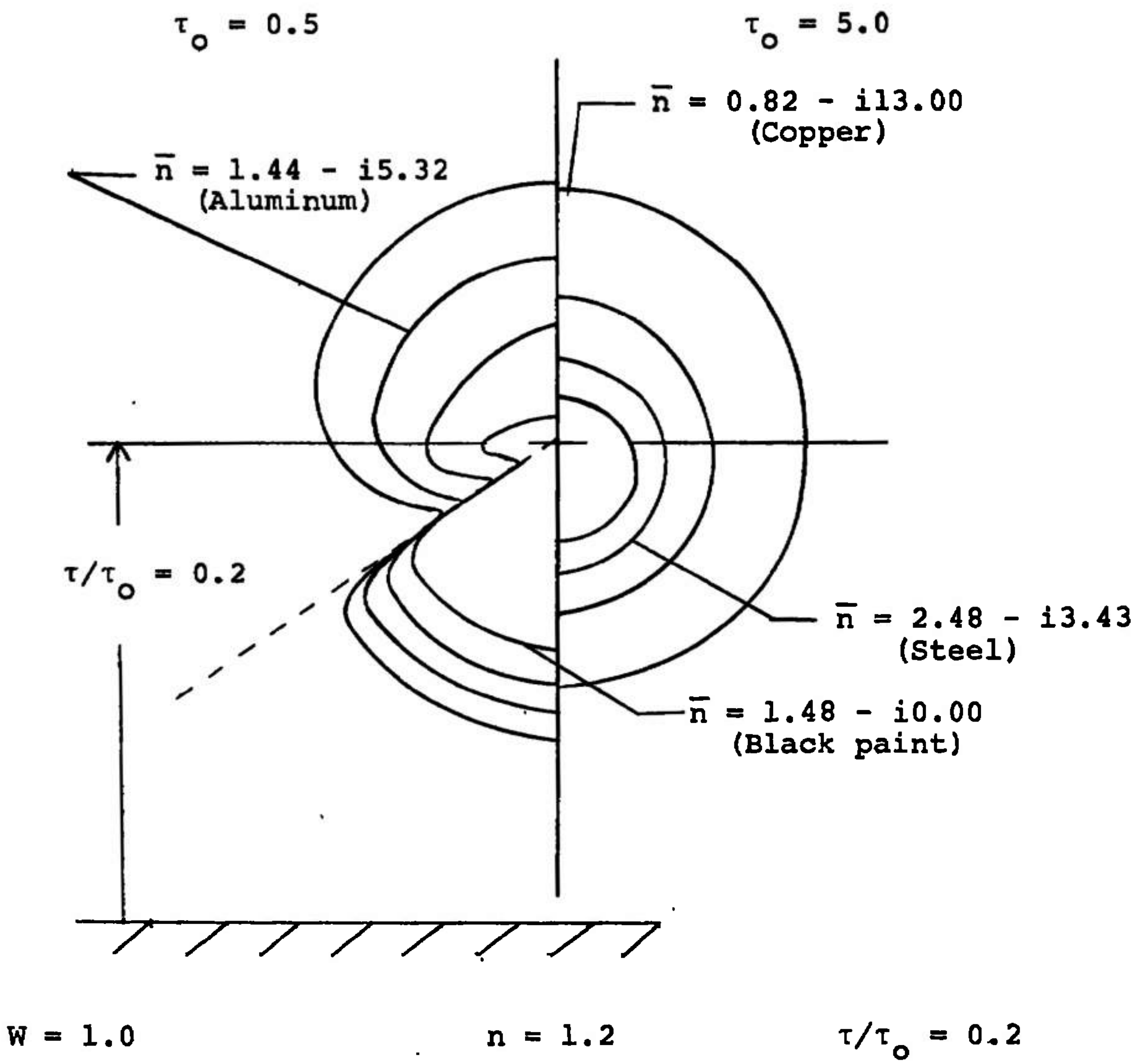

Figure 43. Angular dependence of the dimensionless intensity field, $i(\tau,\mu)$, at fixed points for two optical thicknesses for a case 6 deposit.

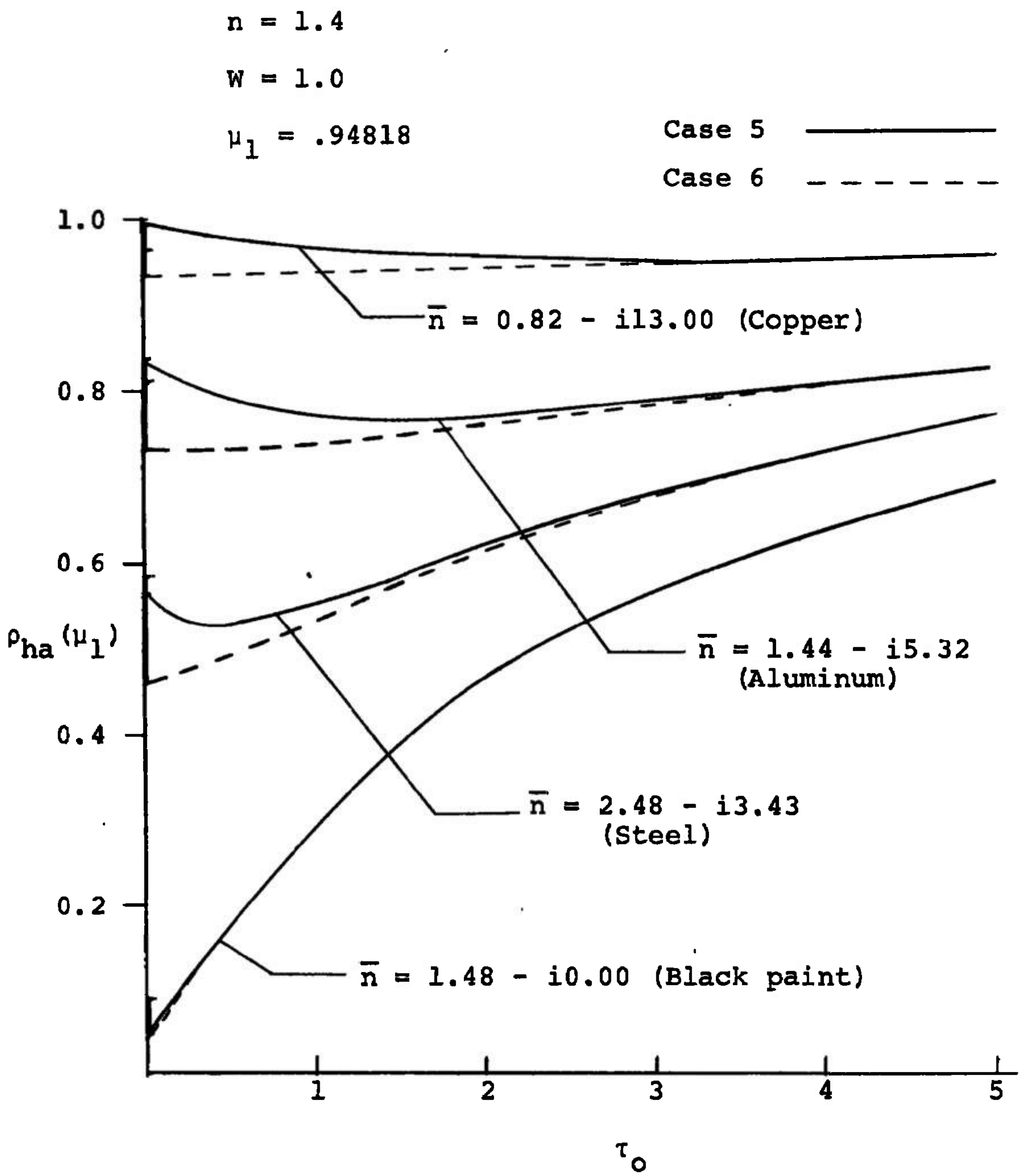

Figure 44. Comparison of case 5 and case 6.

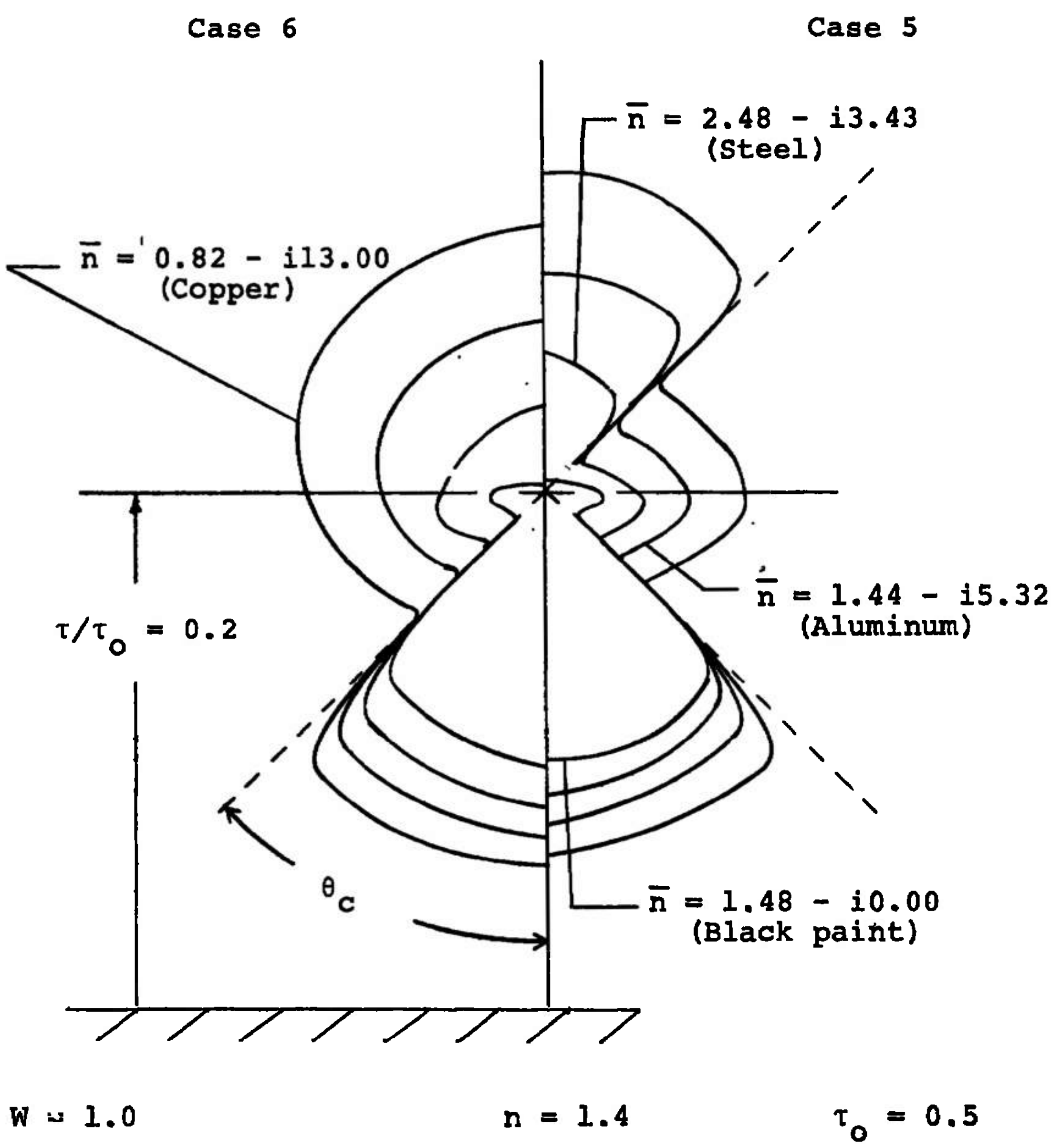

Figure 45. Comparison of the angular dimensionless intensity profiles between case 5 and case 6.

smooth or rough. Also Figure 44 indicates how thick a coating should be used to destroy the angular nature of the substrate. Figure 45 illustrates quite clearly how the magnitude and profile shape are different due to the angular nature of the substrate.

Now that the basic hemispherical-angular reflectance characteristics of all six models have been presented, the next objective is to choose the analytical model which best matches the experimental data presented in Chapter II.

One final comment about the analysis of the results presented in this chapter is in order here. For case 1 a closed form analytical expression for the initial reflectance drop was derived in Appendix B. It should be realized that when two reflecting interfaces are present, there is always an associated infinite series of reflections back and forth. When $\tau_o > 0$ there is also the influence of scattering coupled into the series of reflections. The coupling of these effects is sometimes difficult to analyze and only the influence of the dominant effects can usually be isolated. The initial drop for the other five cases can only be calculated numerically by setting $\tau_o = 0$ in the computer program, thus making the individual effects more difficult to isolate and analyze. The mathematical coupling of the boundary conditions is much stronger for the last five cases since they always involve at least one diffusely reflecting interface.

CHAPTER VI

SELECTION OF BEST ANALYTICAL MODEL

Several analytical models have been presented for the radiative characteristics of solid deposits on an opaque substrate. Attention has been focused toward gas films condensed on cryogenic surfaces in a vacuum with diffusely incident radiation. Based on the general trends of the data discussed in Chapter II, the model which best matches the experimental results shown for a cryodeposit and its substrate will now be chosen.

It should be obvious from comparison of Figures 2 and 3, pages 15 and 16, with Figures 7 and 10, pages 42 and 52, that in the visible wavelength region the albedo parameter must be large ($0.9 \leq W \leq 1.0$). Values of albedo less than 0.9 approach a limiting $\rho_{ha}(\mu_1)$ value and correspond to the near infrared and infrared wavelength regions where CO_2 and H_2O deposits have increased absorption.

All models investigated showed that the magnitude of the substrate reflectance had a strong influence on the hemispherical-angular reflectance for thin deposits. For very high albedo films the magnitude of the substrate reflectance was influential at all the optical thicknesses investigated. The substrate rapidly loses its influence for the more highly absorbing deposits.

In all cases considered a reflectance plateau occurred which was essentially independent of the substrate for the lower albedo deposits. That such a plateau is realistic for H_2O cryodeposits has been reported by Cunningham and Young [22] and also by Caren et al. [23]. Cunningham and Young [24] gathered non-monochromatic data for CO_2 deposits which approached a reflectance plateau, but a different plateau was reached for each substrate. This was attributed to the band absorption concept. Wood [3], however, has shown that on a monochromatic basis the CO_2 deposits do approach a common reflectance plateau for different substrate reflectances. As indicated in Chapter III the present analysis corresponds to a monochromatic or gray analysis, thus the analytical results presented herein would correspond to the data of Wood [3] and not to the results of Reference [24] which are associated with non-monochromatic reflectances involving an absorption band. In fact an absorption band study similar to the monochromatic one presented would be of interest to determine if the band structure theoretically shows the same trends as those of Reference [24]. Merriam [11] has shown results for a band model; however, the results are for optical thicknesses which are not large enough to determine whether one plateau for all substrates is attained or whether a separate plateau is reached for each different substrate.

The two general trends of the data thus far discussed have not resulted in any elimination of the six models. Experimentally it has been observed, such as in Figure 2, page 15, that the reflectance of a surface is a function of the viewing angle and that the larger viewing angles correspond to higher monochromatic reflectances. The theoretically diffuse reflector and transmitter has no angular dependence at all and the general trends of the results for cases 3 and 4 do not appear very similar to the data shown in Figures 2, 3, and 31, pages 15, 16, and 89. Another primary objection is that cases 3 and 4 have initial decreases which are much more drastic than indicated by the experimental data. In light of Figure 31, case 5 appeared to be a likely candidate. However, the viewing angle dependence is the reverse of the angular dependence of the experimental data shown in Reference [2].

Cases 1 and 2 satisfy the angular characteristics of the experimental data. The shape of the initial decreases in Figures 2 and 3 are similar to those for specular substrates rather than diffuse substrates. This is as should be expected since the stainless steel and copper substrates are very smooth and hence should reflect specularly.

The agreement of the general trends of the experimental results presented in Figure 3 with the analytical findings shown in Figure 7, page 42, were better than expected. Both indicate an initial decrease of approximately the same magnitude. Also the depth of the decrease for nonzero thicknesses in both cases is roughly at about $\rho_{ha}(\mu_1) = 0.38$. The change in $\rho_{ha}(\mu_1)$ with increasing viewing angle also seems to be in general agreement as illustrated in

Figures 2 and 9, pages 15 and 51. The values for the substrate refractive indices were taken from References [25] and [26]. The refractive index for black paint was taken from Reference [5]. The values used for both stainless steel and the black paint show very good agreement with the experimental results for the bare substrate reflectance and the initial reflectance decreases.

The quantitative results of the experimental data and case 1 were in good agreement with respect to general trends and magnitude, thus model one has been chosen as the best analytical model for the cryodeposit. Since the agreement was better than had been expected, it was decided to try to obtain monochromatic radiative properties through use of hemispherical-angular reflectance data and model one.

CHAPTER VII

INITIAL GUESS CRITERIA

In Chapter IV the numerical solution to the radiative transport equation was described. As with many numerical iterative boundary valued problems, it is of fundamental importance to have the capability of making a wise initial guess at the solution. Usually in boundary valued problems the initial guess is made at one of the boundaries. Then the numerical iterative scheme proceeds from one boundary to the other and then back again to the starting boundary to check with the previous values calculated at the starting boundary to determine if the iterative scheme is diverging or whether the scheme has satisfactorily converged to a solution within a given tolerance.

Often the entire success of a numerical iterative scheme depends on the ability to make an initial guess which will lead to the convergence of a satisfactory solution. Also an intelligent initial guess can often significantly reduce the amount of computer time required to obtain a solution and hence add to the versatility of the computer program. Short computing times permit a deeper understanding of the physical phenomena by allowing computer time for greater variation of the governing parameters.

The basic objective is to make a simplifying assumption which will permit the derivation of an algebraic expression that can be used as an effective initial guess. Such an expression is valuable because it would permit calculations of the initial guess rather than requiring the reading of input data cards. The most valuable property of such an expression is that every time the input parameters are varied the initial-guess expression automatically handles the new input parameters. This saves reading a different set of input data cards each time one of the governing parameters such as albedo, optical thickness, deposit refractive index, substrate refractive index or interface reflection function are varied to a new value or if a combination of these parameters are changed.

The radiative transport equation is presented again in dimensional form for the sake of convenience:

$$\mu\frac{di(x,\mu)}{dx} = -\beta\ i(x,\mu) + \frac{\sigma}{2}\int_{-1}^{1} i(x,\mu')d\mu' \tag{44}$$

The intensity in the upward direction will be denoted $i^{+}(x,\mu)[0 \le \mu \le 1]$ and the intensity in the downward direction will be denoted $i^{-}(x,\mu)[-1 \le \mu \le 0]$. This convention leads to two intergrodifferential equations, one for the upward intensity and one for the downward intensity, which have the forms

$$\mu\ \frac{di^{+}(x,\mu)}{dx} = -\beta\ i^{+}(x,\mu) + \frac{\sigma}{2}\int_{-1}^{0} i^{-}(x,\mu')d\mu'$$

$$+ \frac{\sigma}{2} \int_{0}^{1} i^{+}(x,\mu')d\mu' \tag{45}$$

and

$$\mu \frac{di^{-}(x,\mu)}{dx} = -\beta i^{-}(x,\mu) + \frac{\sigma}{2} \int_{-1}^{0} i^{-}(x,\mu')d\mu'$$

$$+ \frac{\sigma}{2} \int_{0}^{1} i^{+}(x,\mu')d\mu' \tag{46}$$

In order to have $i^{-}(x,\mu)$ take on values of μ in the range $0 \leq \mu \leq 1$ it is necessary to replace μ by $-\mu$ in Equation 46 which yields:

$$-\mu \frac{di^{-}(x,-\mu)}{dx} = -\beta i^{-}(x,-\mu) + \frac{\sigma}{2} \int_{0}^{1} i^{-}(x,-\mu)d\mu'$$

$$+ \frac{\sigma}{2} \int_{0}^{1} i^{+}(x,\mu')d\mu' \tag{47}$$

and Equation 45 can be written as

$$\mu \frac{di^{+}(x,\mu)}{dx} = -\beta i^{+}(x,\mu) + \frac{\sigma}{2} \int_{0}^{1} i^{-}(x,-\mu)d\mu'$$

$$+ \frac{\sigma}{2} \int_{0}^{1} i^{+}(x,\mu')d\mu' \tag{48}$$

where now both Equations 47 and 48 are valid in the range $0 \leq \mu \leq 1$.

As yet no additional assumptions have been made which have not already been discussed in Chapter III. At this point let the simplifying assumption be made that $i^+(x,\mu) = i^+(x)$ and $i^-(x,-\mu) = i^-(x)$. These are the basic assumptions employed in the two-flux method described in Hottel [34]. Enforcing these assumptions in Equations 47 and 48 yields

$$\mu_k \frac{di^+}{dx} = -\beta i^+ + \frac{\sigma}{2} i^- + \frac{\sigma}{2} i^+ \tag{49}$$

and

$$-\mu_k \frac{di^-}{dx} = -\beta i^- + \frac{\sigma}{2} i^- + \frac{\sigma}{2} i^+ \tag{50}$$

where μ_k corresponds to any specified direction inside the deposit such as a positive quadrature direction and where $0 < \mu_k \leq 1$. Since i^+ and i^- were assumed independent of μ, the integrals in Equations 47 and 48 were easily integrated. Simplifying the terms in Equations 49 and 50 with the relation $\beta = \sigma + k$ gives the results:

$$\frac{di^+}{dx} = \frac{-[k + (\sigma/2)]}{\mu_k} i^+ + \frac{\sigma}{2\mu_k} i^- \tag{51}$$

and

$$\frac{di^-}{dx} = \frac{-\sigma i^+}{2\mu_k} + \frac{[k + (\sigma/2)]}{\mu_k} i^- \tag{52}$$

Thus the assumption that the intensity in both the upward and downward directions is independent of μ has made possible the transformation of the integrodifferential transport equation into two simultaneous linear differential equations. Now let the further restrictions be added that the scattering coefficient, σ, and the absorption coefficient, k, are independent of x. The problem thus becomes the solution of two simultaneous linear ordinary differential equations with constant coefficients. The method of solution is to calculate the eigenvalues and eigenvectors corresponding to the coefficient matrix. The coefficient matrix is given by

$$\begin{bmatrix} \dfrac{-[k + (\sigma/2)]}{\mu_k} & \dfrac{\sigma}{2\mu_k} \\ \\ -\dfrac{\sigma}{2\mu_k} & \dfrac{[k + (\sigma/2)]}{\mu_k} \end{bmatrix} \tag{53}$$

The eigenvalues are those values of λ which satisfy the determinant

$$\begin{vmatrix} \dfrac{-[k + (\sigma/2)]}{\mu_k} - \lambda & \dfrac{\sigma}{2\mu_k} \\ \\ -\dfrac{\sigma}{2\mu_k} & \dfrac{[k + (\sigma/2)]}{\mu_k} - \lambda \end{vmatrix} = 0 \qquad (54$$

Expansion of the determinant yields

$$\lambda^2 - \frac{(k^2 + k\sigma)}{\mu_k^2} = 0 \tag{55}$$

therefore the eigenvalues are

$$\lambda_1 = \frac{\sqrt{k^2 + k\sigma}}{\mu_k} \tag{56}$$

and

$$\lambda_2 = -\frac{\sqrt{k^2 + k\sigma}}{\mu_k} \tag{57}$$

The eigenvectors associated with λ_1 which has column components v_{11} and v_{21} and with λ_2 which has column components v_{12} and v_{22} are calculated by the matrix equations

$$\begin{bmatrix} -\left(\frac{[k + (\sigma/2)] + \sqrt{k^2 + k\sigma}}{\mu_k}\right) & \frac{\sigma}{2\mu_k} \\ -\frac{\sigma}{2\mu_k} & \left(\frac{[k + (\sigma/2)] - \sqrt{k^2 + k\sigma}}{\mu_k}\right) \end{bmatrix} \begin{bmatrix} v_{11} \\ v_{21} \end{bmatrix} = 0 \tag{58}$$

and

$$\begin{bmatrix} -\left(\frac{[k + (\sigma/2)] - \sqrt{k^2 + k\sigma}}{\mu_k}\right) & \frac{\sigma}{2\mu_k} \\ -\frac{\sigma}{2\mu_k} & \left(\frac{[k + (\sigma/2)] + \sqrt{k^2 + k\sigma}}{\mu_k}\right) \end{bmatrix} \begin{bmatrix} v_{12} \\ v_{22} \end{bmatrix} = 0$$

Solution of the Equations 58 and 59 gives the results:

$$v_{11} = v_{22} = \frac{\sigma}{2\mu_k} \tag{60}$$

$$v_{21} = v_{12} = \left[\frac{[k + (\sigma/2)] + \sqrt{k^2 + k\sigma}}{\mu_k}\right] \tag{61}$$

The expressions for the solutions $i^+(x)$ and $i^-(x)$ have the forms:

$$i^+(x) = A\, v_{11}\, e^{\lambda_1 x} + B\, v_{12}\, e^{\lambda_2 x} \tag{62}$$

$$i^-(x) = A\, v_{21}\, e^{\lambda_1 x} + B\, v_{22}\, e^{\lambda_2 x} \tag{63}$$

where A and B are the two constants of integration. The coordinate system is the same as that shown in Appendix B; therefore, the boundary conditions are $i^+(0) = i_o^+$ at $x = 0$ and $i^-(L) = i_o^-$ at $x = L$.

Substitution of the eigenvalues, eigenvectors and the boundary conditions into Equations 62 and 63 facilitates the evaluation of the integration constants which, after much tedious algebra, are:

$$B = \frac{\left[i_o^- - \frac{2i_o^+}{\sigma}\{k + (\sigma/2) + \sqrt{k^2 + k\sigma}\}e^{\alpha}\right]}{\left[\frac{\sigma\, e^{-\alpha}}{2\mu_k} - \frac{2}{\sigma\mu_k}\{k + (\sigma/2) + \sqrt{k^2 + k\sigma}\}B\right.} \tag{64}$$

where $\alpha = \sqrt{k^2 + k\sigma}\, L/\mu_k$ and

$$A = \frac{2\mu_k i_o^+}{\sigma} + \frac{2}{\sigma}\{k + (\sigma/2) + \sqrt{k^2 + k\sigma}\}B \tag{65}$$

The final algebraic task is to calculate the values of i_o^+ and i_o^- in terms of the interface reflectances and refractive indices. The expressions for i_o^+ and i_o^- are similar to Equations 170 and 171; in this case they are determined by

$$i_o^+ = \rho_{23}(\mu)i^-(0) \tag{66}$$

and

$$i_o^- = \rho_{21}(\mu)i^+(L) + [1 - \rho_{12}(\mu_1)]n^2 \tag{67}$$

The values of $i^-(0)$ and $i^+(L)$ are found by substitution of the eigenvalues, eigenvectors and integration constants (A and B) into Equation 63 evaluated at $x = 0$ and into Equation 62 evaluated at $x = L$. This produces two equations for the two unknowns i_o^+ and i_o^-. The algebra for the solution of i_o^+ and i_o^- is very tedious.

In order to summarize, the expressions for $i^+(x)$ which is associated with the intensity in the upward directions, and $i^-(x)$, which corresponds to the intensity in the downward directions, have been derived on the basis of assuming the intensity field to be independent of μ and that σ and k are constants.

After making considerable, laborious algebraic simplifications in the preceeding equations, the expressions for $i^+(x)$ and $i^-(x)$ can be given by the following quantities:

$$i^+ = \exp\left(\frac{-\sqrt{k^2 + k\sigma}}{\mu_k}\, x\right)\Bigg\{ i_o^+$$

$$+ \left[\frac{i_o^+[k + \sigma/2 - \sqrt{k^2 + k\sigma}]e^{-2\alpha} - \sigma i_o^- e^{-\alpha}}{\text{DEN}}\right]\Bigg\}$$

$$+ \left[\frac{(\sigma/2) i_o^- e^{-\alpha} - i_o^+[k + \sigma/2 + \sqrt{k^2 + k\sigma}]e^{-2\alpha}}{\text{DEN}}\right]$$

$$\times \exp\left[\frac{\sqrt{k^2 + k\sigma}}{\mu_k}\right] x \tag{68}$$

$$i^- = \exp\left[\frac{-\sqrt{k^2 + k\sigma}}{\mu_k}\, x\right]$$

$$\times \left[i_o^- e^{\alpha} + \frac{(\sigma/2) i_o^+ + \sigma i_o^-[k + \sigma/2 + \sqrt{k^2 + k\sigma}]e^{-2\alpha}}{\text{DEN}}\right]$$

$$+ \exp\left[\frac{\sqrt{k^2 + k\sigma}}{\mu_k}\, x\right]$$

$$\times \left[\frac{-(\sigma/2) i_o^+ e^{-2\alpha} + i_o^-[k + \sigma/2 + \sqrt{k^2 + k\sigma}]e^{-\alpha}}{\text{DEN}}\right] \tag{69}$$

where DEN $= [(k + \sigma/2)(1 - e^{-2\alpha}) + \sqrt{k^2 + k\sigma}(1 + e^{-2\alpha})]$ and i_o^+ and i_o^- are given by

$$i_o^+ = \frac{C}{D} \tag{70}$$

$$i_o^- = \frac{E}{F} \tag{71}$$

where

$$E = (1 - \rho_{12})n^2[-(k^2 + k\sigma)(e^{-4\alpha} + 2e^{-2\alpha} + 1)$$

$$- (k + \sigma/2)^2(e^{-4\alpha} - 2e^{-2\alpha} + 1)$$

$$+ 2(k + \sigma/2)\sqrt{k^2 + k\sigma}(e^{-4\alpha} - 1)$$

$$+ \rho_{23}(\sigma/2)(k + \sigma/2)(e^{-3\alpha} - 2e^{-2\alpha} - e^{-\alpha} + 1)$$

$$- \rho_{23}(\sigma/2)\sqrt{k^2 + k\sigma}(e^{-3\alpha} - e^{-2\alpha} - e^{-\alpha} - 1) \qquad (72)$$

$$F = [(k^2 + k\sigma)(\rho_{21}\rho_{23} - 1)(e^{-4\alpha} + 2e^{-2\alpha} + 1)$$

$$+ 2(k + \sigma/2)\sqrt{k^2 + k\sigma}(e^{-4\alpha} - 1) - (k + \sigma/2)^2$$

$$\times (e^{-4\alpha} - 2e^{-2\alpha} + 1)(1 + \rho_{21}\rho_{23}) + \frac{\sigma^2}{4}\rho_{21}\rho_{23}$$

$$\times (e^{-4\alpha} - e^{-3\alpha} - e^{-2\alpha} + e^{-\alpha}) + (\sigma/2)(k + \sigma/2)$$

$$\times \{\rho_{23}(e^{-3\alpha} - e^{-2\alpha} - e^{-\alpha} + 1)$$

$$+ \rho_{21}(e^{-4\alpha} - 2e^{-2\alpha} + 1) \quad - (\sigma/2)\sqrt{k^2 + k\sigma}$$

$$\times \{\rho_{23}(e^{-3\alpha} - e^{2\alpha} + e^{-\alpha} + 1) + \rho_{21}(e^{-4\alpha} - 1)\}$$

$$- 2\rho_{23}\rho_{21}(k + \sigma/2)^2(e^{-4\alpha} - 2e^{-2\alpha} + 1)] \qquad (73)$$

$$C = \rho_{23}(-2\sqrt{k^2 + k\sigma})e^{-\alpha}E \qquad (74)$$

$$D = [(k + \sigma/2)(e^{-2\alpha} - 1) - \sqrt{k^2 + k\sigma}(e^{-2\alpha} + 1)$$

$$- \rho_{23}(\sigma/2)(e^{-\alpha} - 1)]F \qquad (75)$$

These equations permit the ability to make an initial guess of the intensity field not only at the boundaries but also at any position, x, throughout the deposit. The equations appear to be monstrous, but they do constitute a closed form expression involving only a calculation and no iteration. Such a computation would be ridiculous to attempt by hand; however, these equations can be evaluated in a fraction of a second and with great accuracy by a high speed digital computer. The same type of assumptions can also be used to generate an initial guess even if the scattering is anisotropic.

Since the intensity field can be guessed at every point within the deposit, these equations allow a guess of the intensity field in all of the quadrature directions at each numerical integration station. Thus if 51 stations are used and 10 quadrature points are employed, then 510 guesses are made. Use of these equations are certainly more convenient than reading 510 input data cards.

Originally it was attempted to make only an initial guess of the intensity at one boundary and then proceed back and forth with the numerical solution. This did not lead to a convergent solution for all cases since the initial guess is better for some cases than others. Since convergence could not be obtained for all cases it was decided to make an initial guess at the entire intensity field and using the numerical scheme as described in Chapter IV, there were no cases encountered where convergence was not obtained. Thus the initial guess equations not only provide starting values but they also help to stabilize the numerical scheme and thus avoid any divergent solutions. It is believed that not having the ability to make an initial guess, which would lead to stable convergence, is probably the difficulty encountered in Reference [12] at high W values and also the reason why numerical solutions to the transport equation are not widespread.

These initial guess equations can be transferred into terms of τ, τ_o, and W instead of L, x, σ, and k quite easily via the relations

$$W = \frac{\sigma}{\sigma + k}, \quad \tau = (\sigma + k)x, \text{ and } \tau_o = (\sigma + k)L$$

As a means of indicating the accuracy of the initial guess, Equations 68 and 69 have been used to calculate $\rho_{ha}(\mu_1)$ via the expression

$$\rho_{ha}(\mu_1) = \rho_{12}(\mu_1) + \frac{[1 - \rho_{21}(\mu)]}{n^2} i^+(L) \tag{80}$$

Figures 46 and 47 illustrate the correspondence between the numerical solution for case 1 and Equation 80. The initial guess equations were also used for the other five cases investigated; no significant increase in computer time was noticed in using the initial guess for the other cases and convergence was always obtained.

In general it was found that for a given W value the initial guess was better for low reflecting substrates. For a given substrate reflectance the initial guess improved as

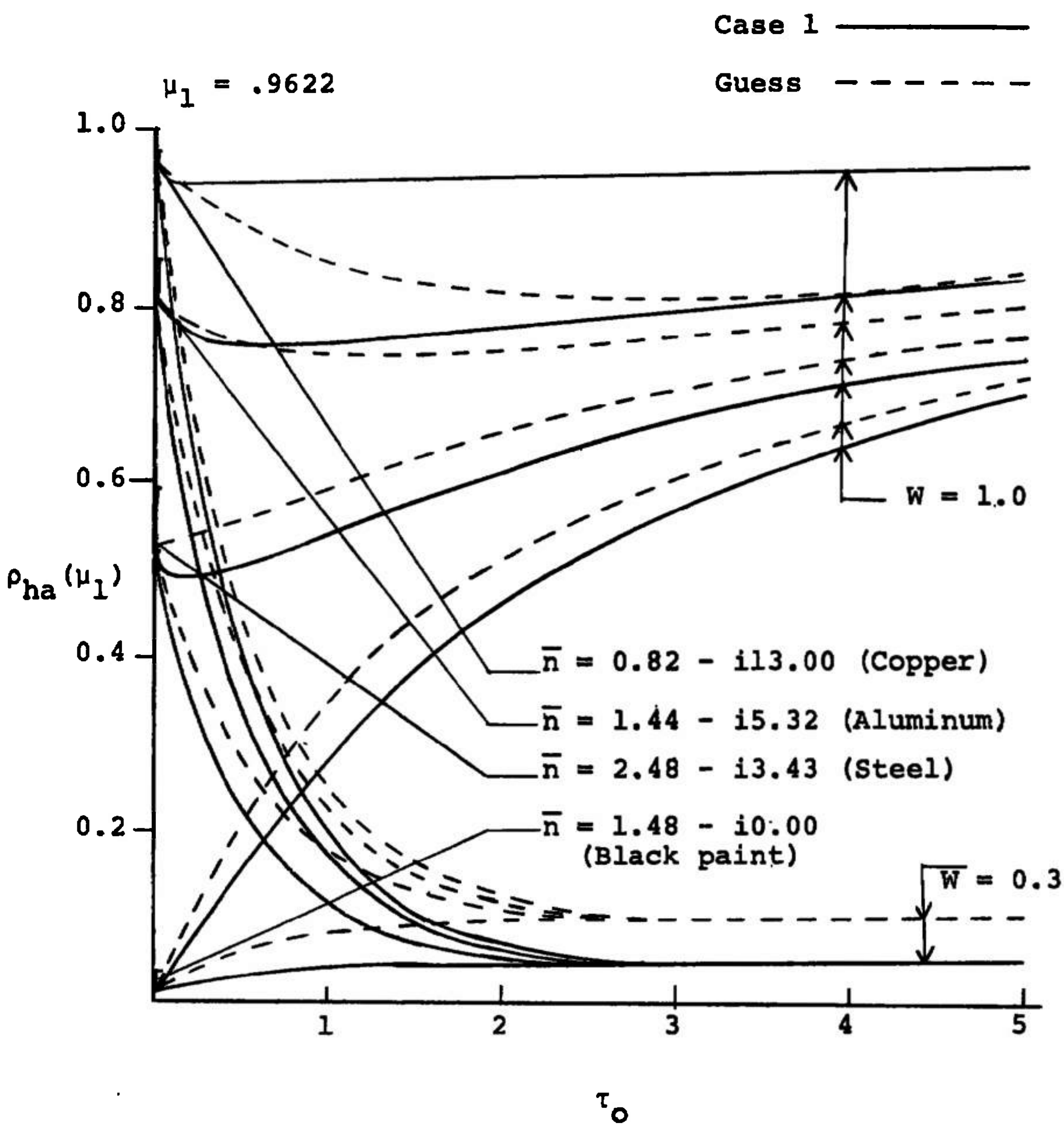

Figure 46. Comparison of the initial guess criteria and the numerical solution for n = 1.2.

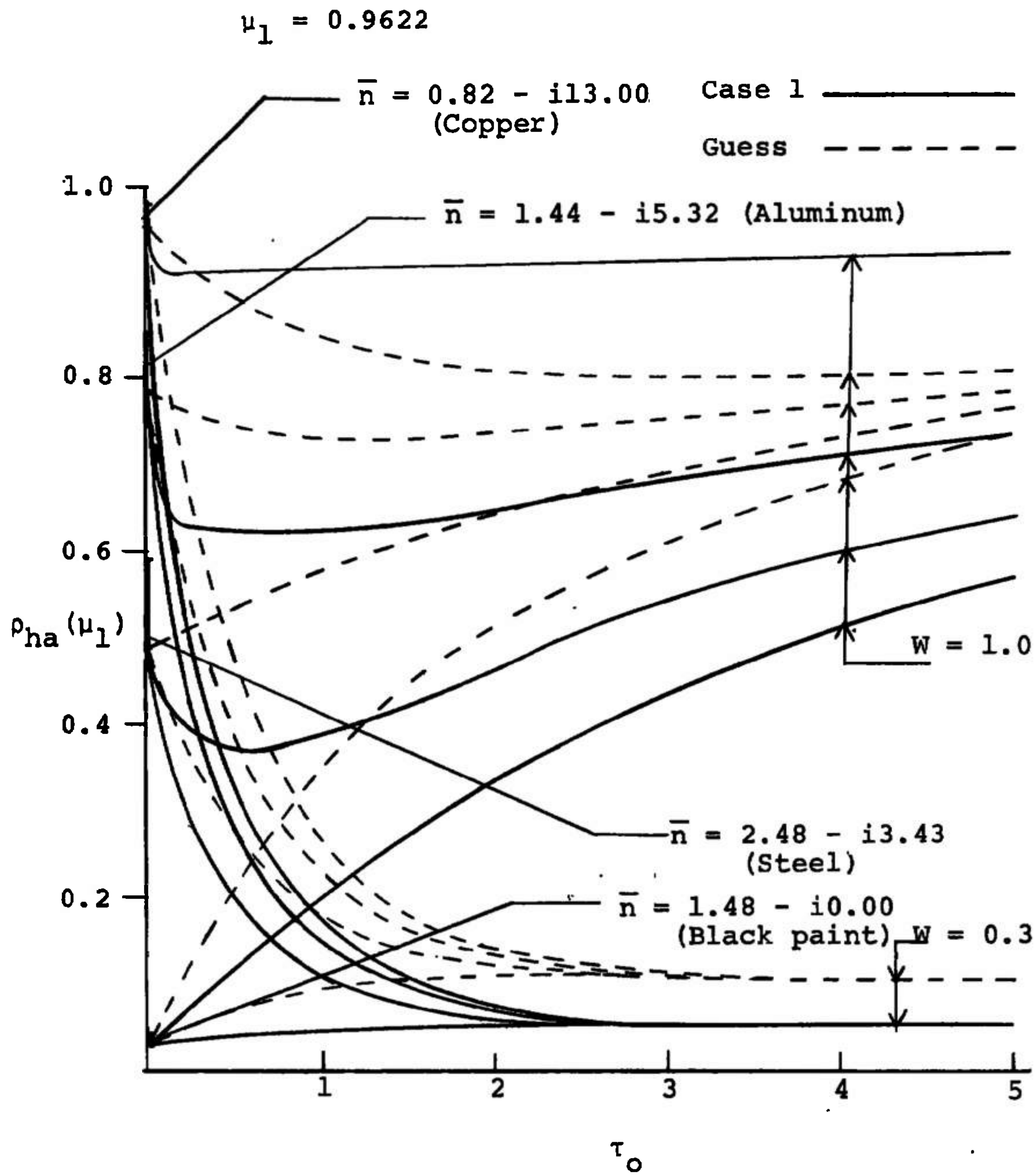

Figure 47. Comparison of the initial guess criteria and the numerical solution for n = 1.4.

the albedo decreased. As evident by Figures 46 and 47 the initial guess was also best for $n = 1.2$.

For the limiting case of no scattering ($\sigma = 0$) the initial guess equations reduce to exactly those which can be derived in closed form as in Love [7]. The initial guess equations can also be shown to reduce to Equation 176 at $L = 0$. For the limiting cases of $k = 0$ or $L = \infty$ no conclusions could be obtained since these limiting cases lead to an indetermined form requiring the use of L'hospital's rule. The complexity of the algebraic expressions do not readily lend them useful to L'hospital's rule which probably may have to be employed many times before arriving at an expression for $\rho_{ha}(\mu_1)$ at $k = 0$ or $L = \infty$.

CHAPTER VIII

DISCUSSION OF ERROR

In Chapter VII the initial guess criteria was presented for a first estimate at the solution of the transport equation. The iterative scheme and the numerical formulas used in the formal solution were described in Chapter IV. Now a discussion of the numerical error will be presented in order that confidence in the results presented may be achieved. It should be remembered that all numerical formulas are approximate since they usually involve the truncation of a Taylor's series. The calculation of the error associated with numerical integration is also approximate. The purpose of the error terms is to offer a means of obtaining a general idea of the error committed by numerical integration using a particular step size.

The first error involved is through the use of the method of discrete ordinates. Since the intensity field is actually constructed from the use of the Gaussian quadrature, it is difficult to approximate the error associated with a given order of quadrature. In Chapter IV a discussion was presented concerning the different orders of quadrature used by the authors of [9], [13], [11], and [10]. The general concensus is that eight quadrature points seems to be sufficient to insure good accuracy. The most convincing proof was given in Reference [10]; the authors used quadratures of orders 4, 12, 20, and 24. The results shown for the comparison of different orders of quadrature indicated a negligible change between the 4 point and 24 point quadratures. Also no improvement of accuracy was noticed between employing the single or double Gaussian quadratures. Based on the results and experience of the above authors it was decided to use the 10 point single Gaussian quadrature for this investigation in order to insure sufficient accuracy.

The predictor-corrector method is very convenient because it provides a simple expression for the error per step estimate. Call $E_{pr}(\tau_{n+1})$ the error in computing $i_{pr}(\tau_{n+1})$ by using Equation 25; call $E_{co}(\tau_{n+1})$ the error in computing $i_{co}(\tau_{n+1})$ by Equation 26 to correct this predicted value of $i_{pr}(\tau_{n+1})$. Let $Y(\tau_{n+1})$ be the actual value of $i(\tau_{n+1})$, then

$$E_{co}(\tau_{n+1}) = Y(\tau_{n+1}) - i_{co}(\tau_{n+1}) \tag{81}$$

$$E_{pr}(\tau_{n+1}) = Y(\tau_{n+1}) - i_{pr}(\tau_{n+1}) \tag{82}$$

Subtracting the first equation from the second gives

$$i_{co}(\tau_{n+1}) - i_{pr}(\tau_{n+1}) = E_{pr}(\tau_{n+1}) - E_{co}(\tau_{n+1}) \tag{83}$$

The expressions for the error terms of the predictor and corrector are given respectively by

$$E_{pr}(\tau_{n+1}) = \frac{28}{90} h^5 \, i^{(5)} \, (X_1) \tag{84}$$

$$E_{co}(\tau_{n+1}) = -\frac{1}{90} h^5 i^{(5)} (X_2) \tag{85}$$

where X_1 is contained in the interval (τ_{n-3}, τ_{n+1}) and X_2 is contained in the interval (τ_{n-1}, τ_{n+1}). Let the assumption be made that h is sufficiently small so that the variation between $i^{(5)}(X_1)$ and $i^{(5)}(X_2)$ is negligible, then a small error is committed by using $i^{(5)}(X)$ as their approximate common value. Hence subtracting Equation 85 from Equation 84 and replacing $i^{(5)}(X_1)$ and $i^{(5)}(X_2)$ by $i^{(5)}(X)$, results in

$$E_{pr}(\tau_{n+1}) - E_{co}(\tau_{n+1}) = \frac{29}{90} h^5 i^{(5)} (X) \tag{86}$$

Combining Equations 83 and 86 yields

$$i_{co}(\tau_{n+1}) - i_{pr}(\tau_{n+1}) = \frac{29}{90} h^5 i^{(5)}(X) = -29E_c(\tau_{n+1}) \tag{87}$$

and therefore

$$E_{co}(\tau_{n+1}) = [i_{pr}(\tau_{n+1}) - i_{co}(\tau_{n+1})]/29 \tag{88}$$

Equation 88 gives an approximate error formula for the error committed per step of numerical integration by the Milne predictor-corrector method.

For the purpose of plotting results which would indicate the significant general trends, it was decided that the total maximum error between two successive iterations of $i(\tau_o, \mu)[i = 1, \ldots, p/2]$ should be less than 0.001, thus the error per step should be less than 0.001 divided by the total number of steps. Since 50 steps were used, the difference between predictor and corrector at any station τ, for each quadrature direction should be

$$i_{pr}(\tau_{n+1}) - i_{co}(\tau_{n+1}) = 29\ E_{co}(\tau_{n+1}) \tag{89}$$

and the value of $E_c(\tau_{n+1})$ is approximated by

$$E_{co}(\tau_{n+1}) = \frac{0.001}{\text{no. steps}} = \frac{0.001}{50} = .00002 \tag{90}$$

Thus at each integration station it was required that $i_{pr} - i_{co} < .00058$. Since the maximum optical thickness used was $\tau_o = 5.0$, this corresponds to a "maximum" value $h = 0.1$. Since the error per step is on the order of h^5, by Equation 85 the value of $E_{co}(\tau_{n+1}) \approx .00001$ which is less than the value required by Equation 90. The values presented correspond to the maximum error, and again it should be mentioned that these expressions give only a reasonable estimate of the error committed. If the difference between predictor and corrector is not less than .00058, the corrector may be used over again and again until two successive calculations are within the given tolerance. It was not necessary to use the corrector more than once except for $\tau_o = 5.0$ where at a few stations it was necessary for multiple use. As will be shown later, for the results requiring a maximum error of 0.001 in $i(\tau_o,\mu_\ell)[\ell = 1, \ldots, p/2]$ between two successive iterations, it was only necessary to perform the calculations in single precision. By a similar analysis as just presented it was possible to specify a maximum error of 10^{-5} between two successive iterations of $i(\tau_o,\mu_\ell)[\ell = 1, \ldots, p/2]$, if the calculations were performed in double precision.

So far only the analysis for approximating the error associated with the numerical formula has been presented. There are also round off errors associated with any numerical calculation scheme. An effective procedure for determining the magnitude of the round off error is to first carry out a calculation in single precision and then use double precision to see if any significant difference is present. However, the formula errors and round off errors are usually coupled together such that they cannot be separately approximated.

Probably the most effective method of approximation of the coupled error is not only to use double and single precision but also to simultaneously reduce the step size to one half its previous value and see if any radical changes occur. In an attempt to make sure that the accuracy of the solution was within the stated tolerance, the numerical solution was performed in both double and single precision and also for various step sizes. Tables I and II illustrate a comparison of the results for various step sizes and for the single and double precision calculations. The two tables are for different values of refractive index. As should be expected the small optical thickness is much more accurate than the large optical thickness since the

TABLE I

RESULTS FOR VARIOUS STEP SIZES AND FOR DOUBLE AND SINGLE PRECISION FOR CASE 1 AT n = 1.4 AND W = 1.0

Substrate	μ_1	τ_o	Eigen-value Solution	Double Precision 50 Steps	Double Precision 100 Steps	Single Precision 50 Steps	Single Precision 100 Steps	Single Precision 200 Steps
Black Paint	.94818	0.5	.1058	.1058	.1058	.1058	.1058	.1058
	.71185		.1208	.1208	.1208	.1208	.1208	.1208
n = 1.48 - i10.00	.94818	5.0	.5730	.5691	.5690	.5708	.5704	.5703
	.71185		.5882	.5845	.5844	.5861	.5857	.5856
Steel	.95818	0.5	.3757	.3760	.3760	.3760	.3760	.3760
	.71185		.3747	.3750	.3750	.3750	.3750	.3750
n = 2.48 - i3.43	.94818	5.0	.6312	.6259	.6259	.6281	.6281	.6343
	.71185		.6443	.6393	.6392	.6412	.6412	.6474
Aluminum	.94818	0.5	.6232	.6238	.6238	.6238	.6237	.6237
	.71185		.6163	.6168	.6168	.6168	.6168	.6168
n = 1.44 - i5.32	.94818	5.0	.7240	.7166	.7164	.7195	.7194	.7189
	.71185		.7338	.7266	.7165	.7293	.7293	.7287
Copper	.94818	0.5	.9252	.9271	.9271	.9264	.9263	.9262
	.71185		.9230	.9246	.9246	.9241	.9241	.9240
n = 0.82 - i13.0	.94818	5.0	.9274	.9310	.9311	.9309	.9308	.9307
	.71185		.9300	.9335	.9336	.9333	.9332	.9332

TABLE II

RESULTS FOR VARIOUS STEP SIZES AND FOR DOUBLE AND SINGLE PRECISION FOR CASE 1 AT n = 1.2 AND W = 1.0

Substrate	μ_1	τ_o	Eigen-value Solution	Double Precision 50 Steps	Double Precision 100 Steps	Single Precision 50 Steps	Single Precision 100 Steps	Single Precision 200 Steps
Black Paint	.96220	0.5	.1591	.1591	.1591	.1591	.1591	.1591
	.79850		.1742	.1742	.1742	.1742	.1742	.1742
	.47403		.2294	.2294	.2294	.2294	.2294	.2294
n = 1.48 - i10.00	.96220	5.0	.6903	.6863	.6861	.6878	.6878	.6877
	.79850		.7058	.7019	.7018	.7052	.7033	.7032
	.47403		.7391	.7356	.7356	.7367	.7368	.7366
Steel	.96220	0.5	.5013	.5015	.5015	.5015	.5015	.5015
	.79850		.5026	.5029	.5029	.5029	.5029	.5028
	.47403		.5190	.5192	.5192	.5192	.5192	.5192
n = 2.48 - i3.43	.96220	5.0	.7455	.7404	.7407	.7423	.7423	.7422
	.79850		.7581	.7533	.7535	.7550	.7550	.7549
	.47403		.7855	.7813	.7826	.7826	.7826	.7825
Aluminum	.96220	0.5	.7468	.7472	.7472	.7472	.7472	.7471
	.79850		.7444	.7448	.7448	.7447	.7447	.7446
	.47403		.7453	.7457	.7457	.7457	.7457	.7456
n = 1.44 - i5.32	.96220	5.0	.8222	.8346	.8346	.8346	.8346	.8345
	.79850		.8310	.8428	.8428	.8428	.8428	.8427
	.47403		.8501	.8606	.8606	.8606	.8606	.8605

TABLE II (continued)

Substrate	μ_1	τ_o	Eigen-value Solution	Double Precision 50 Steps	Double Precision 100 Steps	Single Precision 50 Steps	Single Precision 100 Steps	Single Precision 200 Steps
Copper	.96220	0.5	.9609	.9619	.9619	.9613	.9613	.9612
	.79850		.9603	.9611	.9611	.9607	.9607	.9606
	.47403		.9593	.9601	.9601	.9598	.9598	.9597
n = 0.82 - i13.00	.96220	5.0	.9597	.9709	.9709	.9706	.9706	.9705
	.79850		.9617	.9723	.9723	.9721	.9720	.9720
	.47403		.9660	.9755	.9754	.9752	.9752	.9751

corresponding step size is one-tenth that of the larger optical-thickness step size. In order to obtain added confidence in the solution, also indicated in the tables are the results of an eigenvalue solution.

Due to the stimulus of the author of this work an eigenvalue program was written by the A. E. F. programmers of ARO, Inc. The program was not completed and perfected until after the numerical results of this work were completed. As far as the results of this work are concerned the eigenvalue program should only be considered as a library program. The eigenvalue program was found to be successful for a matrix as large as 16 × 16. The agreement between the eigenvalue method and the numerical solution was very good as is evidenced by Tables I and II.

Now a brief sketch of the eigenvalue approach will be presented. After employing the method of discrete ordinates to obtain a system of differential equations as given by Equation 24, the problem is reduced to the solution of a system of linear ordinary simultaneous differential equations with constant coefficients. The coefficient matrix for the system of equations is given by

$$\left[\frac{W_{aj}}{2\mu_i} - \frac{\delta_{ij}}{\mu_i}\right] \qquad \begin{array}{l} i = 1, \ldots\ldots, p \\ j = 1, \ldots\ldots, p \end{array} \tag{91}$$

where δ_{ij} is Kronecker delta function. The objective is to calculate the eigenvalues and eigenvectors of Equation 91. Associated with each eigenvalue γ_k will be p values of X, called the column components of the eigenvector. The p components of the p eigenvectors constitute an eigenvector matrix $\{X_{i,k}\}$. The general form of the solution is

$$i(\tau,\mu_i) = \sum_{k=1}^{p} C_k \, X_{i,k} \, e^{\gamma_k \tau} \tag{92}$$

The quantities C_k are the p number of integration constants. Their values are determined through use of the boundary conditions presented in Chapter III. Using the boundary conditions leads to a system of p simultaneous linear nonhomogeneous algebraic equations to be solved for the C_k values.

The method of A. M. Danilevsky, as described by Faddeeva [12], was used to compute the coefficients of the characteristic polynomial and the eigenvectors of the given matrix. The eigenvalues of the characteristic polynomial were determined by the Newton-Raphson method. The simultaneous algebraic equations satisfying the intensity boundary conditions were solved for the coefficients, C_k, by application of the Cholesky matrix factorization method. The Gauss-Jordan method was originally employed to solve for C_k, but it was discovered that the matrix was ill conditioned for accurate use of this method.

It was very encouraging to see the close agreement between the eigenvalue method and the numerical solution. In general it was found that the eigenvalue method was about one and one-half times faster than the numerical solution.

However, the eigenvalue program could not handle a matrix larger than 16 × 16. The numerical solution was successfully employed for the equivalent of a 40 × 40 matrix as will be shown in Chapter X.

One inherent advantage of the numerical solution is that the coefficients of the differential equations may be variable whereas the eigenvalue approach is only applicable for differential equations with constant coefficients. Variable coefficients were not used in this work but the case of having W as a function of τ is very realistic for many physical problems such as for the analysis of the solar degradation of thermal control coatings.

CHAPTER IX

COMPARISON OF THEORY AND DATA

In Chapter VI it was shown that model one most closely simulated the experimental findings presented in Chapter II. The agreement was good not only with respect to general trends but also with respect to general magnitudes. Since the dimensionless results and the experimental results were so strikingly similar, it was decided to try to use the numerical solution and the reflectance data to determine radiative properties. No analysis has been found yet, by this author, whereby the monochromatic absorption and scattering coefficients have been simultaneously determined.

From the analytical results it has been seen that there are two governing parameters, τ_o and W. Also these two parameters are functions only of the two radiative properties, σ and k, by the relations

$$\tau_o = (\sigma + k)L \qquad W = \frac{\sigma}{\sigma + k} \tag{93}$$

It would be useful if an analysis could be developed where σ and k were the only two unknowns and therefore could be determined. In order to isolate σ and k as the only unknowns it is necessary to have available other optical properties of the deposit being investigated. First of all it is necessary to have the refractive index of the deposit as a function of wavelength; this data is provided in a limited wavelength region in Figures 4 and 5, pages 19 and 20. Also it is necessary to have available the refractive index data of the substrate as a function of wavelength. The refractive index of black paint, on which the data was taken, was determined by Müller [5] to be $\bar{n} = 1.48 - i\ 0.00$ at $\lambda = 0.7\mu$. The reflectance of the black paint at other wavelengths ($0.4\mu < \lambda < 1.1\mu$) was essentially constant and therefore it was assumed that the black-paint refractive index was constant in this wavelength region.

There are two reasons for preferring cryodeposit data taken on a black substrate for use in a computer program. First, as shown in Figure 21, page 72, the hemispherical-angular reflectance for a specular deposit on a black substrate is independent of whether the substrate is diffuse or specular at a viewing angle of approximately 20 degrees. Therefore any effect due to slight substrate roughness will not be evident on the hemispherical-angular reflectance data and thus the substrate effect is minimized. As shown for a stainless steel substrate, the result of having a diffuse or specular substrate can be quite strong at small optical thicknesses.

Secondly, the black substrate has essentially a constant refractive index in this region whereas the stainless steel substrate has significant spectral variation of reflectance in this wavelength region. There are many types of stainless steel and handbook values are only given at $\lambda = 0.589\mu$. Also since the substrate is a metal it has both a real and an imaginary component of refractive index. The determination of complex refractive indices is quite difficult and has not been performed in the A. E. F. thermal radiation laboratory. With the spectral data for both the cryodeposit and substrate given, there are only two monochromatic unknowns, σ and k.

The objective of the following is to generate an iterative procedure whereby a combination of experimental data and the radiative transport solution are employed to determine the radiative properties σ and k, (monochromatic absorption and scattering coefficients) of the cryodeposit. Two experimental data points (hemispherical-angular reflectance at two thicknesses at a given viewing angle) in conjunction with the solution to the transport equation will be used to solve for the two unknowns (coefficients) through use of the Newton-Raphson method. After determination of these two radiative properties at the two experimental points, these properties will be used to predict the hemispherical-angular reflectance at other experimental points (thicknesses) in order to confirm the validity of the radiative properties. Once the radiative properties have been determined, $\rho_{ha}(\mu_1)$ can be monochromatically predicted at any given thickness.

I. NEWTON-RAPHSON METHOD

Often in the solution of algebraic equations it is not easy to solve for the unknowns in closed form due to the non-linearity of the equations. One method of obtaining a solution is an iterative technique called the Newton-Raphson method.

Consider the following function

$$\rho_{ha}(L,\sigma,k,\rho_{12},\rho_{21},\rho_{23},\bar{n}_q,\mu) = \rho_{ha} \quad q = 1, 2, 3 \tag{94}$$

For a given deposit, substrate and for fixed viewing angles the values ρ_{12}, ρ_{21}, ρ_{23} and $\bar{n}_q$ are known as indicated in the preceding section. If, for these fixed values, the hemispherical-angular reflectance, $\rho_{ha}(\mu_1)$, is known at two thicknesses, L, then it should be possible to solve for σ and k.

Now for a given deposit, substrate, and viewing angle, Equation 94 reduces to

$$\rho_{ha}(L,\sigma,k) = \rho_{ha} \tag{95}$$

The experimental values of ρ^*_{ha}, at thickness L_1, and at thickness L_2, are known; thus there are two equations and two unknowns

$$\rho_{ha_1}(L_1,\sigma,k) - \rho^*_{ha_1} = 0 \tag{96}$$

$$\rho_{ha_2}(L_2,\sigma,k) - \rho^*_{ha_2} = 0 \tag{97}$$

from which it should be possible to solve for the scattering coefficient, σ, and the absorption coefficient, k. Expanding Equations 96 and 97 into Taylor's series about $\sigma^{(1)}$ and $k^{(1)}$, then retaining the first two terms yields:

$$0 = \rho_{ha_1}(L_1,\sigma^{(1)},k^{(1)}) - \rho^*_{ha_1} + \left.\frac{\partial\rho_{ha_1}}{\partial k}\right|_{L_1,\sigma^{(1)},k^{(1)}} (k^{(3)} - k^{(1)})$$

$$+ \left.\frac{\partial\rho_{ha_1}}{\partial\sigma}\right|_{L_1,\sigma^{(1)},k^{(1)}} (\ ^{(3)} - \ ^{(1)}) \tag{98}$$

$$0 = \rho_{ha_2}(L_2,\sigma^{(1)},k^{(1)}) - \rho^*_{ha_2} + \left.\frac{\partial\rho_{ha_2}}{\partial k}\right|_{L_2,\sigma^{(1)},k^{(1)}} (k^{(3)} - k^{(1)})$$

$$+ \left.\frac{\partial\rho_{ha_2}}{\partial\sigma}\right|_{L_2,\sigma^{(1)},k^{(1)}} (\sigma^{(3)} - \sigma^{(1)}) \tag{99}$$

where $\sigma^{(1)}$ and $k^{(1)}$ are the initial guesses at the values of σ and k which satisfy both Equation 96 and 97. The values $\sigma^{(3)}$ and $k^{(3)}$ are the newly computed values of σ and k given by

$$\sigma^{(3)} = \sigma^{(1)} + \frac{\begin{vmatrix} \dfrac{\partial\rho_{ha_1}}{\partial k} & (\rho^*_{ha_1} - \rho_{ha_1}) \\[2ex] \dfrac{\partial\rho_{ha_2}}{\partial k} & (\rho^*_{ha_2} - \rho_{ha_2}) \end{vmatrix}}{\begin{vmatrix} \dfrac{\partial\rho_{ha_1}}{\partial k} & \dfrac{\partial\rho_{ha_1}}{\partial\sigma} \\[2ex] \dfrac{\partial\rho_{ha_2}}{\partial k} & \dfrac{\partial\rho_{ha_2}}{\partial\sigma} \end{vmatrix}} \tag{100}$$

$$k^{(3)} = k^{(1)} + \frac{\begin{vmatrix} (\rho^*_{ha_1} - \rho_{ha_1}) & \dfrac{\partial\rho_{ha_1}}{\partial\sigma} \\ (\rho^*_{ha_2} - \rho_{ha_2}) & \dfrac{\partial\rho_{ha_2}}{\partial\sigma} \end{vmatrix}}{\begin{vmatrix} \dfrac{\partial\rho_{ha_1}}{\partial k} & \dfrac{\partial\rho_{ha_1}}{\partial\sigma} \\ \dfrac{\partial\rho_{ha_1}}{\partial k} & \dfrac{\partial\rho_{ha_2}}{\partial\sigma} \end{vmatrix}} \tag{101}$$

After the values $k^{(3)}$ and $\sigma^{(3)}$ are calculated, they are compared with $k^{(1)}$ and $\sigma^{(1)}$. If the difference converges to within the given tolerance then the solution is obtained.

The values of σ and k calculated in this work had to be within ±2 per cent on two successive iterations before convergence was considered to have been obtained. Therefore the radiative properties computed are considered to be accurate to within ±2 per cent of the indicated value.

When the two given equations are in closed form such as Equations 96 and 97 there is no difficulty in obtaining the values $\partial\rho_{ha}/\partial k$ and $\partial\rho_{ha}/\partial\sigma$ at given values of $\sigma^{(1)}$ and $k^{(1)}$. Also it is easy to evaluate Equation 95 at $\sigma^{(1)}$ and $k^{(1)}$, which is required in Equations 100 and 101. However, in the present case no closed form solutions are given, rather the information represented by Equation 95 at L_1 and L_2 are given in terms of numerical results. The values $\rho_{ha_1}(L_1,\sigma^{(1)},k^{(1)})$ and $\rho_{ha_2}(L_2,\sigma^{(1)},k^{(1)})$ are solved for by expressing

$$\tau_o = (\sigma^{(1)} + k^{(1)})L \qquad W = \frac{\sigma^{(1)}}{\sigma^{(1)} + k^{(1)}} \tag{102}$$

and then numerically solving the transport equation with the aid of the initial guess criteria of Chapter VII and the numerical scheme described in Chapter IV. The values $\partial\rho_{ha}/\partial\sigma$ and $\partial\rho_{ha}/\partial k$ are evaluated by the approximations

$$\frac{\partial \rho_{ha}}{\partial k} \simeq \frac{\Delta\rho_{ha}}{\Delta k} \tag{103}$$

$$\frac{\partial \rho_{ha}}{\partial \sigma} \simeq \frac{\Delta\rho_{ha}}{\Delta \sigma} \tag{104}$$

therefore

$$\left.\frac{\partial \rho_{ha_1}}{\partial k}\right|_{L_1,\sigma^{(1)},k^{(1)}} \simeq \frac{\rho_{ha_1}(L_1,\sigma^{(1)},k^{(2)}) - \rho_{ha_1}(L_1,\sigma^{(1)},k^{(1)})}{(k^{(2)} - k^{(1)})} \tag{105}$$

$$\left.\frac{\partial \rho_{ha_1}}{\partial \sigma}\right|_{L_1,\sigma^{(1)},k^{(1)}} \simeq \frac{\rho_{ha_1}(L_1,\sigma^{(2)},k^{(1)}) - \rho_{ha_1}(L_1,\sigma^{(1)},k^{(1)})}{(\sigma^{(2)} - \sigma^{(1)})} \tag{106}$$

where

$$\sigma^{(2)} = \sigma^{(1)} + .01\sigma^{(1)} \qquad k^{(2)} = k^{(1)} + .01k^{(1)} \tag{107}$$

It had to be assumed that the slope was approximately a straight line between the two points at which the ρ_{ha} values were calculated. Picking the values $k^{(2)}$ and $\sigma^{(2)}$ close to $\sigma^{(1)}$ and $k^{(1)}$ as indicated in Equation 107 proved to be adequate in evaluating the slope. However, picking $\sigma^{(2)}$ and $k^{(2)}$ this close in order to obtain a good derivative evaluation also required that two consecutive iterations of $i(\tau_o,\mu_\ell)[\ell = 1, \ldots, p/2]$ had a maximum error of less than 0.00001. This is because the values of ρ_{ha} used in Equations 105 and 106 sometimes only differed in the third decimal place or less. The data used for the two values of $\rho^*_{ha_1}$ and $\rho^*_{ha_2}$ were picked at thicknesses which would lead, via Equation 102, to optical thicknesses less than $\tau_o = 2.5$. As shown in Chapter VIII the error per step in ρ_{ha}, Equation 85, should be less than approximately

$$h^5 = \left(\frac{2.5}{50}\right)^5 = 3.125 \times 10^{-7}$$

Thus the error for 51 steps would be roughly 1.5×10^{-5} which is approximately what was desired (1.0×10^{-5}). Also the error between the predictor and corrector should be less than 5.8×10^{-6}. Of course, all calculations had to be performed in double precision (17 decimal places). The criteria for Equation 107 was that ρ_{ha} in Equations 105 and 106 would differ by no more than .01 and no less than .0001. This implies that in this range of ρ_{ha} values, the derivatives can be sufficiently approximated by Equations 103 and 104. It is felt that the magnitude of the error can be more easily approximated by the numerical solution than the eigenvalue method. Also the step size in the solution can be varied to reduce the error.

From the results for case 1 in Chapter V and the experimental results presented in Chapter II it should be obvious that in the visible wavelength region the range of W is $0.9 < W < 1.0$. The initial guesses $\sigma^{(1)}$ and $k^{(1)}$ were made by the use of a graph like Figure 48. For a given W, the value of τ_o is read for the corresponding ρ^*_{ha}. The thickness, L, is known at each ρ^*_{ha} value from the experimental data. Knowing L, W, and τ_o the values of σ and k can be determined from Equation 93. This is done for each experimental ρ^*_{ha} and L; if the calculated k and σ are approximately the same for all the experimental thicknesses then these are used as $\sigma^{(1)}$ and $k^{(1)}$. If the k and σ values calculated at each thickness vary greatly, the above computations are carried out for the next W curve. This process is continued until a satisfactory $\sigma^{(1)}$ and $k^{(1)}$ are obtained.

II. THEORY AND DATA COMPARISON

Using the analysis presented in the previous section, the determination of the radiative properties of the media was attempted. The solutions given for the transport equation are in the quadrature directions and the data was taken at an angle of 20 degrees. Figures 49 through 53 show the comparison of the analytical and experimental results for the H_2O cryodeposit at several wavelengths. Figures 54 through 59 show the same comparison for the CO_2 cryodeposit. The data used was obtained from B. A. Seiber. The analysis was limited to the visible wavelength range because this was

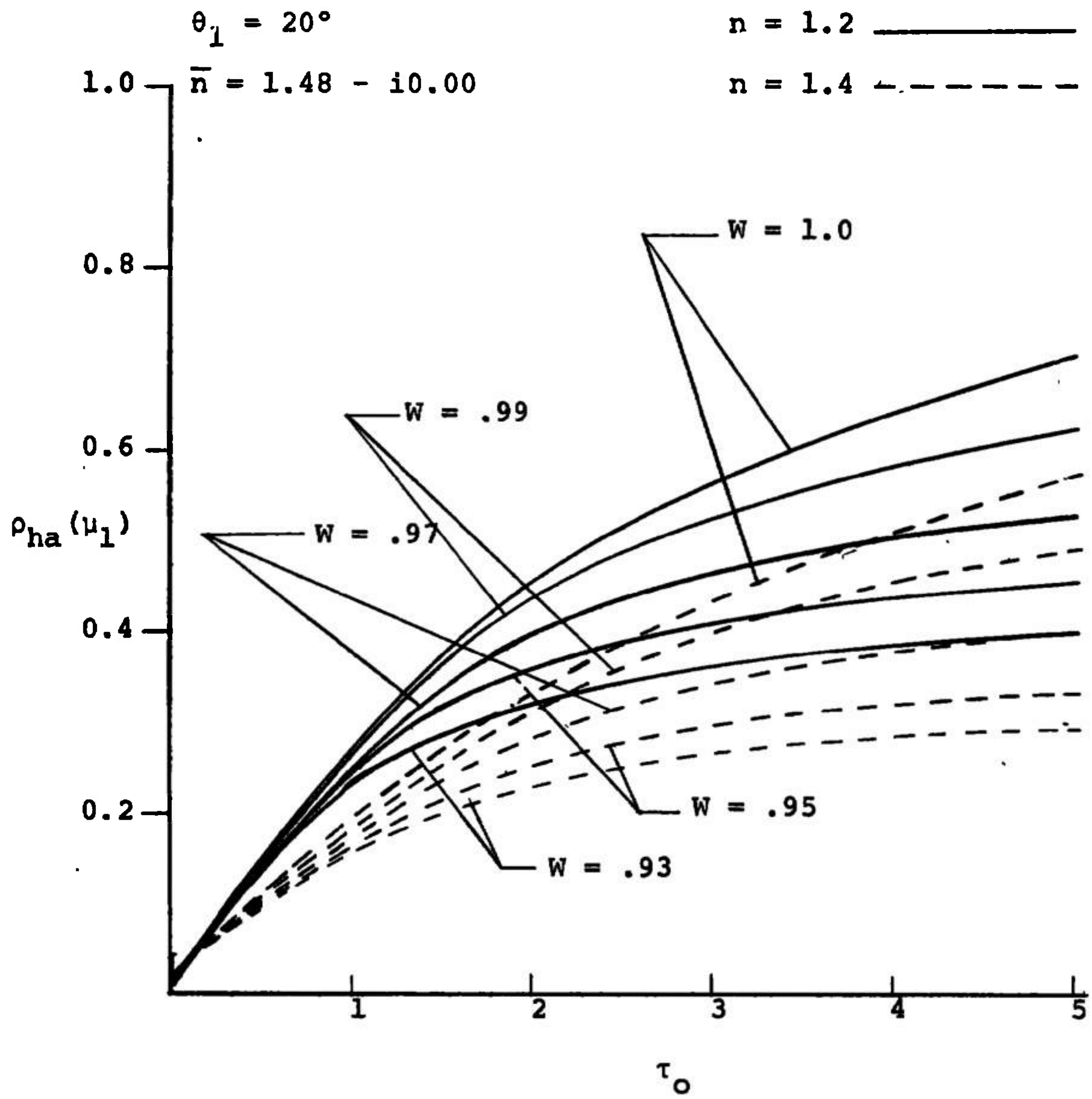

Figure 48. Results used for making an initial guess for σ and k.

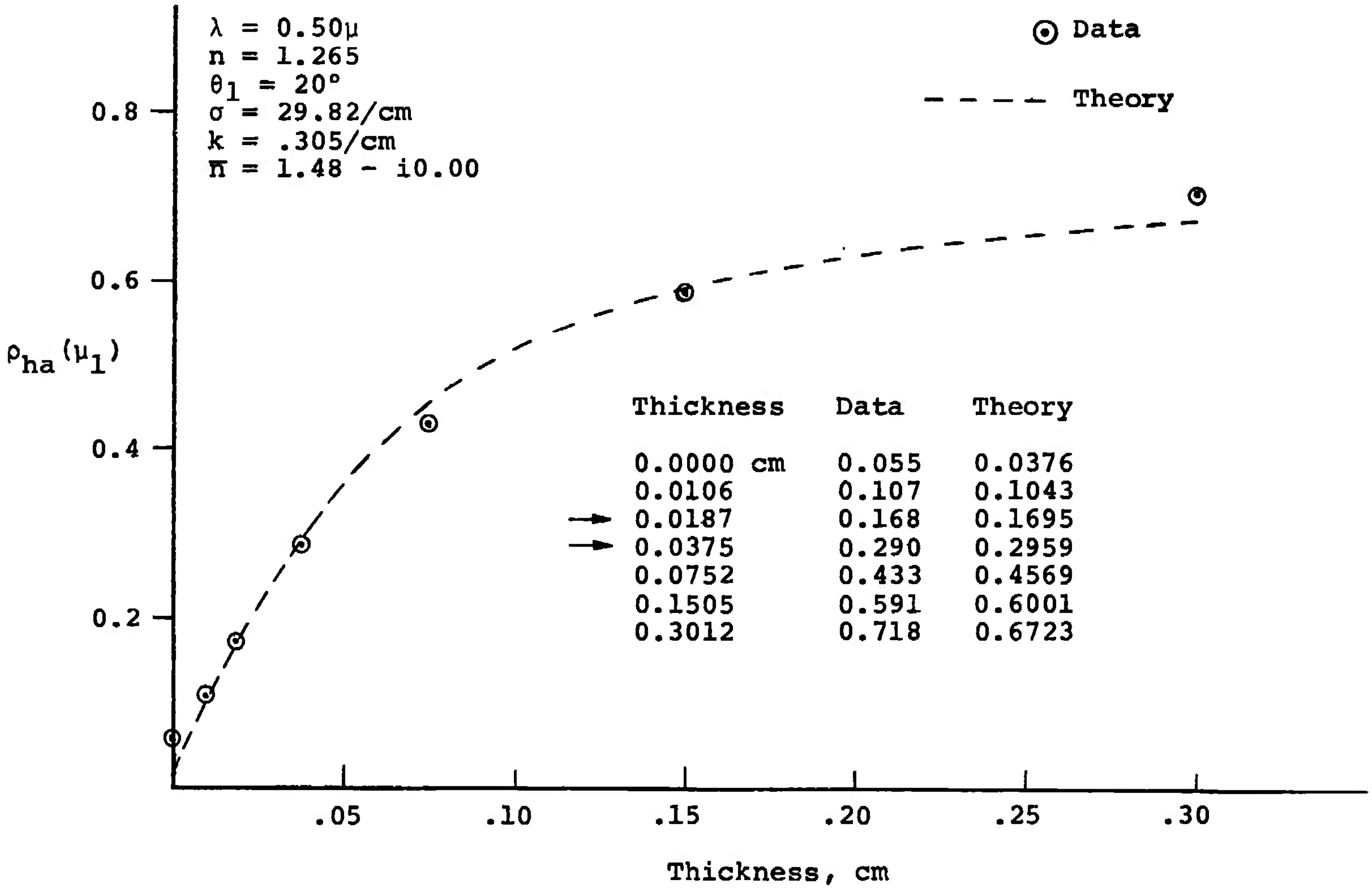

Thickness	Data	Theory
0.0000 cm	0.055	0.0376
0.0106	0.107	0.1043
→ 0.0187	0.168	0.1695
→ 0.0375	0.290	0.2959
0.0752	0.433	0.4569
0.1505	0.591	0.6001
0.3012	0.718	0.6723

Figure 49. Comparison of theory and data for a H_2O cryodeposit on a black paint substrate at $\lambda = 0.50\mu$.

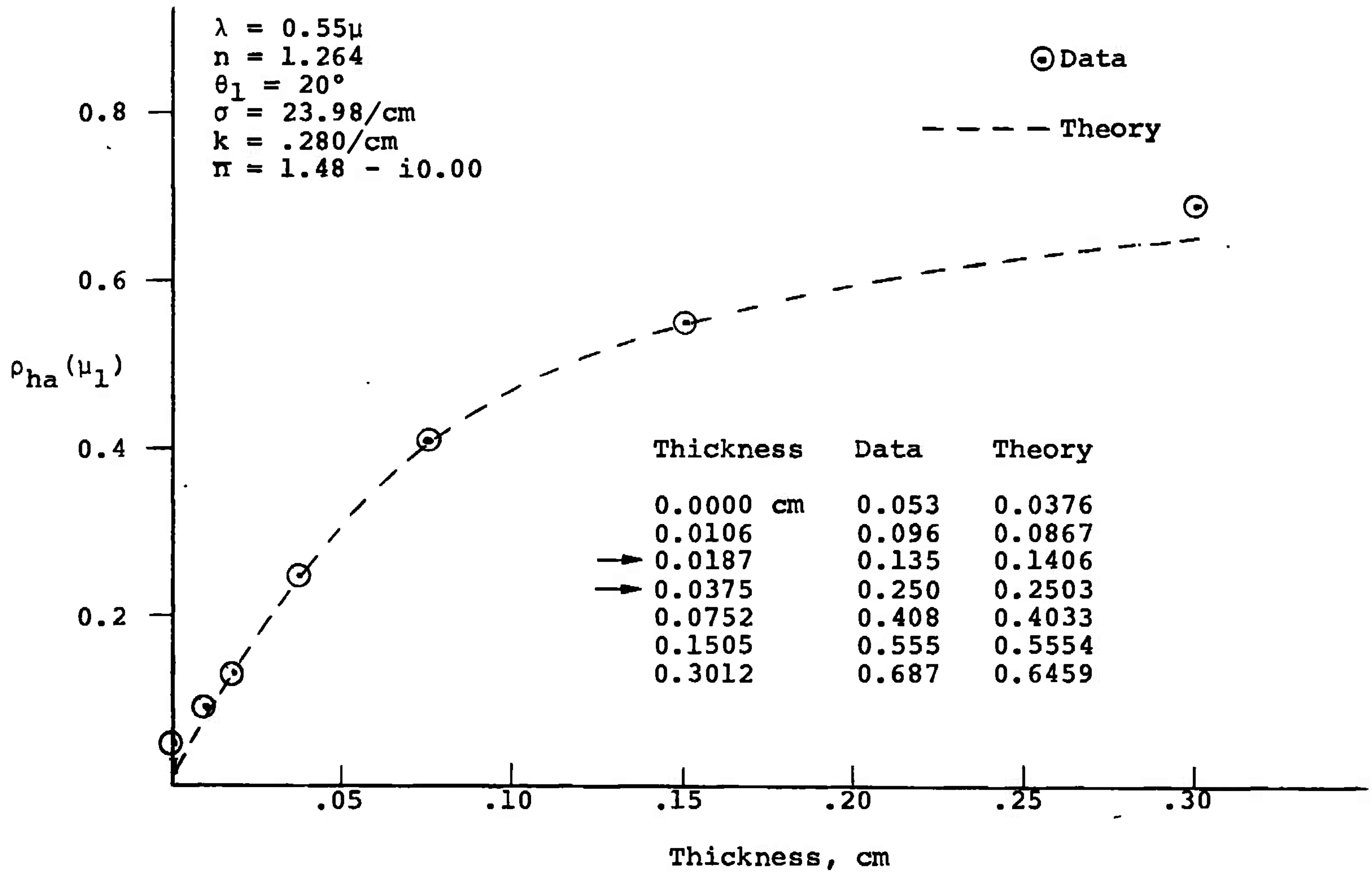

Figure 50. Comparison of theory and data for a H_2O cryodeposit on a black paint substrate at $\lambda = 0.55\mu$.

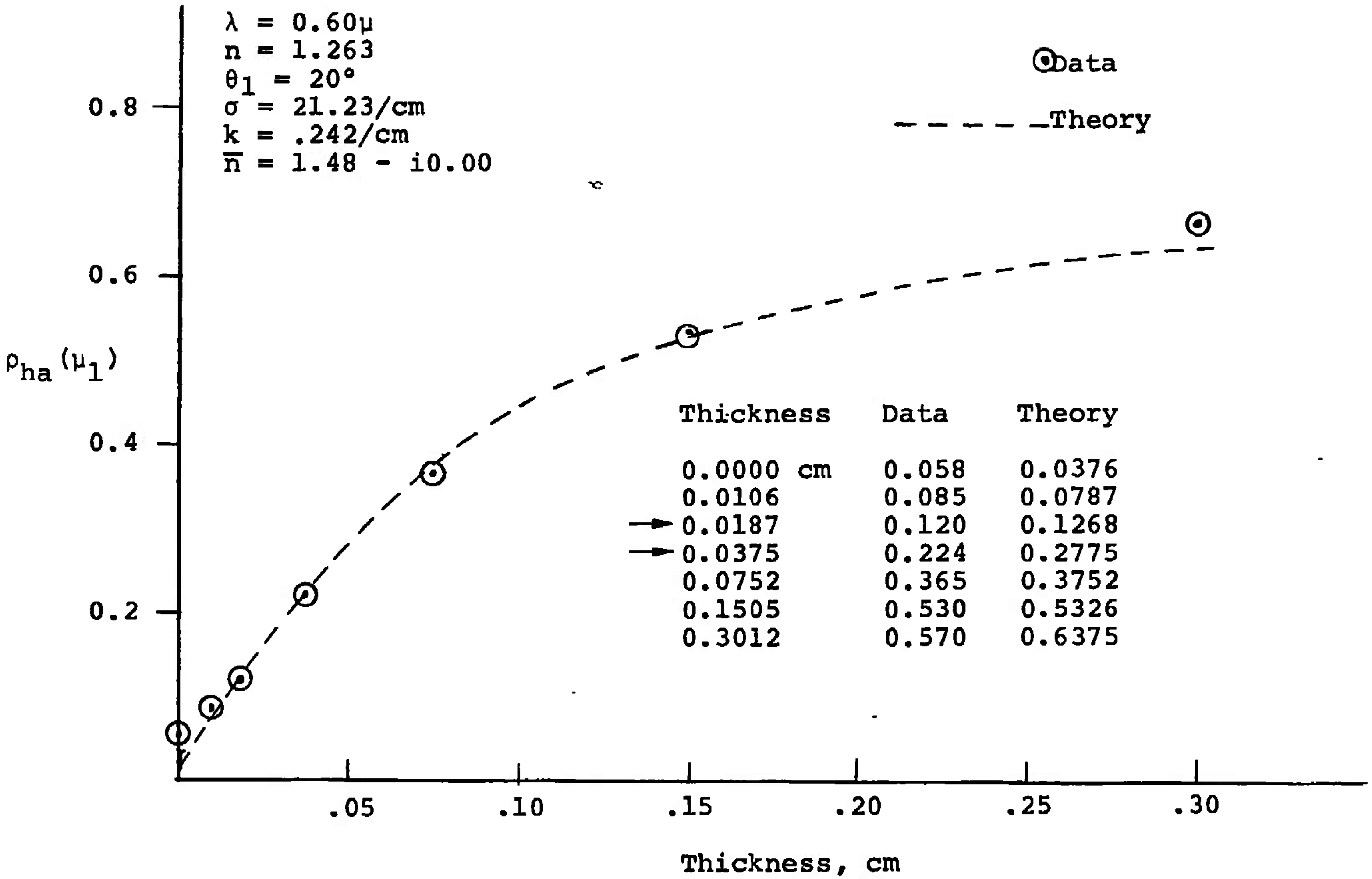

Thickness	Data	Theory
0.0000 cm	0.058	0.0376
0.0106	0.085	0.0787
→ 0.0187	0.120	0.1268
→ 0.0375	0.224	0.2775
0.0752	0.365	0.3752
0.1505	0.530	0.5326
0.3012	0.570	0.6375

Figure 51. Comparison of theory and data for a H_2O cryodeposit on a black paint substrate at $\lambda = 0.60\mu$.

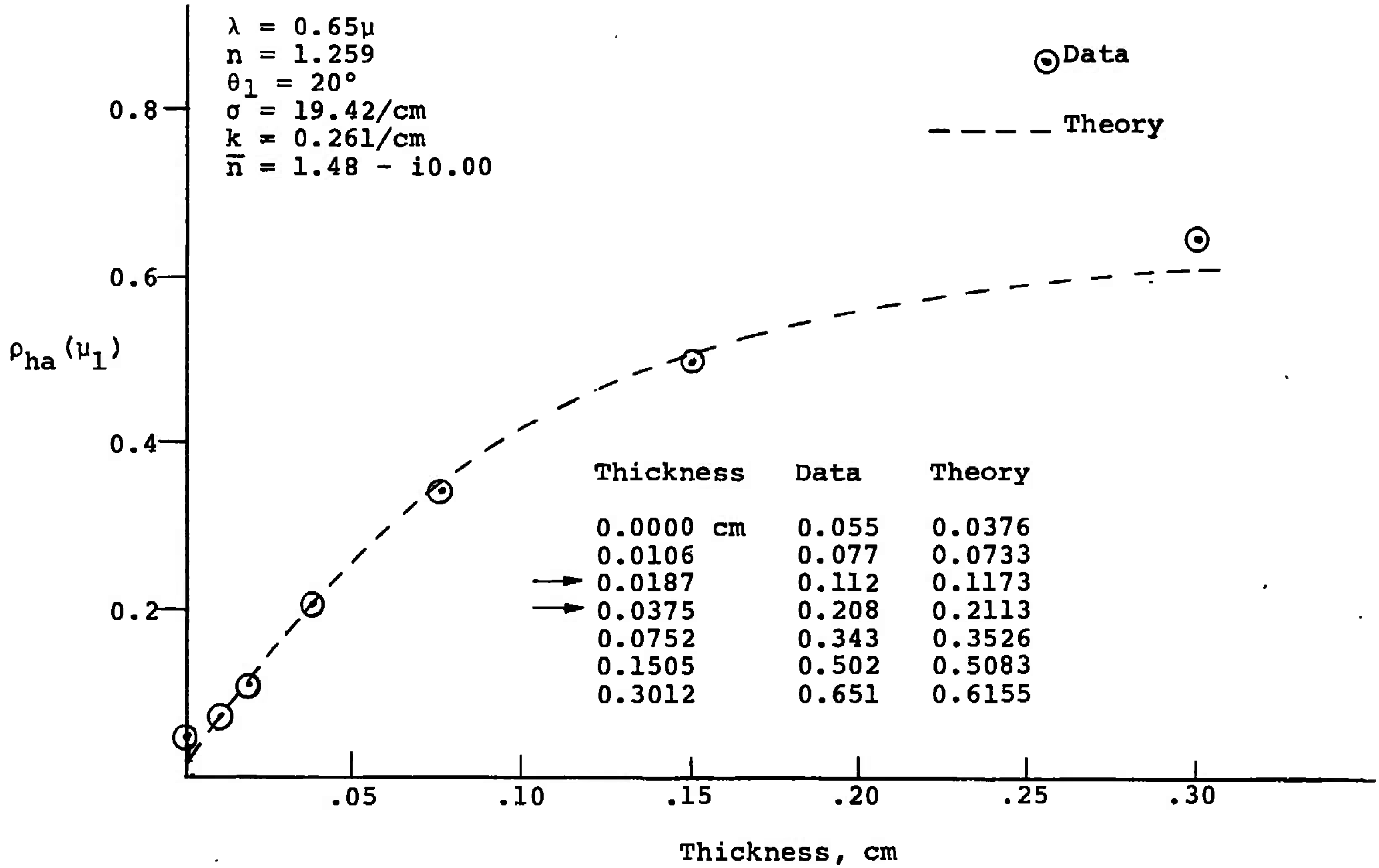

Thickness	Data	Theory
0.0000 cm	0.055	0.0376
0.0106	0.077	0.0733
→ 0.0187	0.112	0.1173
→ 0.0375	0.208	0.2113
0.0752	0.343	0.3526
0.1505	0.502	0.5083
0.3012	0.651	0.6155

Figure 52. Comparison of theory and data for a H_2O cryodeposit on a black paint substrate at $\lambda = 0.65\mu$.

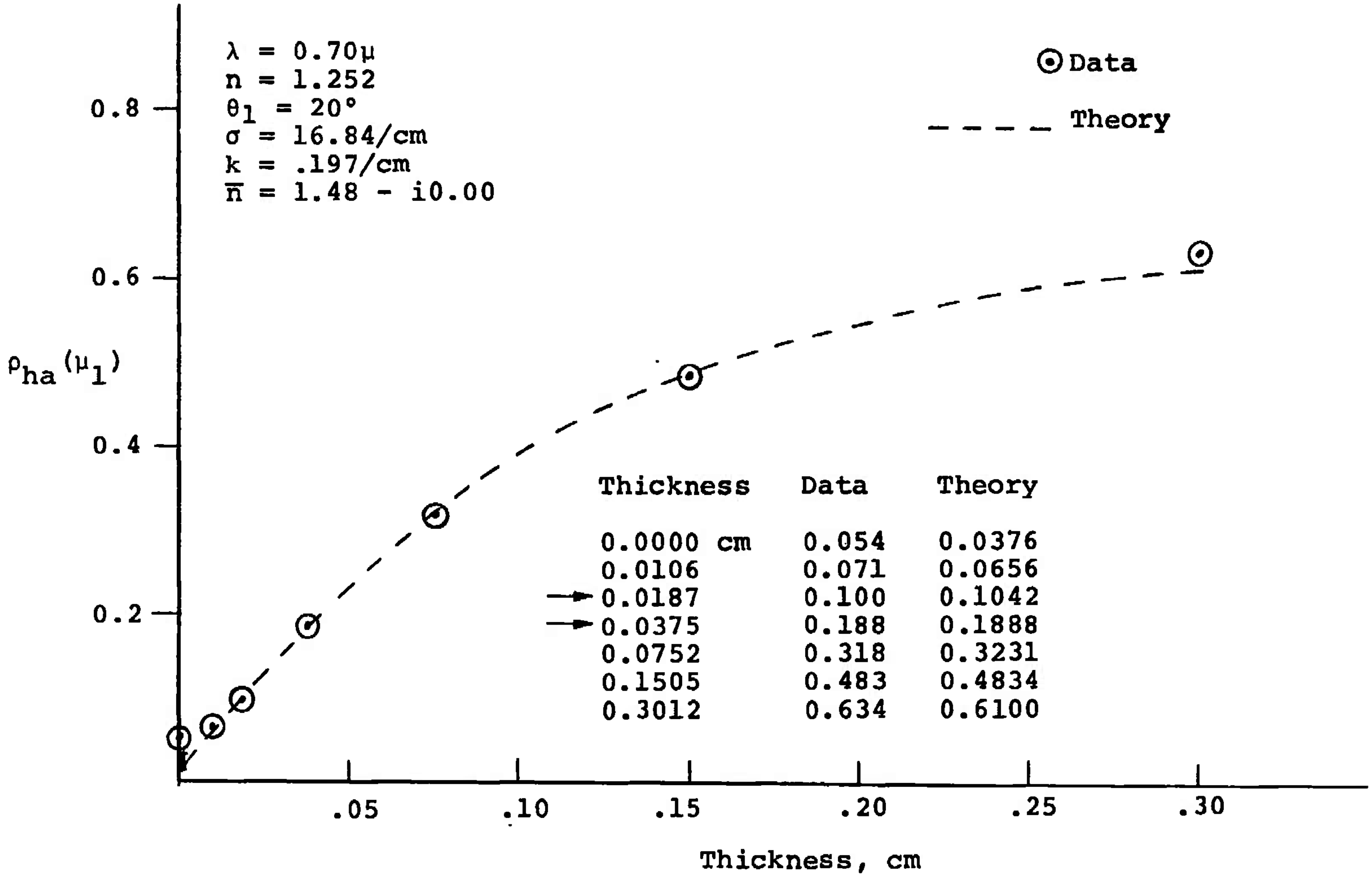

Thickness	Data	Theory
0.0000 cm	0.054	0.0376
0.0106	0.071	0.0656
→ 0.0187	0.100	0.1042
→ 0.0375	0.188	0.1888
0.0752	0.318	0.3231
0.1505	0.483	0.4834
0.3012	0.634	0.6100

Figure 53. Comparison of theory and data for a H_2O cryodeposit on a black substrate at $\lambda = 0.70\mu$.

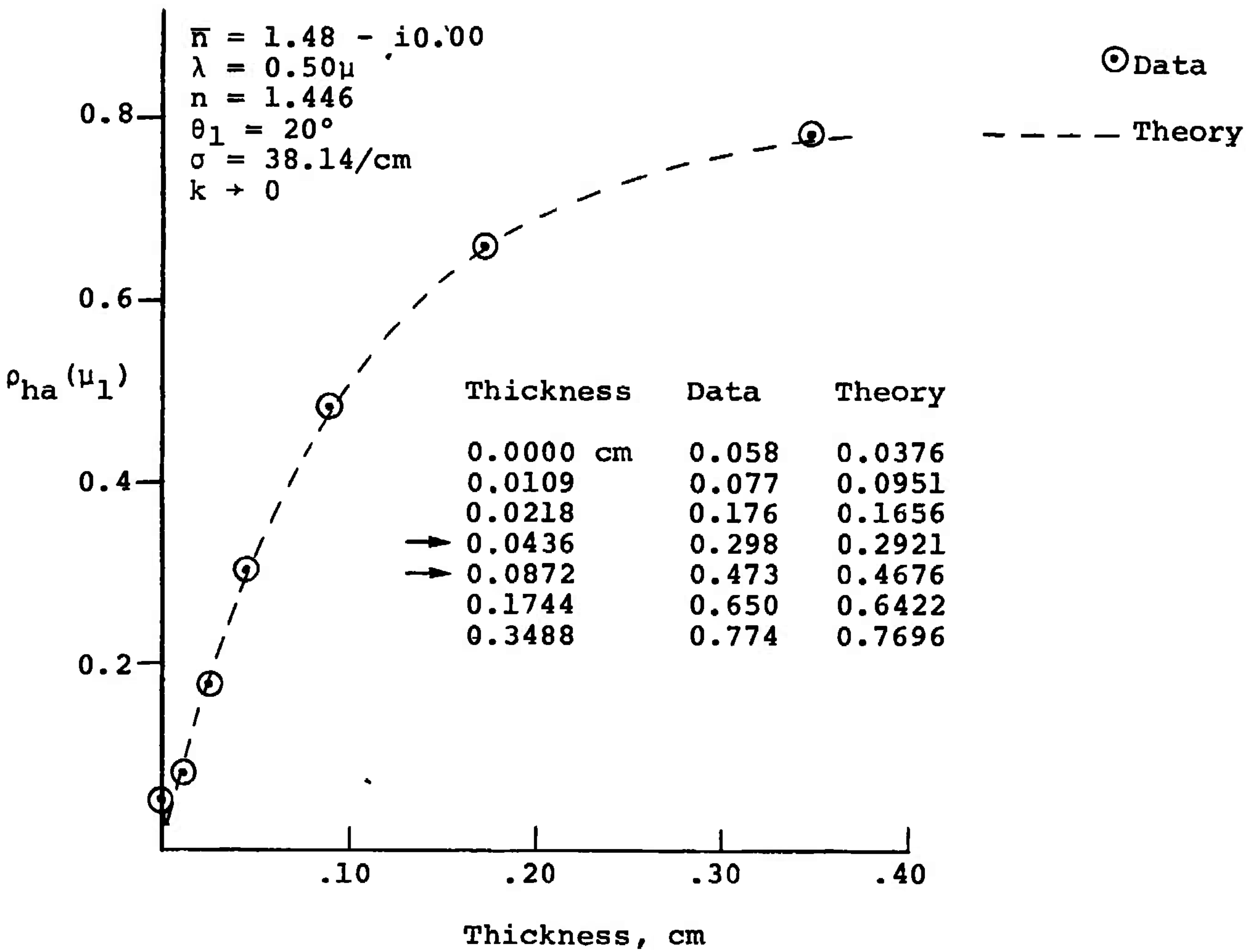

Thickness	Data	Theory
0.0000 cm	0.058	0.0376
0.0109	0.077	0.0951
0.0218	0.176	0.1656
→ 0.0436	0.298	0.2921
→ 0.0872	0.473	0.4676
0.1744	0.650	0.6422
0.3488	0.774	0.7696

Figure 54. Comparison of theory and data for a CO_2 cryodeposit on a black paint substrate at 0.50μ.

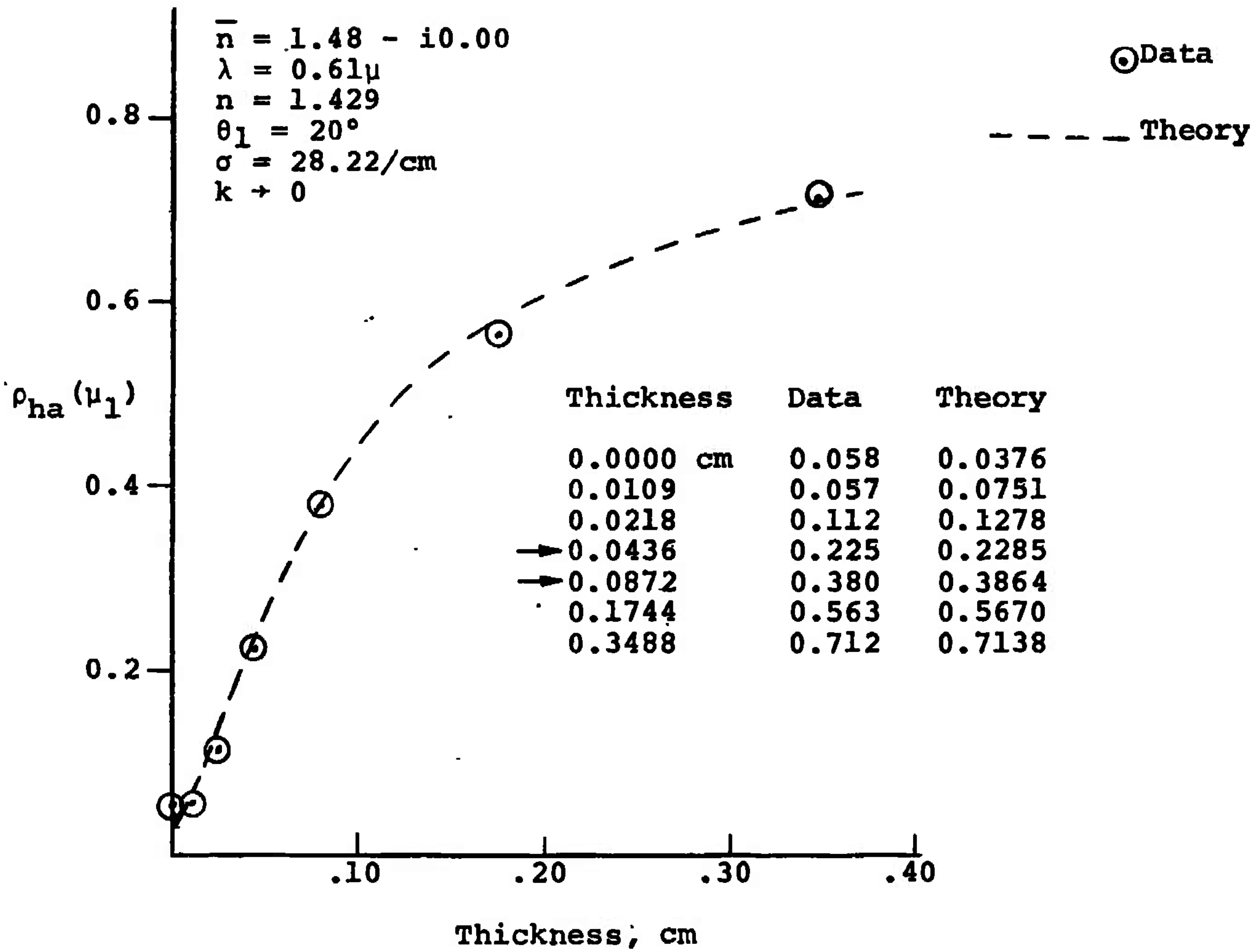

Thickness	Data	Theory
0.0000 cm	0.058	0.0376
0.0109	0.057	0.0751
0.0218	0.112	0.1278
→ 0.0436	0.225	0.2285
→ 0.0872	0.380	0.3864
0.1744	0.563	0.5670
0.3488	0.712	0.7138

Figure 55. Comparison of theory and data for a CO_2 cryodeposit on a black paint substrate at $\lambda = 0.61\mu$.

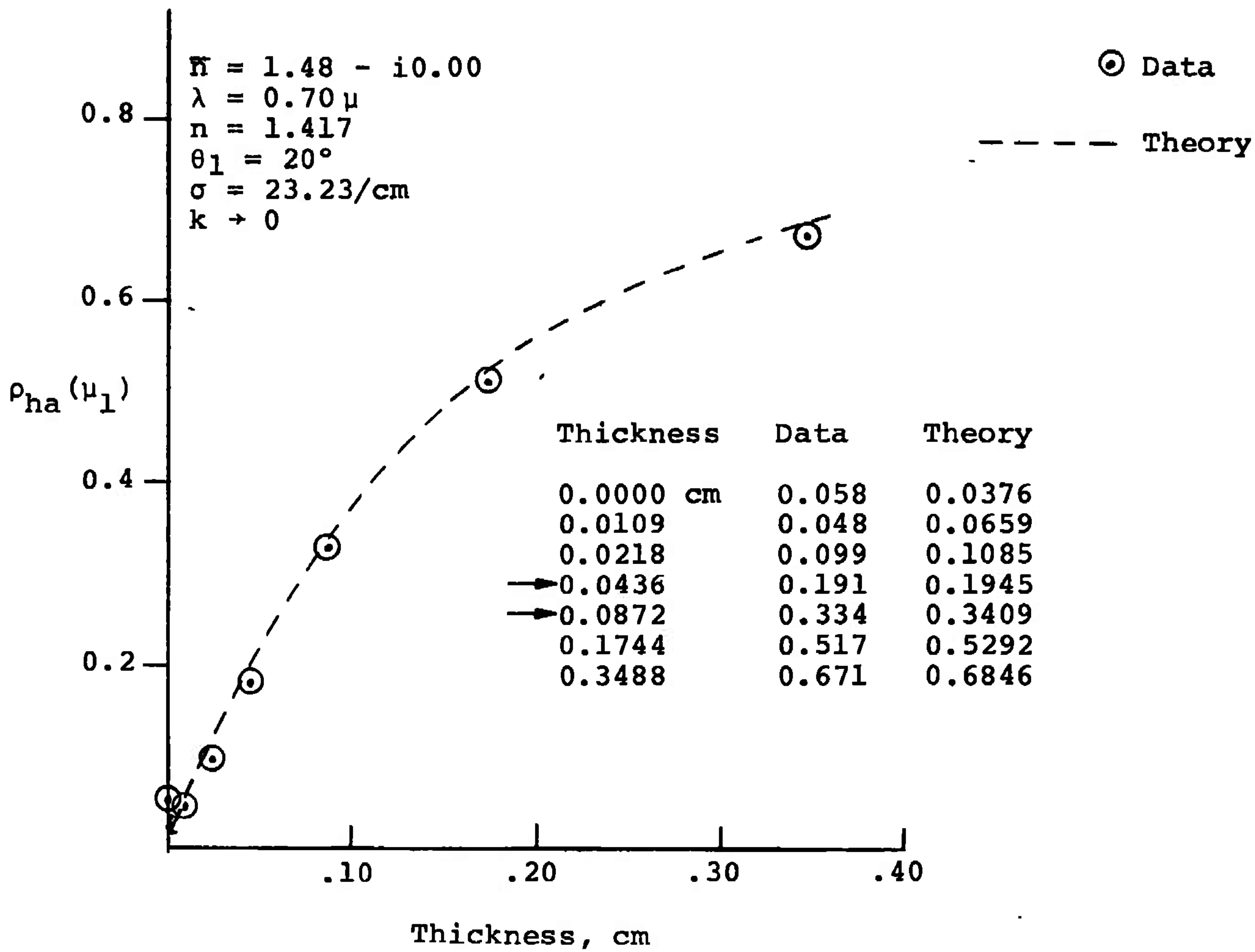

Thickness	Data	Theory
0.0000 cm	0.058	0.0376
0.0109	0.048	0.0659
0.0218	0.099	0.1085
0.0436	0.191	0.1945
0.0872	0.334	0.3409
0.1744	0.517	0.5292
0.3488	0.671	0.6846

Figure 56. Comparison of theory and data for a CO_2 cryodeposit on a black paint substrate at λ = 0.70μ.

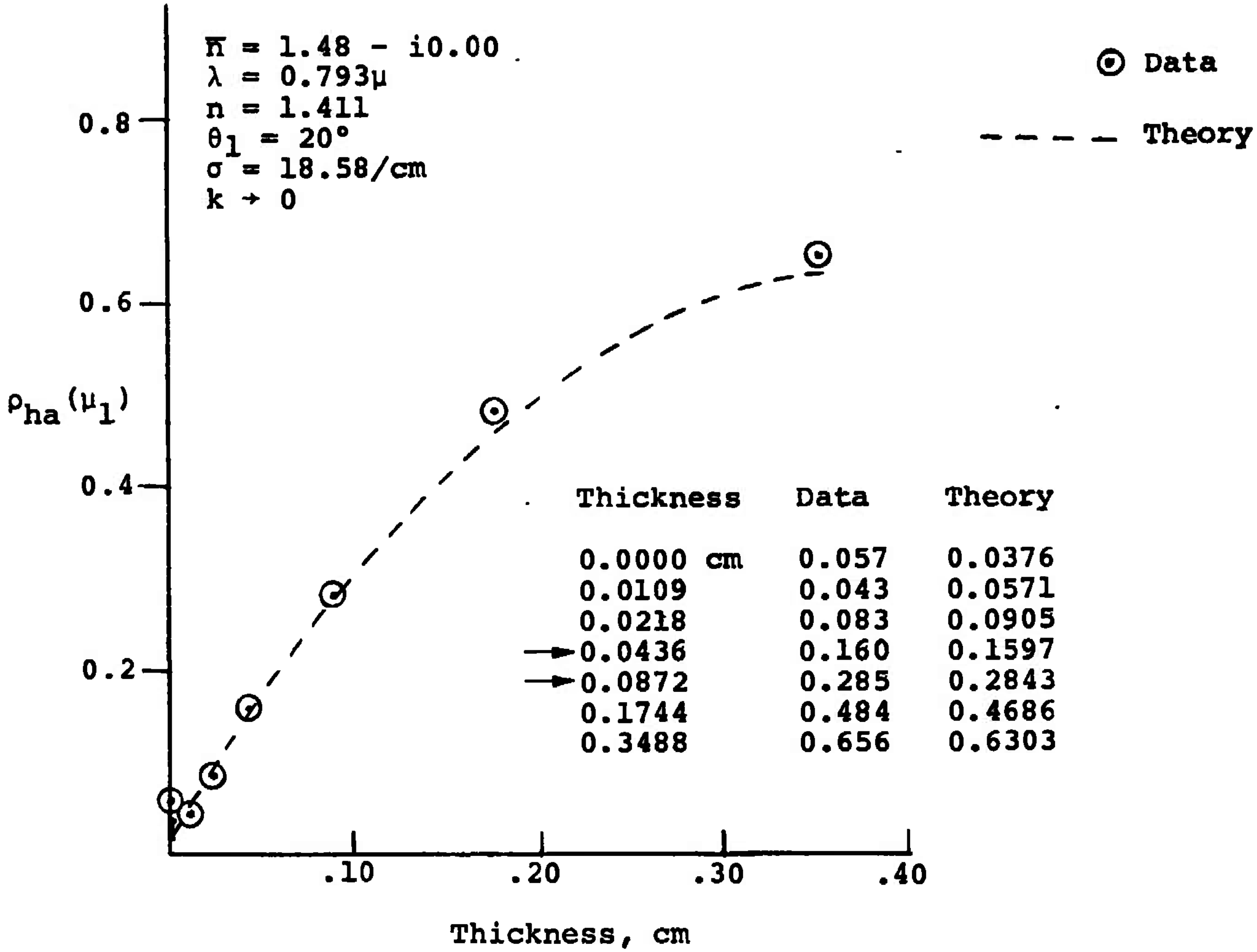

Thickness	Data	Theory
0.0000 cm	0.057	0.0376
0.0109	0.043	0.0571
0.0218	0.083	0.0905
→ 0.0436	0.160	0.1597
→ 0.0872	0.285	0.2843
0.1744	0.484	0.4686
0.3488	0.656	0.6303

Figure 57. Comparison of theory and data for a CO_2 cryodeposit on a black paint substrate at λ = 0.793μ.

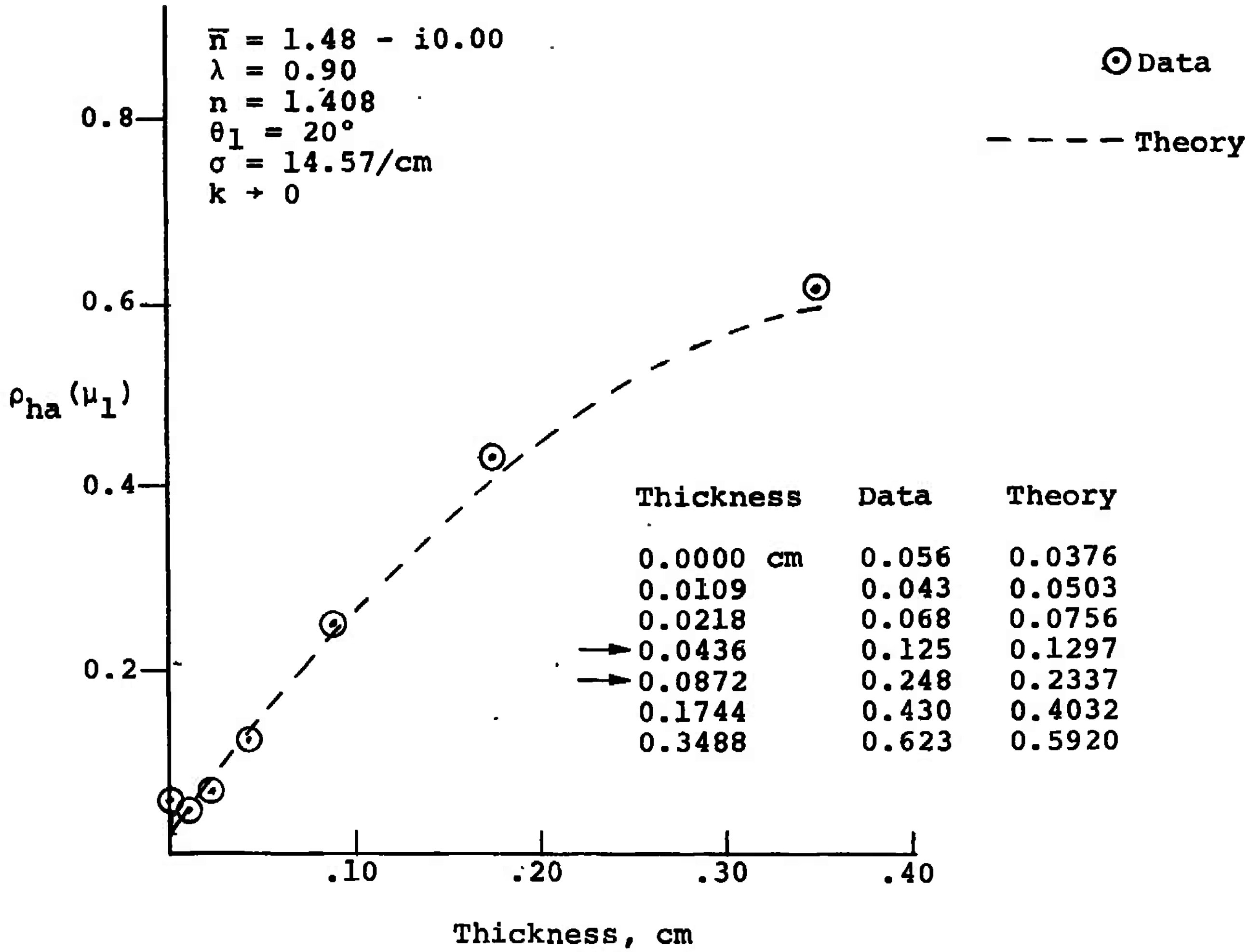

Thickness	Data	Theory
0.0000 cm	0.056	0.0376
0.0109	0.043	0.0503
0.0218	0.068	0.0756
→ 0.0436	0.125	0.1297
→ 0.0872	0.248	0.2337
0.1744	0.430	0.4032
0.3488	0.623	0.5920

Figure 58. Comparison of theory and data for a CO_2 cryodeposit on a black paint substrate at 0.90μ.

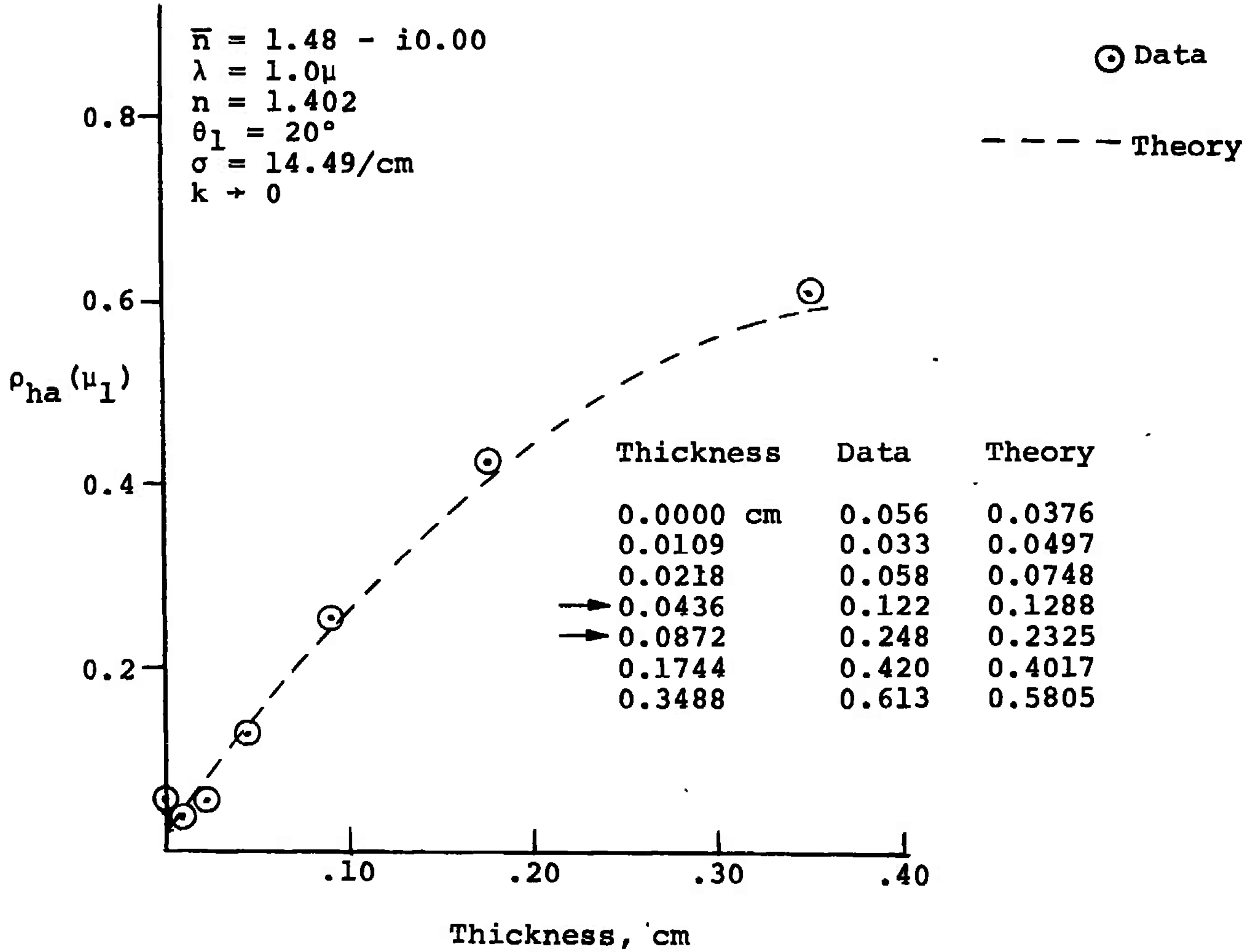

Figure 59. Comparison of theory and data for a CO_2 cryodeposit on a black paint substrate at λ = 1.0μ.

the only wavelength region where all of the necessary input data was available.

The arrows on the figures indicate the two data points which were used for $\rho^*_{ha_1}$ and $\rho^*_{ha_2}$ in Equations 99 and 100. Using the properties determined from these two data points, the reflectance at the other data points was predicted. It should be noted that the experimental data and analytical predictions are in good agreement at all thicknesses; however, the correspondence is better at small thicknesses. It is believed that the difference in theory and data for the H_2O deposits at the larger thicknesses is due to a possible structure change in the outer layers of the deposit as reported by Wood. Also most deposits encountered in the solar simulators rarely obtain a thickness greater than 0.2 cm. So even though the data and theory are less accurate at large thicknesses, there are no real consequences since practical thicknesses are not this large.

Also it should be noticed that the absorption coefficient for CO_2 is indicated as approaching zero. The values of the absorption coefficient were so low that the derivatives could no longer be accurately evaluated because the difference between $\rho_{ha}(L,\sigma^{(1)},k^{(2)})$ and $\rho_{ha}(L,\sigma^{(1)},k^{(1)})$ were on the order of 10^{-5} or less. This was found to occur when the value of the absorption coefficient was less than 0.001/cm. If, in the iteration process, the absorption coefficient was less than 0.001/cm then the computer program proceeded with the calculation taking k = 0. For the H_2O cryodeposit this difficulty did not occur.

From the experimental data it can be seen that $\rho_{ha}(\mu_1)$ decreases as the wavelength increases. Figure 60 illustrates the cause of this decrease is due to the decrease in σ with increasing wavelenghts; the value of k for both deposits is essentially constant in this range.

From the agreement between theory and data it should be evident that the analytical model proposed is realistic and that calculation of the monochromatic reflectance at a given thickness is possible to within engineering accuracy by using the properties that have been determined. This analysis can be extended to other wavelengths if the properties such as refractive indices are known. A monochromatic analysis is important because the monochromatic behavior of σ and k is required before any accurate band-model can be constructed.

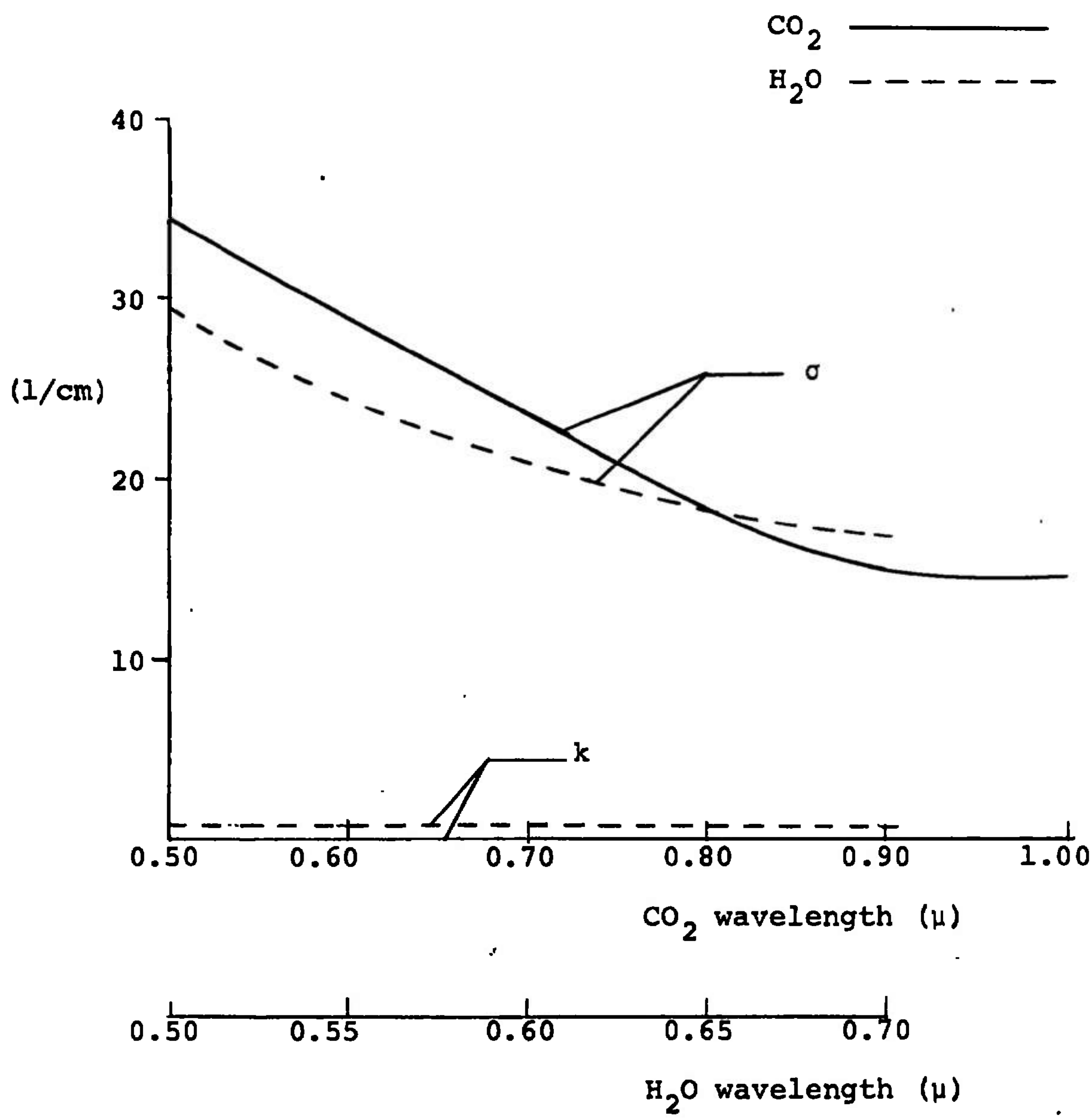

Figure 60. Variation of monochromatic absorption and scattering coefficients as a function of wavelength.

CHAPTER X

BIANGULAR REFLECTION

I. TRANSPORT EQUATION

The entire analysis presented thus far has been concerned with the hemispherical-angular reflectance. The physical basis for the hemispherical-angular reflectance is irradiating a surface diffusely and viewing the reflected intensity from fixed directions. Now an analysis of the biangular reflectance will be presented. The biangular reflectance, $\rho_{ha}(\mu_1)$, corresponds to irradiating a surface with a monodirectional flux and then viewing the surface from fixed directions to determine the angular distribution of reflected intensity.

The presence of a monodirectional flux causes several changes in the approach to the solution of the transport equation. Previously the intensity transmitted through the top interface was handled through the boundary conditions. For an incident monodirectional flux it is simpler to employ a source function within the transport equation to handle the transmitted radiation.

The representation proposed by Kourganoff [27] is to define the incident intensity, I_o, corresponding to the monodirection flux such that its integrated value gives the correct incident flux. Such an expression is

$$I_o = \frac{F_o \; \delta(\mu_1 - \mu_1^*)}{2\pi} \tag{108}$$

where $\delta(\mu_1 - \mu_1^*)$ is the Dirac "selecting" function, μ_1^* is the cosine of the incidence angle of the monodirectional flux, μ_1 corresponds to the cosine of any angle of incidence and F_o is the incident monodirectional flux normal to the projected area of the irradiated surface. The basic properties of the Dirac delta function are as indicated by [27] are

$$\delta(\mu_1 - \mu_1^*) = 0 \text{ when } \mu_1 \neq \mu_1^* \tag{109}$$

and for any integrable function $f(\xi)$

$$f(\mu_1^*) = \int_{-\infty}^{\infty} f(\xi)\,\delta(\xi - \mu_1^*)d\xi \tag{110}$$

Kourganoff [27] proposed this representation because from these properties of $\delta(\mu_1 - \mu_1^*)$ it is easy to verify that Equation 108 gives a correct description of the two main physical features of the incident radiation, that of being zero intensity for all directions other than that of μ_1^* and that of giving a flux $F_o\mu_1^*$ per unit area of the irradiated surface. The monochromatic incident flux is defined as

$$F_{in} = \int_0^{2\pi}\int_0^{1} I_o \; \mu_1 d\mu_1 d\phi \tag{111}$$

therefore

$$F_{in} = 2\pi \int_{o}^{1} \frac{F_o \delta(\mu_1 - \mu_1^*)}{2\pi} \mu_1 d\mu_1 \qquad (112)$$

$$F_{in} = F_o \mu_1^* \qquad (113)$$

thus the incident flux per unit area of the irradiated area is correct. The transport equation can now be written for isotropic scattering as:

$$\frac{dI}{d\tau} = -\frac{I}{\mu} + \frac{W}{4\pi\mu} \int_{o}^{2\pi} \int_{-1}^{1} I(\tau,\mu') d\mu' d\phi$$

$$+ \frac{W}{4\pi\mu} \int_{o}^{2\pi} \int_{-1}^{1} I_o^*(\tau,\mu^*) d\mu' d\phi \qquad (114)$$

Equation 114 contains an additional term on the right-hand side which was not present in Equation 7. The term on the left-hand side of the equation is the rate of change in intensity of a beam with distance. Those on the right respectively represent the attenuation due to absorption and scattering; the contribution, by scattering into the reference beam, from beams that have been scattered one or more times; and the new term represents the scatter into the reference beam out of the partially attenuated incident beam. Note that $I_o^*(\tau,\mu^*)$ represents the intensity of the incident beams at any point τ within the deposit. Due to scattering and absorption the incident beams are attenuated as they transverse through the deposit and no longer have the value I_o.

In Appendix B expressions have already been derived for the value of the attenuated intensity due to both absorption and scattering. From Appendix B, substitution of Equation 172 into Equation 169 and substitution of Equation 173 into Equation 168 yields:

$$I_o^*(\tau,\mu^*) = \frac{\rho_{23}(\mu^*)[1 - \rho_{12}(\mu_1^*)]n^2 e^{-(\tau_o+\tau)/\mu^*} I_o}{[1 - \rho_{21}(\mu^*)\rho_{23}(\mu^*)e^{-2\tau_o/\mu^*}]} \tag{115}$$

$$I_o^*(\tau,-\mu^*) = \frac{[1 - \rho_{12}(\mu^*)]n^2 e^{-(\tau_o-\tau)/\mu^*} I_o}{[1 - \rho_{21}(\mu^*)\rho_{23}(\mu^*)e^{-2\tau_o/\mu^*}} \tag{116}$$

Equation 114 can now be written in the form

$$\frac{dI}{d\tau} = \frac{-I}{\mu} + \frac{W}{2\mu}\int_{-1}^{1} I(\tau,\mu')d\mu' + \frac{W}{2\mu}\int_{o}^{1} I_o^*(\tau,\mu^*)d\mu'$$

$$+ \frac{W}{2\mu}\int_{o}^{1} I_o^*(\tau,-\mu^*)d\mu' \tag{117}$$

where $I_o^*(\tau,\mu^*)$ and $I_o^*(\tau,-\mu^*)$ are given by Equation 115 and Equation 116 respectively. The expression I_o in Equations 115 and 116 is given by Equation 108. Substitution of Equation 108 into Equations 115 and 116 and then combining these with Equation 117 produces

$$\frac{dI}{d\tau} = \frac{-I}{\mu} + \frac{W}{2\mu} \int_{-1}^{1} I(\tau,\mu')d\mu' + [K_1(\tau,\mu_1^*) + K_2(\tau,\mu_1^*)]$$

$$\times \frac{W}{2\mu} \int_{o}^{1} I_o d\mu' \tag{118}$$

where

$$K_1(\tau,\mu_1^*) = \frac{\rho_{23}(\mu^*)[1 - \rho_{12}(\mu_1^*)]e^{-(\tau_o+\tau)/\mu^*}}{[1 - \rho_{21}(\mu^*)\rho_{23}(\mu^*)e^{-2\tau_o/\mu^*}]} \tag{119}$$

$$K_2(\tau,\mu_1^*) = \frac{[1 - \rho_{12}(\mu_1^*)]e^{-(\tau_o-\tau)/\mu^*}}{[1 - \rho_{21}(\mu^*)\rho_{23}(\mu^*)e^{-2\tau_o/\mu^*}]} \tag{120}$$

In order to simplify Equation 118, let the integral in the last term be evaluated, therefore

$$\int_{o}^{1} I_o d\mu = \int_{o}^{1} F_o \frac{\delta(\mu_1 - \mu_1^*)}{2\pi} d\mu \tag{121}$$

and recalling Snell's law

$$\mu_1 = [1 - n^2(1 - \mu^2)]^{1/2} \tag{122}$$

the differential $d\mu$ becomes

$$d\mu = \left(\frac{\mu_1}{\mu}\right) \frac{d\mu_1}{n^2} \tag{123}$$

Substitution of Equation 123 into Equation 121 gives

$$\int_0^1 I_o d\mu = \int_0^1 \frac{F_o \;\delta(\mu_1 - \mu_1^*)}{2\pi} \left(\frac{\mu_1}{\mu}\right) \frac{d\mu_1}{n^2} \tag{124}$$

and by Equation 109, the integral becomes

$$\int_0^1 I_o d\mu = \frac{F_o}{2\pi n^2} \left(\frac{\mu_1^*}{\mu^*}\right) \tag{125}$$

Incorporating Equation 125 into the transport equation, Equation 118, yields the result

$$\mu\frac{dI}{d\tau} = -I + \frac{W}{2} \int_{-1}^{1} I(\tau,\mu')d\mu' + \{K_1(\tau,\mu^*) + K_2(\tau,\mu^*)\}$$

$$\times \frac{WF_o}{4\pi} \left(\frac{\mu_1^*}{\mu^*}\right) \tag{126}$$

The next step is to multiply both sides by π/F_{in} and define

$$i(\tau,\mu) = \frac{\pi \; I(\tau,\mu)}{F_{in}} \tag{127}$$

which yields

$$\frac{di}{d\tau} = \frac{-i}{\mu} + \frac{W}{2\mu} \int_{-1}^{1} i(\tau,\mu')d\mu' + \frac{W}{4\mu}$$

$$\times \{K_1(\tau,\mu^*) + K_2(\tau,\mu^*)\} \left(\frac{1}{\mu^*}\right) \tag{128}$$

Since simplification of the source term has been accomplished, Equation 128 can be transformed into a system of differential equation by use of Equation 23 for the integral term, thus giving

$$\frac{di}{d\tau}(\tau,\mu_\ell) = \frac{-i(\tau,\mu_\ell)}{\mu_\ell} + \frac{W}{2\mu_\ell}\sum_{j=1}^{p} i(\tau,\mu_j)a_j + \frac{W}{2\mu_\ell}$$

$$\times \{K_1(\tau,\mu^*) + K_2(\tau,\mu^*\} \left(\frac{1}{\mu^*}\right) \qquad (129)$$

The numerical solution of Equation 129 proceeds the same as indicated in Chapter IV. The same initial guess criteria as presented in Chapter VII was successfully employed. If Equation 129 is solved by the eigenvalue approach then a particular solution is found by assuming $Ce^{-\tau/\mu^*}$ for the solution of the non-homogeneous equation, where C is a constant.

Since model one has already been chosen, Equation 129 was only solved for case one. The transmitted flux has been used as a source term in the transport equation so the boundary conditions must not involve transmission through the top surface. The normalized boundary conditions become

$$i(\tau_o,-\mu_\ell) = \rho_{21}(\mu_\ell)\ i(\tau_o,\mu_\ell) \qquad (130)$$

$$i(0,\mu_\ell) = \rho_{23}(\mu_\ell)\ i(0,-\mu_\ell) \qquad (131)$$

$$\ell = 1, \ldots, p/2$$

In Chapter II the definition of biangular reflectance was presented; mathematically expressed this definition becomes

$$\rho_{ba}(\mu_1) = \frac{\pi I_r}{F_{in}} \tag{132}$$

where I_r is the reflected intensity

$$I_r = \rho_{12}(\mu_1^*)I_o + [1 - \rho_{21}(\mu^*)]I_o^*(\tau_o,\mu^*)$$

$$+ \frac{[1 - \rho_{21}(\mu)]}{n^2} I(\tau_o,\mu) \tag{133}$$

Substitution of Equation 133 into Equation 132 along with the expressions for I_o and $I_o^*(\tau_o,\mu^*)$ yields

$$\rho_{ba}(\mu_1) = \frac{\delta(\mu_1 - \mu_1^*)}{2} \left(\rho_{12}(\mu_1^*) + \frac{[1 - \rho_{21}(\mu^*)][1 - \rho_{12}(\mu_1^*)]\rho_{23}(\mu^*)n^2e^{-2\tau_o/\mu^*}}{[1 - \rho_{21}(\mu^*)\rho_{23}(\mu^*)e^{-2\tau_o/\mu^*}]}\right)$$

$$+ \frac{[1 - \rho_{21}(\mu)]}{n^2} i(\tau_o,\mu) \tag{134}$$

The first term only appears when the specular angle is viewed, the last term is the diffuse term and has a contribution in all directions μ_1, where μ and μ_1 are related by Snell's law. Now by definition let

$$\rho_{ba}^{d}(\mu_1) = \frac{[1 - \rho_{21}(\mu)]}{n^2}\, i(\tau_o,\mu) \tag{135}$$

be the diffuse component of the biangular reflectance.

It can be shown that for a bare substrate the hemispherical-angular and the angular-hemispherical reflectances are equal. Considering a bare specular substrate, the hemispherical-angular reflectance in direction μ_1^* is given by

$$\rho_{ha}(\mu_1^*) = \rho_{13}(\mu_1^*) \tag{136}$$

The angular-hemispherical reflectance is defined by Hottel [34] as

$$\rho_{ah}(\mu_1^*) = \frac{1}{F_{in}} \int_o^{2\pi} \int_o^{1} I_r \mu_1 d\mu_1 d\phi \tag{137}$$

For a monodirectional incident flux the reflected intensity is $I_r = \rho_{13}(\mu_1) I_o$, therefore

$$\rho_{ah}(\mu_1^*) = \frac{1}{F_{in}} \int_o^{2\pi} \int_o^{1} \rho_{13}(\mu_1) \frac{F_o \delta(\mu_1 - \mu_1^*)}{2\pi}\, \mu_1 d\mu_1 d\phi$$

$$\rho_{ah}(\mu_1^*) = \rho_{13}(\mu_1^*)$$

hence

$$\rho_{ah}(\mu_1^*) = \rho_{ha}(\mu_1^*) \tag{138}$$

This proves that the angular-hemispherical and hemispherical-angular reflectances are reciprocal for the bare specular substrate. Now the validity of this reciprocal correspondence will be investigated for the case of the substrate covered by an absorbing, scattering film. No conclusive proof can be given since the results are in the form of numerical values and not closed form functions. The conclusion will be based upon comparison of numerical calculations of $\rho_{ha}(\mu_1)$ and $\rho_{ah}(\mu_1)$. From the expressions already presented it can easily be shown that Equation 138 is valid for $W = 0$.

The derivation of an expression for $\rho_{ah}(\mu_1)$ will now be developed in terms of the biangular reflection. Substitution of Equation 133 into Equation 137 yields

$$\rho_{ah}(\mu_1^*) = \rho_{12}(\mu_1^*)$$

$$+ \frac{\rho_{23}(\mu_1^*)[1 - \rho_{12}(\mu_1^*)][1 - \rho_{21}(\mu^*)]e^{-2\tau_o/\mu^*}}{[1 - \rho_{21}(\mu^*)\rho_{23}(\mu^*)e^{-2\tau_o/\mu^*}]}$$

$$+ \int_0^1 \rho_{ba}^d(\bar{\mu}_1)d\bar{\mu}_1 \qquad (139)$$

where $\bar{\mu}_1 = \sin^2 \theta_1$. The integral term in Equation 139 comes directly from Equation 135 and the integration is performed numerically by using the same order quadrature as employed in Equation 129.

II. BIANGULAR RESULTS

Illustrated in Figure 61 is a plot of the diffuse component of the biangular reflectance versus $\sin^2 \theta_1$. The area under the curve represents the integral term in Equation 139. This diffuse component is due to the internal scattering within the deposit. The incident flux was chosen as normally incident because axial symmetry has been assumed within the deposit. For a diffusely irradiated surface the assumption of axial symmetry is valid. However, for a monodirectional incident flux axial symmetry is probably not physically realistic except for small angles of incidence ($\mu_1^* \simeq 1$). Table III indicates a comparison of the calculated hemispherical-angular and angular hemispherical reflectances for various substrates and for various orders of quadrature. The numerical agreement indicates that reciprocity appears to be reasonable even though there is no rigorous proof available. It should be noticed that the numerical solution was successfully employed for the system of 40 simultaneous equations. The highest order eigenvalue approach, observed in the literature by this author, was 24. Also the change of the order of quadrature does not appear to have a large effect on $\rho_{ah}(\mu_1)$.

Experimental biangular data has been presented by Müller [5]. It was attempted to achieve a correspondence between the data and the theory by using the properties determined in Chapter IX. The data in [5] is not a measure

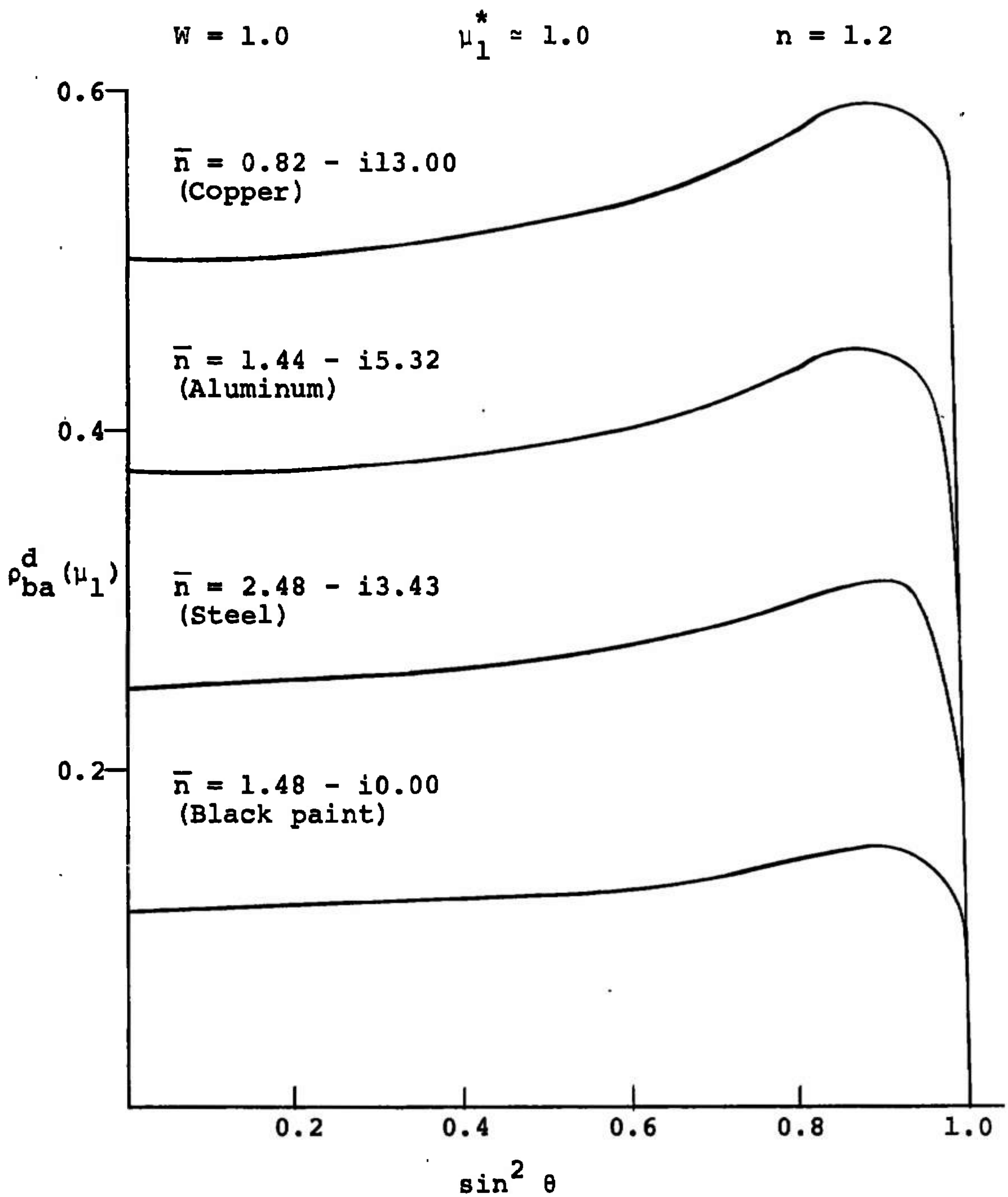

Figure 61. Biangular reflectance distribution for a case 1 deposit.

TABLE III

COMPARISON OF HEMISPHERICAL-ANGULAR AND ANGULAR-HEMISPHERICAL REFLECTANCE FOR VARIOUS ORDERS OF QUADRATURE AT n = 1.2, W = 1.0, AND $\mu_1^* = 0.999$

Substrate	τ_o	50 Steps 10 Point Quadrature+	50 Steps 10 Point Quadrature−	50 Steps 10 Point Quadrature−	50 Steps 10 Point Quadrature−
Black Paint n = 1.48 - i0.00	0.5	.1563	.1563	.1496	.1547
Steel n = 2.48 - i3.43	0.5	.5005	.4906	.4902	.5023
Aluminum n = 1.44 - i5.32	0.5	.7438	.7357	.7220	.7360
Copper n = 0.82 - i13.00	0.5	.9610	.9507	.9412	.9598

+Hemispherical-angular reflectance.

−Angular-hemispherical reflectance.

of the absolute value of biangular reflectance but rather only indicates the angular dependence of the biangular reflectance. The data presented in [5] is given as the ratio of the detector output at any viewing angle with a deposit present to the detector output of the bare substrate in the specular direction. The detector output is proportional to the power incident on the detector. It is necessary to have expressions which correspond to the detector outputs with and without the deposits. It can be shown, as in Appendix C, that the ratio of detector outputs is given by

$$\frac{P_{D2}}{P_{D1}} = \frac{dA_i}{\pi r^2} \frac{\rho_{ba}^{d}(\mu_1)\mu_1}{\rho_{13}(\mu_1^*)} \tag{140}$$

The magnitude of the ratio of the detector output could not be accurately determined, so it was decided to investigate the general trend of the reflectance data with respect to viewing angle. Since the incidence angle is required to be small, as indicated earlier, the data at an angle of incidence of 0 degrees, $\lambda = 0.9\mu$ and $L = 300\mu$ was used. The radiative properties for the CO_2 deposit at this wavelength were taken from Figure 58, page 161. The magnitude in the normal direction was adjusted such that Equation 140 and the data were identical at this point. This is equivalent to picking the constant $dA_i/\pi r^2 \rho_{13}(\mu_1^*)$ to give the correct detector output ratio in the normal direction.

The angular dependence of the data and theory are indicated in Figure 62. The distributions of both the data and theory for the near normal incident flux correspond closely to a cosine profile which implies that even though the substrate is specular and the interfaces reflect and transmit specularly, the internal scattering causes an essentially diffuse biangular reflection. The comparison of theory and data for the larger incidence angles of the collimated incident flux shows that the assumption of axially symmetric radiative transport is not very accurate. Thus one should be careful in assuming axial symmetry for a collimated flux incident at angles that are not near zero.

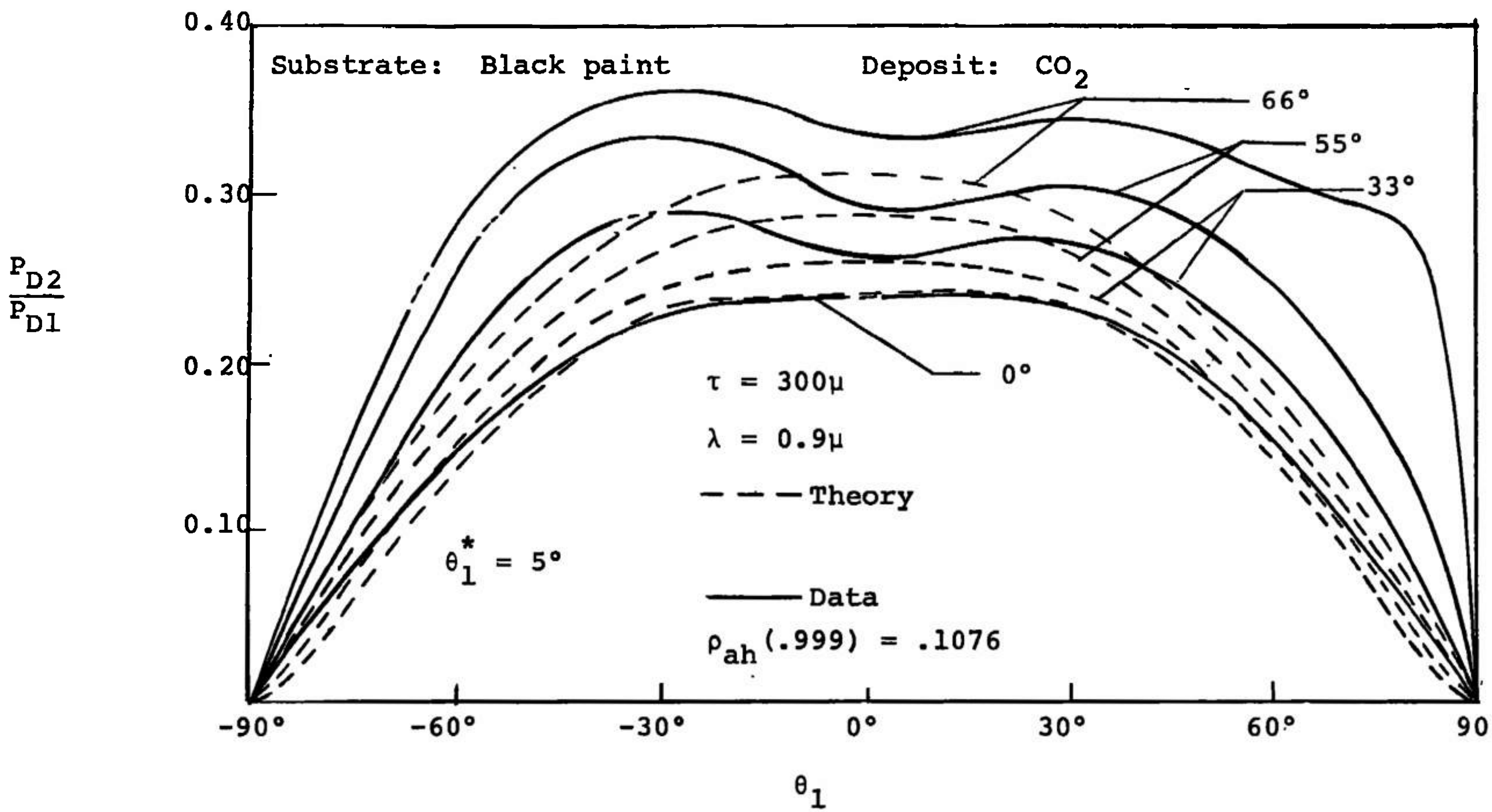

Figure 62. Comparison of theory and data for biangular results.

CHAPTER XI

SUMMARY AND CONCLUSIONS

An analysis has been presented for the radiative characteristics of non-emitting coatings or deposits. Absorbing and isotropically scattering media were considered for several types of boundary conditions with either diffuse or collimated radiation incident flux. The theoretical results correspond to either a monochromatic or gray analysis. Comparison of analytic results and experimental data for cryodeposits was presented on a monochromatic basis. The wavelength span was restricted to a visible region where all of the necessary input data was available.

To summarize, the reflectances of cryodeposits are of interest in general with regard to:

1. studies of thermal radiative properties of cryogenically cooled simulation chamber surroundings,
2. any experiment apparatus requiring cryogenically cooled mirrors, windows or lenses,
3. studies involving planetary frosts,
4. and the effects of thin deposits formed on low temperature black bodies which are used as calibration standards.

Also with the realization that a hydrogen-oxygen fueled space shuttle should be operational before the end of the decade, the possibility of water frost contamination forming on space stations or satellites is increased since the formation of H_2O is a combustion product.

As a result of this study some general conclusions are:

1. The effect of a thin film ($\tau_o = 0$) is significant and causes an immediate hemispherical-angular reflectance decrease due to the relative refractive index change. The magnitude of the reflectance decrease depends on the substrate reflectance.
2. For large optical thicknesses, the hemispherical-angular reflectance was found to increase if W is large and to decrease if W is small. For intermediate W values the reflectance may either increase or decrease depending on the substrate reflectance.
3. The hemispherical-angular reflectance is generally lower for a medium bounded by diffuse surfaces than in one bounded by specular surfaces. Physically this corresponds to rough interfaces having lower reflectances than smooth interfaces.
4. For a given vacuum-interface model, the hemispherical-angular reflectance dependence on the angular nature of the substrate diminishes as the optical thickness increases.
5. The best analytical model for CO_2 and H_2O

cryodeposits was found to be the specular reflector and transmitter. In the visible wavelength region both CO_2 and H_2O cryodeposits correspond to high albedo values and the hemispherical-angular reflectance increases with increasing viewing angles.

6. The reflectance of a highly scattering media ($W \approx 1$) may not necessarily be a monotonic function of thickness. In some instances the reflectance may decrease and then increase with increasing optical thickness due to the critical angle effect.
7. The monochromatic absorption and scattering coefficients were determined in the visible wavelength region and were shown to be useful in accurately predicting the hemispherical-angular reflectance at many thicknesses.
8. The comparison of theory and data for the biangular results showed good agreement for the normal incident collimated flux. The axisymmetric assumption appeared not to be valid for non-normal incident fluxes.
9. The diffuse portion of the biangular reflectance for a case 1 deposit was shown to be approximately a cosine distribution. This means even for specular (Fresnel) vacuum-deposit and substrate-deposit interfaces bounding an isotropically

scattering medium, the intensity reflected in the non-specular directions is diffusely distributed.

BIBLIOGRAPHY

BIBLIOGRAPHY

1. Mills, D. W., and A. M. Smith. "Effect of Reflections from CO_2 Cryopanel Deposits on the Thermal Balance of a Test Model in a Space Simulation Chamber," Journal of Spacecraft and Rockets, 7:374-376, March, 1970.

2. McCullough, B. A., B. E. Wood, and J. P. Dawson. "Thermal Radiative Properties of Carbon Dioxide Cryodeposits from 0.5 to 1.1 Microns," Arnold Engineering Development Center TR-65-94, Arnold Air Force Station, Tennessee, August, 1965.

3. Wood, B. E., B. A. McCullough, and J. P. Dawson. "Vacuum Integrating Spheres for Measuring Cryodeposit Reflectances from 0.35 to 15.0 Microns," Arnold Engineering Development Center TR-65-178, Arnold Air Force Station, Tennessee, August, 1965.

4. McCullough, B. A., B. E. Wood, and A. M. Smith. "A Vacuum Integrating Sphere for In Situ Reflectance Measurements at 77 °K from 0.5 to 10 Microns," Arnold Engineering Development Center TR-67-10, Arnold Air Force Station, Tennessee, April, 1967.

5. Müller, P. R. "Measurements of Refractive Index, Density, and Reflected Light Distributions for Carbon Dioxide and Water Cryodeposits and Also Roughened Glass Surfaces." Ph.D. dissertation, The University of Tennessee, Knoxville, June, 1969.

6. Francis, J. E., and T. J. Love. "Radiant Heat Transfer Analysis of Isothermal Diathermanous Coatings on a Conductor," AIAA Journal, 4:643-649, April, 1966.

7. Love, T. J. Radiative Heat Transfer. Columbus, Ohio: Charles E. Merrill Publishing Company, Inc., 1968.

8. Pepper, S. V. "Absorption of Infrared Radiation by Ice Cryodeposits," NASA Technical Note TN D-518, April, 1969.

9. Hsia, H. M., and T. J. Love. "Radiation Heat Transfer between Parallel Plates Separated by a Nonisothermal Medium with Anisotropic Scattering," Journal of Heat Transfer, C89:197-203, August, 1967.

10. Hottel, H. C., A. F. Sarofim, and I. A. Vasolos. "Radiative Transfer in Anisotropically Scattering Media: Allowance for Fresnel Reflection at the Boundaries," Journal of Heat Transfer, C90:56-62, February, 1968.

11. Merriam, R. L. "A Study of Radiative Characteristics of Condensed Gas Deposits on Cold Surfaces." Ph.D. dissertation, Purdue University, June, 1968.

12. Faddeeva, V. N. Computational Methods of Linear Algebra. New York: Dover Publications, Inc., 1959.

13. Wolf, P. "An Analytical and Experimental Study of the Radiation Heat Transfer in Scattering, Absorbing, and Emitting Media." Ph.D. dissertation, The University of Tennessee, Knoxville, December, 1968.

14. Wood, B. E., A. M. Smith, and B. A. Seiber. "Variation of H_2O and CO_2 Cryodeposit Reflectances with Angle of Incidence and Deposit Thickness," Arnold Engineering Development Center TR-68-144, Arnold Air Force Station, Tennessee, September, 1968.

15. Brown, T. R. "Laser Investigation of Physically Absorbed Gaseous Cryodeposits." Ph.D. dissertation, Purdue University, August, 1968.

16. Chandrasekhar, S. Radiative Transfer. New York: Dover Publications, Inc., 1960.

17. Sparrow, E. M., and R. D. Cess. Radiation Heat Transfer. Belmont, California: Brooks/Cole Publishing Company, 1966.

18. Abramowitz, M., and I. A. Stegum (editors). Handbook of Mathematical Functions. National Bureau of Standards, United States Department of Commerce. Washington: Government Printing Office, 1967.

19. Love, T. J. "An Investigation of Radiant Heat Transfer in Absorbing, Emitting and Scattering Media," Aeronautical Research Laboratories, ARL 63-3, Office of Aerospace Research, United States Air Force, January, 1963.

20. Tenenbaum, M., and H. Pollard. Ordinary Differential Equations. New York: Harper and Row, Publishers, 1963.

21. Scarborough, J. B. Numerical Mathematical Analysis. Fifth edition. Baltimore: The John Hopkins Press, 1962.

22. Cunningham, T. M., and R. L. Young. "The Absorptance of Water Cryodeposits at 77 °K for 350 °K Radiation," Arnold Engineering Development Center TDR-63-155, Arnold Air Force Station, Tennessee, August, 1963.

23. Caren, R. P., A. S. Gilcrest, C. A. Zierman, W. F. Schmidt, and J. P. Millard. "Experimental and Analytical Investigation of the Effect of Cryodeposits on the Radiation Properties of Plain and Extended Surfaces," Arnold Engineering Development Center TR-63-270, Arnold Air Force Station, Tennessee, December, 1963.

24. Cunningham, T. M., and R. L. Young. "Radiative Properties of Carbon Dioxide Cryodeposits at 77 °K," Arnold Engineering Development Center TDR-62-165, Arnold Air Force Station, Tennessee, December, 1962.

25. Jenkins, F. A., and H. E. White. Fundamentals in Optics. Third edition. New York: McGraw-Hill Book Company, Inc., 1957.

26. Hodgman, C. D., R. C. Weast, and S. M. Selby (editors). Handbook of Chemistry and Physics. 40th edition. Cleveland, Ohio: Chemical Rubber Publishing Co., 1958.

27. Kourganoff, J. Basic Methods in Heat Transfer Problems. New York: Dover Publications, Inc., 1964.

28. Harrick, N. J. Internal Reflection Spectroscopy. New York: Interscience Publishers a division of John Wiley and Sons, 1967.

29. Hottel, H. C., and A. F. Sarofim. Radiative Transfer. New York: McGraw-Hill Book Co., 1967.

APPENDIXES

APPENDIX A

The interfaces are assumed to be perfectly smooth surfaces and also to reflect specularly according to Fresnel's law. For the vacuum-deposit interface, all radiation striking the surface at an angle equal to or greater than the critical angle will be totally internally reflected. The concept of critical angle is only applied when speaking of rays striking the surface from within the optically denser medium. The portion of unpolarized radiation that is reflected at the vacuum-deposit interface is given by the following adaption of Fresnel's law from [28]:

$$\rho_{yz}(\mu_1) = \frac{1}{2}\left(\frac{\sin^2(\theta - \bar{\theta}')}{\sin^2(\theta + \bar{\theta}')}\right) + \frac{1}{2}\left(\frac{\tan^2(\theta - \bar{\theta}')}{\tan^2(\theta + \bar{\theta}')}\right) \tag{141}$$

where θ and $\bar{\theta}'$ are the angles of reflection and refraction respectively and where $y = 1$ or 2 and $z = 1, 2,$ or 3.

Separate consideration is given to the plane polarized component with vibrations perpendicular to the plane of incidence R_s and the reflectance of the plane polarized component with vibrations parallel to the plane of incidence R_p. Therefore, Snell's law becomes

$$n_d \sin\theta = \bar{n}_m \sin\bar{\theta}' \tag{142}$$

where $\bar{n}_m$ is the complex refractive index of the conductor, $\bar{\theta}'$ is the complex angle of refraction, and n_d is the refractive index of the dielectric or deposit.

Solving Equation 142 for sin $\bar{\theta}'$ and multiplying and dividing by the complex conjugate of $\bar{n}_m = n_m - ik_m$ results in the following equation:

$$\sin \bar{\theta}' = [n_d(n_m + ik_m) \sin \theta/(n_m^2 + k_m^2)] \tag{143}$$

Noting that θ' may be written as $\bar{\theta}' = \alpha + i\beta$, the reflection function for the perpendicular component becomes

$$R_s = \left(\frac{\sin(\theta - \bar{\theta}')}{\sin(\theta + \bar{\theta}')}\right)^2 = \left(\frac{\sin(\theta - \alpha - i\beta)}{\sin(\theta + \alpha + i\beta)}\right)^2 \tag{144}$$

$$R_s = \left(\frac{\sin(\theta - \alpha)\cosh\beta - i\cos(\theta - \alpha)\sinh\beta}{\sin(\theta + \alpha)\cosh\beta + i\cos(\theta + \alpha)\sinh\beta}\right)^2 \tag{145}$$

$$R_s = \left(\frac{\sin^2(\theta - \alpha)\cosh^2\beta + \cos^2(\theta - \alpha)\sinh^2\beta}{\sin^2(\theta + \alpha)\cosh^2\beta + \cos^2(\theta + \alpha)\sinh^2\beta}\right) \tag{146}$$

$$R_s = \left(\frac{\sin^2(\theta - \alpha) + \sinh^2\beta}{\sin^2(\theta + \alpha) + \sinh^2\beta}\right) \tag{147}$$

Similarly, the parallel component can be written as

$$R_p = \left(\frac{\tan(\theta - \bar{\theta}')}{\tan(\theta + \bar{\theta}')}\right)^2 \tag{148}$$

$$R_p = R_s\left(\frac{\cos(\theta + \bar{\theta}')}{\cos(\theta - \bar{\theta}')}\right)^2 \tag{149}$$

$$R_p = \left(\frac{\cos^2(\theta + \alpha)\cosh^2\beta + \sin^2(\theta + \alpha)\sinh^2\beta}{\cos^2(\theta - \alpha)\cosh^2\beta + \sin^2(\theta - \alpha)\sinh^2\beta}\right)R_s \tag{150}$$

$$R_p = \left(\frac{\cos^2(\theta + \alpha) + \sinh^2\beta}{\cos^2(\theta - \alpha) + \sinh^2\beta}\right)R_s \tag{151}$$

or the interface hemispherical angular reflectance is

$$\rho_{yz} = .5[R_s + R_p] \tag{152}$$

More conveniently we can write Equations 147 and 151 as

$$R_s = \left[\frac{(\sin\theta\cos\alpha - \cos\theta\sin\alpha)^2 + \sinh^2\beta}{(\sin\theta\cos\alpha + \cos\theta\sin\alpha)^2 + \sinh^2\beta}\right] \tag{153}$$

and

$$R_p = \left[\frac{(\cos\theta\cos\alpha - \sin\theta\sin\alpha)^2 + \sinh^2\beta}{(\cos\theta\cos\alpha + \sin\theta\sin\alpha)^2 + \sinh^2\beta}\right] R_s \tag{154}$$

Now it is necessary to solve for $\cos\alpha$, $\sin\alpha$, and $\sinh^2\beta$ in terms of the known quantities. From Equation 143 one may write

$$\sin\overline{\theta}' = \sin(\alpha + i\beta) = \sin\alpha\cosh\beta + i\cos\alpha\sinh\beta \tag{155}$$

$$\sin\alpha\cosh\beta + i\cos\alpha\sinh\beta = \frac{n_d n_m \sin\theta + i n_d k_m \sin\theta}{n_m^2 + k_m^2} \tag{156}$$

and equating the real and imaginary parts gives:

$$\sin\alpha\cosh\beta = (n_d n_m \sin\theta)/(n_m^2 + k_m^2) \tag{157}$$

$$\cos\alpha\sinh\beta = (n_d k_m \sin\theta)/(n_m^2 + k_m^2) \tag{158}$$

Let

$$\xi = (n_d \sin \theta)/(n_m^2 + k_m^2) \tag{159}$$

therefore Equations 157 and 158 become

$$\cosh \beta = \frac{\xi n_m}{\sin \alpha} \tag{160}$$

$$\sinh \beta = \frac{\xi k_m}{\sqrt{1 - \sin^2 \alpha}} \tag{161}$$

Inserting this into the identity $\cosh^2 \beta - \sinh^2 \beta = 1$ and defining $a = (\xi n_m)^2$ and $b = (\xi k_m)^2$ gives

$$\sin \alpha = \left[\frac{1 + a + b}{2} - \sqrt{\frac{(1 + a + b)^2}{4} - a}\right]^{1/2} \tag{162}$$

and from Equations 159 and 162, $\sinh^2 \beta$ is easily computed.

In Equation 162 the constants a and b are given in terms of the knowns n_d, n_m, k_m, and θ. Equations 152, 159, 160, 161, 162 and the constants a and b can be easily programmed as a subroutine to calculate the values of $\rho_{yz}(\mu)$. In programming Equations 153 and 154 it is convenient to let $\mu = \cos \theta$ and $\sin \theta = (1 - \mu^2)^{1/2}$ since the quadrature points presented in Chapter IV correspond to discrete values.

Plots of the internal and external reflectances are shown in Figure 63 for the vacuum-deposit interface at refractive index values of the deposit of 1.2 and 1.4. These graphs show the critical angle phenomena and also

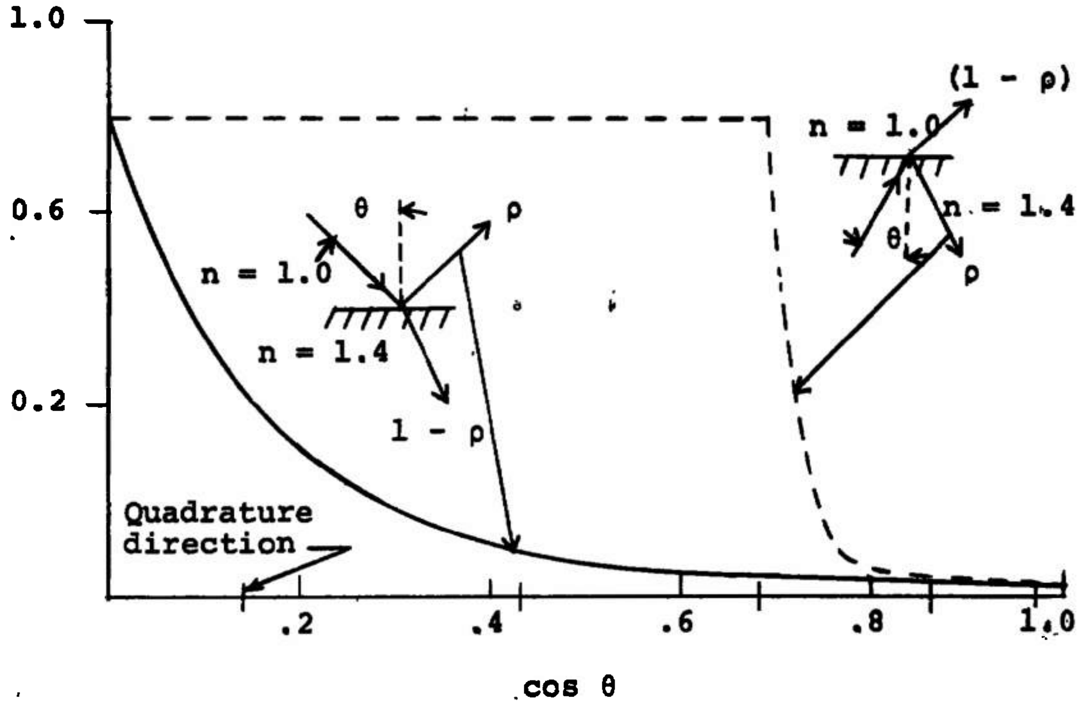

(a) n = 1.4

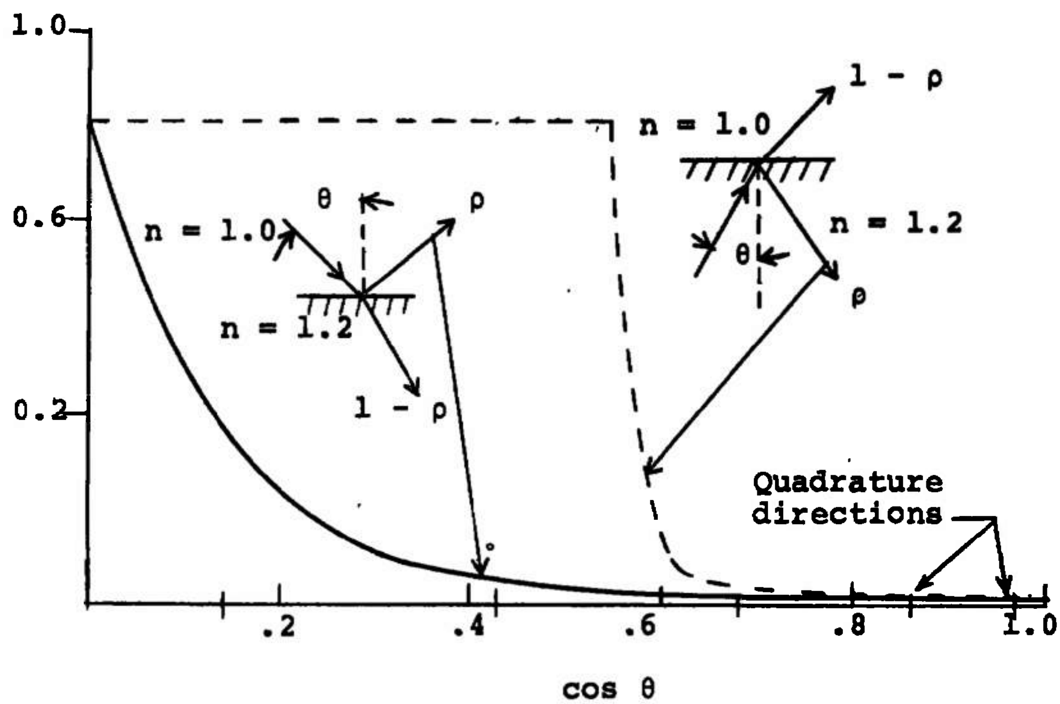

(b) n = 1.2

Figure 63. Fresnel reflectance function for n = 1.4 and n = 1.2.

reveal that the critical angle decreases as the deposit refractive index increases. Also indicated are the μ values which correspond to the discrete ordinates.

APPENDIX B

Considering the geometry in Figure 64 and assuming

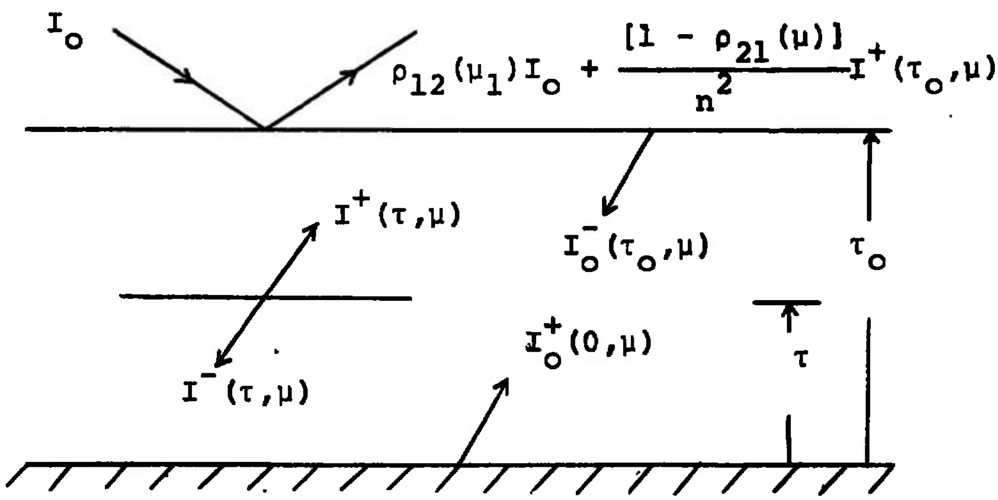

Figure 64. Deposit geometry.

only attenuation of $I^+(\tau,\mu)$ and $I^-(\tau,\mu)$ due to scattering and absorption of a non-emitting medium yields

$$I = C\ e^{-\tau/\mu} \tag{163}$$

Separating Equation 163 into two equations for the two directions gives the result

$$I^+(\tau,\mu) = C_1\ e^{-\tau/\mu} \qquad 0 < \mu \leq 1 \tag{164}$$

$$I^-(\tau,\mu) = C_2\ e^{-(\tau-\tau_o)/\mu} \qquad -1 \leq \mu < 0 \tag{165}$$

with boundary conditions at

$$\tau = 0 \qquad I^+(0,\mu) = I_o^+(0,\mu) \tag{166}$$

$$\tau = \tau_o \qquad I^-(\tau_o,\mu) = I_o^-(\tau_o,\mu) \tag{167}$$

therefore $C_1 = I_o^+(0,\mu)$ and $C_2 = I_o^-(\tau_o,\mu)$.

Now for $0 < \mu \leq 1$

$$I^+(\tau,\mu) = I_o^+(0,\mu)e^{-\tau/\mu} \tag{168}$$

$$I^-(\tau,-\mu) = I_o^-(\tau_o,-\mu)e^{-(\tau_o-\tau)/\mu} \tag{169}$$

the physical boundary conditions are

$$I_o^+(0,\mu) = \rho_{23}(\mu)I^-(0,-\mu) \tag{170}$$

$$I_o^-(\tau_o,-\mu) = \rho_{21}(\mu)I^+(\tau_o,\mu) + [1 - \rho_{12}(\mu_1)]n^2 I_o \tag{171}$$

Substitution of Equation 168 into Equation 171 and Equation 169 into Equation 170 yields

$$I_o^-(\tau_o,-\mu) = \frac{(1 - \rho_{12})I_o n^2}{[1 - \rho_{21}\rho_{23}e^{-2\tau_o/\mu}]} \tag{172}$$

$$I_o^+(0,\mu) = \frac{\rho_{23}(1 - \rho_{12})n^2 e^{-\tau_o/\mu} I_o}{[1 - \rho_{21}\rho_{23}e^{-2\tau_o/\mu}]} \tag{173}$$

The hemispherical-angular reflectance from the film is given by the reflected intensity divided by the incident intensity

$$\rho_{ha}(\mu_1) = \frac{\rho_{12}\, I_o}{I_o} + \frac{I^+(\tau_o,\mu)}{I_o}\,\frac{[1 - \rho_{21}]}{n^2} \tag{174}$$

Substitution of Equation 173 into Equation 168 and then incorporating Equation 168 into Equation 174 yields

$$\rho_{ha}(\mu_1) = \rho_{12} + \frac{\rho_{23}[1 - \rho_{21}][1 - \rho_{12}]e^{-2\tau_o/\mu}}{[1 - \rho_{21}\rho_{23}e^{-2\tau_o/\mu}]} \tag{175}$$

Now for very thin films where the optical thickness is so small that negligible attenuation can occur, ρ_{ha} becomes

$$\rho_{ha}(\mu_1)\Big|_{\tau_o \to 0} = \rho_{12} + \frac{\rho_{23}[1 - \rho_{21}][1 - \rho_{12}]}{[1 - \rho_{21}\rho_{23}]} \tag{176}$$

Thus if no film is present, the expression for ρ_{ha} of the bare substrate is

$$\rho_{ha}(\mu_1) = \rho_{13}(\mu_1) \tag{177}$$

where $\rho_{13}(\mu_1)$ is given as indicated in Appendix A. For a monolayer film of molecules absorption and scattering have not yet become prominent; thus $\rho_{ha}(\mu_1)$ is given by Equation 176. The discontinuous change in ρ_{ha} from Equation 177 to Equation 176 accounts for the first drop as shown in Figure 3, page 16. Essentially the film optical thickness is zero in both cases. However, there is a definite relative refractive index change which occurs.

The expression Equation 176 can also be shown to be the sum of the infinite series of reflections that occur at the top and bottom interfaces. Again the expressions for ρ_{23}, ρ_{12} and ρ_{21} are given as indicated in Appendix A.

APPENDIX C

As shown in Figure 65, let the area dA_j represent the

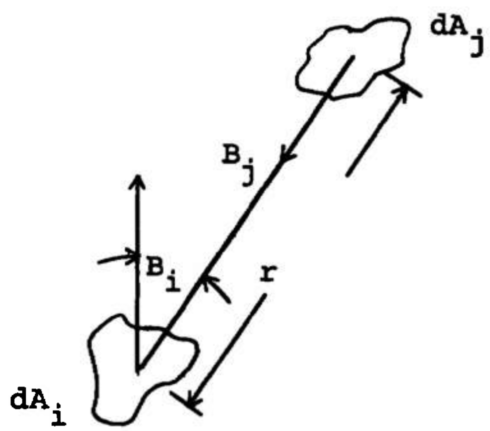

Figure 65. Geometrical arrangement of the detector and irradiated areas.

detector area and let dA_i represent the illuminated area. If dA_i is considered to be a bare specular surface, the flux incident on dA_i is

$$F_{in} = \int_0^{2\pi} \int_0^1 J_o \cos\theta \, d\omega$$

$$= 2\pi \int_0^1 \frac{F_o}{2\pi} \delta(\mu_1 - \mu_1^*) \mu_1 d\mu_1$$

$$= F_o \mu_1^*$$

The intensity reflected from dA_i is

$$I_r = \rho_{13}(\mu_1) I_o = \rho_{13}(\mu_1) \frac{F_o}{2\pi} \delta(\mu_1 - \mu_1^*)$$

and the reflected flux is

$$F_r = \int_o^{2\pi} \int_o^1 \rho_{13}(\mu_1) \frac{F_o}{2\pi} \delta(\mu_1 - \mu_1^*) \mu_1 d\mu_1 d\phi$$

$$F_r = \rho_{13}(\mu_1^*) F_{in}$$

The power leaving dA_i is $\rho_{13}(\mu_1^*) F_{in} dA_i$ and the portion of this reflected power incident on the detector is

$$P_{D1} = \frac{dA_j}{dA_i} \{\rho_{13}(\mu_1^*) F_{in} dA_i\}$$

$$P_{D1} = \rho_{13}(\mu_1^*) F_{in} dA_j$$

With a diffusely reflecting deposit present on the substrate the power incident on the detector in the non-specular directions is

$$P_{D2} = \frac{I_r \cos \beta_i \cancel{\cos \beta_j} dA_i dA_j}{r^2}$$

$$P_{D2} = \left(\frac{\pi I_r}{F_{in}}\right) \mu_1 \frac{dA_i dA_j}{r^2} \left(\frac{F_{in}}{\pi}\right)$$

$$P_{D2} = \rho_{ba}^d(\mu_1) \mu_1 \left(\frac{dA_i dA_j}{r^2} \frac{F_o \mu_1^*}{\pi}\right) \tag{178}$$

where $\cos \beta_i = \mu_1$.

The ratio of the detector outputs is

$$\frac{P_{D2}}{P_{D1}} = \left(\frac{dA_i}{\pi r^2 \rho_{13}(\mu_1^*)}\right) \rho_{ba}^d(\mu_j)\mu_j \tag{179}$$

It should be noticed that the term in brackets is a constant. Now let the bare substrate be considered as a perfectly diffuse surface. The expression for the power incident on the detector is given by Equation 178 where the reflected flux is

$$\pi I_r = 2\pi \int_o^1 \rho_{13}(\mu_1) \frac{F_o}{2\pi} \delta(\mu_1 - \mu_1^*)\mu_1 d\mu_1$$

$$I_r = \rho_{13} \frac{(\mu_1^*)F_o\mu_1^*}{\pi} \tag{180}$$

Substitution of Equation 180 into Equation 178 gives the power incident on the detector as

$$P_{D3} = \rho_{13}(\mu_1^*)\mu_1^* \frac{dA_i dA_j}{r^2} \left(\frac{F_{in}}{\pi}\right)$$

Now the ratio of the detector outputs becomes

$$\frac{P_{D2}}{P_{D3}} = \left(\frac{1}{\rho_{13}(\mu_1^*)\mu_1^*}\right) \rho_{ba}^d(\mu_j)\mu_j. \tag{181}$$

The expression in brackets again is a constant. Comparison of Equations 179 and 181 shows that the value of this constant in the detector output ratios can vary considerably depending on whether the substrate is assumed to be perfectly diffuse or specular. Since no surface is exactly diffuse or specular, the value of the constant in Equation 140 of Chapter X was picked before comparing the angular dependence of the data and theory in Figure 62, page 181.

DOCUMENT CONTROL DATA - R & D

(Security classification of title, body of abstract and indexing annotation must be entered when the overall report is classified)

1. ORIGINATING ACTIVITY (Corporate author) Arnold Engineering Development Center, ARO, Inc., Operating Contractor, Arnold Air Force Station, Tennessee 37389	2a. REPORT SECURITY CLASSIFICATION UNCLASSIFIED 2b. GROUP N/A

3. REPORT TITLE

RADIATIVE HEAT TRANSFER OF COATINGS ON A CRYOGENIC SURFACE

4. DESCRIPTIVE NOTES (Type of report and inclusive dates)

October 1968 to September 1970--Final Report

5. AUTHOR(S) (First name, middle initial, last name)

Jeffrey A. Roux, ARO, Inc.

6. REPORT DATE	7a. TOTAL NO. OF PAGES	7b. NO. OF REFS
April 1971	223	29

8a. CONTRACT OR GRANT NO. F40600-71-C-0002	9a. ORIGINATOR'S REPORT NUMBER(S) AEDC-TR-71-90
b. PROJECT NO. Program Element 64719F c. d.	9b. OTHER REPORT NO(S) (Any other numbers that may be assigned this report) ARO-VKF-TR-71-66

10. DISTRIBUTION STATEMENT

Approved for public release; distribution unlimited.

11. SUPPLEMENTARY NOTES	12. SPONSORING MILITARY ACTIVITY
Available in DDC	Arnold Engineering Development Center (XON), Arnold Air Force Station, Tennessee 37389

13. ABSTRACT

An analytical model for the radiative characteristics of coatings formed on a cryogenic surface is presented. In creating a realistic mathematical model, six different sets of boundary conditions are employed in order to determine which most closely approximates the actual experimental results. The medium is considered to be absorbing and scattering; due to the cryogenic temperatures involved, emission is justifiably neglected. The scattering is considered as isotropic. To determine the best analytical model, the theoretical results are compared to experimental data in order to provide a test of the validity of the radiative transfer theory upon which the analytical predictions are based. Then using a combination of experimental results and the chosen analytical model, the monochromatic absorption and scattering coefficients for H_2O and CO_2 cryodeposits are simultaneously determined in the visible wavelength region. The results are demonstrated in the form of hemispherical-directional reflectance and intensity profiles within the medium. Also bidirectional reflectance distributions are presented and compared with experimental data.

14. KEY WORDS	LINK A		LINK B		LINK C	
	ROLE	WT	ROLE	WT	ROLE	WT
cryogenic temperature						
radiation						
heat transfer						
cryopumping						
mathematical model						
monochromatic radiation						
reflectance						

AFSC
Arnold AFS Tenn